박사 학위논문
Ph. D. Dissertation

저차 솔리드 및 쉘 유한요소의 향상을 위한 변형률 완화 요소법

Strain-smoothed element method for improving low-order solid and shell finite elements

2020

이 채 민 (李 埰 旻 Lee, Chaemin)

한 국 과 학 기 술 원

Korea Advanced Institute of Science and Technology

박사 학위논문

저차 솔리드 및 쉘 유한요소의 향상을 위한 변형률 완화 요소법

2020

이 채 민

한 국 과 학 기 술 원

기계항공공학부/기계공학과

저차 솔리드 및 쉘 유한요소의 향상을 위한 변형률 완화 요소법

이 채 민

위 논문은 한국과학기술원 박사학위논문으로
학위논문 심사위원회의 심사를 통과하였음

2020년 6월 1일

심사위원장 이 필 승 (인)

심 사 위 원 임 세 영 (인)

심 사 위 원 오 일 권 (인)

심 사 위 원 김 성 수 (인)

심 사 위 원 노 건 우 (인)

Strain-smoothed element method for improving low-order solid and shell finite elements

Chaemin Lee

Advisor: Phill-Seung Lee

A dissertation submitted to the faculty of
Korea Advanced Institute of Science and Technology in
partial fulfillment of the requirements for the degree of
Doctor of Philosophy in Mechanical Engineering

Daejeon, Korea
June 1, 2020

Approved by

Phill-Seung Lee
Professor of Mechanical Engineering

The study was conducted in accordance with Code of Research Ethics[1].

1) Declaration of Ethical Conduct in Research: I, as a graduate student of Korea Advanced Institute of Science and Technology, hereby declare that I have not committed any act that may damage the credibility of my research. This includes, but is not limited to, falsification, thesis written by someone else, distortion of research findings, and plagiarism. I confirm that my dissertation contains honest conclusions based on my own careful research under the guidance of my advisor.

DME

이채민. 저차 솔리드 및 쉘 유한요소의 향상을 위한 변형률 완화 요소법. 기계공학과. 2020년. 125+ix 쪽. 지도교수: 이필승. (영문 논문)

Lee, Chaemin. Strain-smoothed element method for improving low-order solid and shell finite elements. Department of Mechanical Engineering. 2020. 125+ix pages. Advisor: Lee, Phill-Seung. (Text in English)

초 록

본 학위 논문에서는 저차 솔리드 및 쉘 유한요소의 성능을 대폭 향상시키기 위한 새로운 유한요소법인 변형률완화요소법(strain-smoothed element method)을 제안한다. 변형률완화요소법은 추가적인 자유도를 도입하지 않으며, 이웃한 요소들의 정보를 완전히 활용하여 해의 정확도를 크게 향상시킨다. 기존의 변형률완화 기반 기법들에서는 별도로 완화영역(smoothing domain)을 구성해주어야 하며, 요소가 아닌 완화영역을 기준으로 변형률장(strain field)이 형성된다는 문제가 있었다. 하지만 본 기법에서는 기존 유한요소법에서와 마찬가지로 요소에 대해서 변형률장이 형성되며, 기존 저차요소를 사용했을 때보다 더 연속적이며 정확한 결과를 제공한다. 일정 변형률장을 가지는 선형 유한요소들(삼각형 및 사면체 솔리드요소)에 최초로 적용되었으며, 이후 기법을 확장하여 변형률완화요소법 기반 사각형 솔리드요소를 개발하였다. 본 기법을 활용하여 기존 쉘요소보다 뛰어난 막(membrane)거동을 보이는 변형률완화요소법 기반 MITC3+ 쉘요소를 개발하였으며, 토탈 라그랑지안(total Lagrangian) 수식을 이용하여 기하비선형해석(geometric nonlinear analysis)으로 확장하였다. 제안된 기법을 수학적으로 검증하기 위해 변분원리(variational principle)를 정립하였으며, 이를 이용하여 제안된 기법의 수렴이론을 규명하였다.

핵심낱말 유한요소법, 변형률완화요소법, 솔리드 유한요소, 쉘 유한요소, 구조해석, 기하비선형해석

Abstract

A new strain smoothing method called the strain-smoothed element (SSE) method has been proposed. The SSE method does not require additional degrees of freedom, and provides highly accurate solutions by fully utilizing the strains of neighboring finite elements. Unlike with previous strain smoothing methods, special smoothing domains are not created, and more continuous and accurate strain fields are constructed within elements. The SSE method was first applied to linear solid elements (also called constant strain elements), i.e., 3-node triangular 2D and 4-node tetrahedral 3D solid elements. A further study has been conducted to extend the method to general low-order finite elements, and as a result, a strain-smoothed 4-node quadrilateral 2D solid element was developed. Using the SSE method, a strain-smoothed MITC3 + shell finite element was developed that exhibits much improved membrane behavior compared with the original MITC3+ shell finite element. Then, we present the total Lagrangian formulation of the strain-smoothed MITC3+ shell element for geometric nonlinear analysis. A variational principle for the SSE method was constructed and convergence and stability analyses were performed based on the defined variational principle.

Keywords Finite element method, Strain-smoothed element method, Solid elements, Shell elements, Structural analysis, Geometric nonlinear analysis

Contents

List of Tables

List of Figures

Chapter 1. Introduction

The finite element method (FEM) has been widely used for solving problems in various engineering fields over the past several decades. There are various types of finite elements for analysis of solid mechanics problems, among which low-order finite elements such as 3-node triangular elements and 4-node tetrahedral elements are very attractive due to their simplicity and efficiency. The low-order elements have high modeling capabilities and are particularly preferred for large deformation analysis requiring automatic remeshing. Also, they often provide a relatively easy way to solve complicated engineering problems such as contact analysis. However, in general, the predictive capability of low-order elements is not good enough to be used in engineering practice. Further development of low-order finite elements with improved accuracy is still required while maintaining its advantages [1-3].

Recently, the smoothed finite element method (S-FEM) was developed and successfully applied to various mechanics problems. In S-FEM, the strain smoothing technique is applied to smooth the strain field of standard FEM. Piecewise constant strain fields are constructed in newly established smoothing domains. The smoothing domains can be constructed on the basis of a cell, node, edge, or face; thus, cell-based, node-based, edge-based, and face-based S-FEM methods were devised. There are differences in characteristics and performance among the methods, and edge-based S-FEM is generally known to be most effective. Compared to standard FEM, S-FEM achieves significantly improved accuracy, especially for 3-node triangular and 4-node tetrahedral solid finite elements. The important advantage of S-FEM is that no additional degrees of freedom (DOFs) are required [4-21].

In this study, a new strain smoothing method called the strain-smoothed element method (SSE method) is first proposed for linear solid elements (also called constant strain elements), i.e. 3-node 2D triangular and 4-node 3D tetrahedral solid elements. The distinct feature of the SSE method is that special smoothing domains are not created, and that linear strain fields are constructed within elements. The linear strain field of an element is synthesized utilizing the constant strains of neighboring finite elements through simple strain smoothing. In this way, we obtain the full advantages of strain smoothing, and have a smoothed strain field integrated within the element. The SSE method is simple and provided more accurate solutions in a variety of numerical examples than with the standard FEM, and with the face-based and edge-based S-FEM methods [22].

Then, the author proposes its application for a 4-node quadrilateral finite element and thus a strain-smoothed 4-node quadrilateral finite element is developed. An important key is to employ the piecewise linear shape functions instead of the standard bilinear shape functions. The proposed strain-smoothed element has a bilinear strain field where the strains of neighboring elements are integrated within an element formulation through a new strain smoothing technique. Consequently, the new finite element provides highly accurate solutions, which are illustrated in various benchmark problems [23].

Adopting the mixed interpolation of tensorial components (MITC) method for the continuum mechanics based 3-node triangular shell finite element, the MITC3+ shell element was recently developed. Its excellent bending behavior has been demonstrated through various numerical examples [24]. However, the membrane behavior of the MITC3+ shell element is the same as that of the displacement-based 3-node triangular shell elements. The author proposes a strain-smoothed MITC3+ shell finite element in which the membrane behavior of the MITC3+ shell finite element is improved by employing the SSE method, and thus additional DOFs are unnecessary. The covariant strain fields of the MITC3+ shell element are decomposed into membrane, bending and transverse shear parts. The SSE method is applied only to the membrane part. Convergence behavior is improved in membrane-dominated and mixed bending-membrane problems while maintaining good convergence behavior in bending-dominated problems [25].

Also, the formulation of the strain-smoothed MITC3+ shell finite element for geometric nonlinear analysis is presented. The total Lagrangian formulation is used allowing for large displacements and rotations. The MITC method is employed for the transverse shear strain fields. The SSE method is adopted for the membrane strain fields of the MITC3+ shell element, leading to the tangent stiffness matrix and internal force vector. The nonlinear performance of the strain-smoothed MITC3+ shell element is evaluated through various numerical examples. This study shows that the SSE method originally proposed for linear analysis can be easily extended for nonlinear analysis and produces reliable solutions in nonlinear analysis.

So far, the properties of the SSE method have only been verified by numerical means. We now establish a theoretical foundation for the SSE method. The smoothed strains in the SSE method can be obtained by applying a sequence of orthogonal projection operators among assumed strain spaces. Invoking this observation, a mixed variational principle for the SSE method is established. The SSE method can be derived as a conforming Galerkin approximation of the defined variational principle. We perform convergence and stability analyses of the SSE method based on the variational principle.

Chapter 2. A new strain smoothing method for linear order 2D and 3D solid finite elements

In this chapter, a new strain smoothing method (the strain-smoothed element method) that is useful for finite element analysis of problems in two-dimensional (2D) and three-dimensional (3D) solid mechanics is proposed. The strain-smoothed element (SSE) method is simple and provides highly accurate solutions. No additional degrees of freedom (DOFs) are required, while for other methods such as extended FEM and enriched FEM, additional DOFs are required to improve accuracy [26-32]. The SSE method is first developed for linear solid finite elements (also called constant strain elements), i.e. 3-node triangular 2D and 4-node tetrahedral 3D solid elements.

We briefly review the edge-based strain smoothing method [10,14], and present the formulation of the SSE method, for the 3-node triangular and 4-node tetrahedral solid elements for analysis of solid mechanics problems [23].

2.1. Strain smoothing method for 3-node triangular 2D solid elements

2.1.1. The edge-based smoothed triangular element

The geometry of the standard 3-node triangular 2D solid element is described by

$$\mathbf{x} = \sum_{i=1}^{3} h_i(r,s)\mathbf{x}_i \quad \text{with} \quad \mathbf{x}_i = \begin{bmatrix} x_i & y_i \end{bmatrix}^T , \tag{2.1}$$

where $\mathbf{x}_i$ is the position vector of node i in the global Cartesian coordinate system, and $h_i(r,s)$ is the 2D interpolation function of the standard isoparametric procedure corresponding to node i given by

$$h_1 = 1 - r - s , \quad h_2 = r , \quad h_3 = s . \tag{2.2}$$

The displacement of the standard 3-node triangular 2D solid element is interpolated by

$$\mathbf{u} = \sum_{i=1}^{3} h_i(r,s)\mathbf{u}_i \quad \text{with} \quad \mathbf{u}_i = \begin{bmatrix} u_i & v_i \end{bmatrix}^T , \tag{2.3}$$

where $\mathbf{u}_i$ is the displacement vector of node i in the global Cartesian coordinate system.

Employing the standard isoparametric finite element procedure, the strain field within a 3-node triangular element is obtained using

$$\boldsymbol{\varepsilon}^{(e)} = \mathbf{B}^{(e)}\mathbf{u}^{(e)} \quad \text{with} \quad \mathbf{B}^{(e)} = \begin{bmatrix} \mathbf{B}_1 & \mathbf{B}_2 & \mathbf{B}_3 \end{bmatrix} , \quad \mathbf{u}^{(e)} = [\mathbf{u}_1 \quad \mathbf{u}_2 \quad \mathbf{u}_3]^T , \tag{2.4}$$

in which $\boldsymbol{\varepsilon}^{(e)} = [\varepsilon_{xx} \quad \varepsilon_{yy} \quad 2\varepsilon_{xy}]^T$, $\mathbf{B}^{(e)}$ is the strain-displacement matrix of an element, $\mathbf{u}^{(e)}$ is the nodal displacement vector of the element, and $\mathbf{B}_i$ is the strain-displacement matrix corresponding to node i .

In the edge-based strain smoothing method, smoothing domains are formed based on elements in standard FEM (shown in **Fig. 2.1**a). Let us consider two elements adjacent to the target edge painted in red in the figure. Each element is divided into three sub-triangles using its nodes and a center point ($r = s = 1/3$), and each sub-triangle is named "cell", see **Fig. 2.1**(b). In the red edge considered, the edge-based smoothing domain is defined as an assemblage of two neighboring cells belonging to different elements.

The smoothed strain for the edge-based smoothing domain is given by

$$\bar{\boldsymbol{\varepsilon}} = \frac{1}{A_c^{(1)} + A_c^{(2)}} (A_c^{(1)} \boldsymbol{\varepsilon}^{(1)} + A_c^{(2)} \boldsymbol{\varepsilon}^{(2)}) \tag{2.5}$$

where $A_c^{(1)}$ and $A_c^{(2)}$ are the areas of the first and second cells neighboring the target edge, and $\boldsymbol{\varepsilon}^{(1)}$ and $\boldsymbol{\varepsilon}^{(2)}$ are the strains of the neighboring finite elements. While **Fig. 2.1**(a) shows a typical domain discretization in the standard FEM, smoothing domains are shown in **Fig. 2.1**(c).

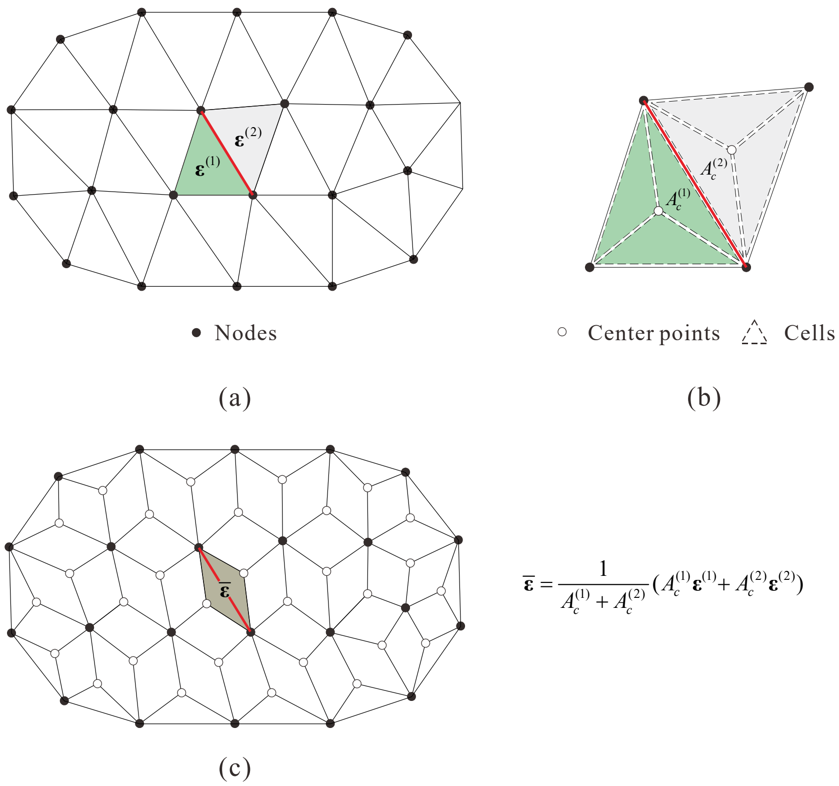

Fig. 2.1. Construction of edge-based smoothed strain fields: (a) Elements of the standard FEM. The red line corresponds to a target edge. (b) The elements are divided into three cells. (c) Smoothing domains and smoothed strains of the edge-based S-FEM. Piecewise constant strain fields are constructed for elements in (a) and for smoothing domains in (c).

The edge-based strain smoothing method also has a constant strain field in the smoothing domain. It is known that the 3-node triangular elements subject to the edge-based strain smoothing method pass all the basic tests (patch, isotropy, and zero energy mode tests), and that the edge-based strain smoothing method shows the best performance among various S-FEM methods. Thus, the edge-based smoothing method has been extended for polyhedral 3D solid elements (see Ref. [15] for its formulation).

2.1.2. The proposed strain-smoothed triangular element

With the proposed method, the strains of all neighboring elements are fully utilized in the strain smoothing process. For 3-node triangular elements, the strains of up to three surrounding elements can be used through element edges (see **Fig. 2.2**a) where $\boldsymbol{\varepsilon}^{(e)}$ is the strain of a target element and $\boldsymbol{\varepsilon}^{(k)}$ is the strain of the k th neighboring element.

Let us define smoothed strains between the target element and neighboring elements

$$\hat{\boldsymbol{\varepsilon}}^{(k)} = \frac{1}{A^{(e)} + A^{(k)}}(A^{(e)}\boldsymbol{\varepsilon}^{(e)} + A^{(k)}\boldsymbol{\varepsilon}^{(k)}) \quad \text{with} \quad k = 1, 2, 3, \tag{2.6}$$

where $A^{(e)}$ and $A^{(k)}$ are the areas of the target element and the k th neighboring element, respectively, see **Fig. 2.2**(b). Note that if the k th edge of the target element corresponds to a boundary, there is no neighboring element for the edge and thus $\hat{\boldsymbol{\varepsilon}}^{(k)} = \boldsymbol{\varepsilon}^{(e)}$ is used.

Smoothed strains in Eq. (2.7) can also be expressed in a matrix and vector form as

$$\hat{\boldsymbol{\varepsilon}}^{(k)} = \hat{\mathbf{B}}^{(k)}\hat{\mathbf{u}}^{(k)} \quad \text{with} \quad \hat{\mathbf{B}}^{(k)} = \begin{bmatrix} \hat{\mathbf{B}}_1 & \hat{\mathbf{B}}_2 & \hat{\mathbf{B}}_3 & \hat{\mathbf{B}}_{k+3} \end{bmatrix}, \quad \hat{\mathbf{u}}^{(k)} = [\mathbf{u}_1 \quad \mathbf{u}_2 \quad \mathbf{u}_3 \quad \mathbf{u}_{k+3}]^T . \tag{2.7}$$

where $\hat{\mathbf{B}}^{(k)}$ and $\hat{\mathbf{u}}^{(k)}$ are the strain-displacement matrix and the corresponding displacement vector of the element for the smoothed strains $\hat{\boldsymbol{\varepsilon}}^{(k)}$. The subscript i in $\hat{\mathbf{B}}_i$ and $\mathbf{u}_i$ denotes the neighboring node number as shown in **Fig. 2.2**(a).

In a 3-node triangular element, three point Gauss integration is used to calculate the stiffness matrix. The smoothed strain values in Eq. (2.7) are directly assigned to the Gauss points (a, b, and c in **Fig. 2.2**c) of the target element using the following equations, as shown in **Fig. 2.2**(d)

$$\boldsymbol{\varepsilon}^a = \frac{1}{2}(\hat{\boldsymbol{\varepsilon}}^{(1)} + \hat{\boldsymbol{\varepsilon}}^{(3)}), \quad \boldsymbol{\varepsilon}^b = \frac{1}{2}(\hat{\boldsymbol{\varepsilon}}^{(1)} + \hat{\boldsymbol{\varepsilon}}^{(2)}), \quad \boldsymbol{\varepsilon}^c = \frac{1}{2}(\hat{\boldsymbol{\varepsilon}}^{(2)} + \hat{\boldsymbol{\varepsilon}}^{(3)}). \tag{2.8}$$

Therefore, in the computation of the stiffness matrix and stress, the strains assigned in Eq. (2.9) are used directly at the Gauss integration points. The strain field within the element can be explicitly expressed in a form of assumed strain

$$\bar{\boldsymbol{\varepsilon}}^{(e)} = \left[1 - \frac{1}{q-p}(r + s - 2p)\right]\boldsymbol{\varepsilon}^a + \frac{r-p}{q-p}\boldsymbol{\varepsilon}^b + \frac{s-p}{q-p}\boldsymbol{\varepsilon}^c , \tag{2.9}$$

where $p = 1/6$ and $q = 4/6$ are the constants indicating the positions of the Gauss points. Note that the use of this equation is not necessary in actual computations.

When the element has three neighboring elements with common element edges, the strain-displacement relation for the strain field can be expressed in a vector and matrix form as

$$\bar{\boldsymbol{\varepsilon}}^{(e)} = \bar{\mathbf{B}}^{(e)} \bar{\mathbf{u}}^{(e)}, \tag{2.10}$$

with

$$\bar{\mathbf{B}}^{(e)} = \left[\bar{\mathbf{B}}_1 \quad \bar{\mathbf{B}}_2 \quad \bar{\mathbf{B}}_3 \quad \bar{\mathbf{B}}_4 \quad \bar{\mathbf{B}}_5 \quad \bar{\mathbf{B}}_6 \right], \tag{2.11}$$

$$\bar{\mathbf{u}}^{(e)} = \left[\mathbf{u}_1 \quad \mathbf{u}_2 \quad \mathbf{u}_3 \quad \mathbf{u}_4 \quad \mathbf{u}_5 \quad \mathbf{u}_6 \right]^T, \tag{2.12}$$

where $\bar{\mathbf{B}}^{(e)}$ is the strain-displacement matrix of the strain-smoothed element, and $\bar{\mathbf{u}}^{(e)}$ is the corresponding displacement vector of the element. Note that the components of the strain-displacement matrix and the displacement vector vary depending on the configurations of neighboring elements.

As in other strain smoothing methods, exterior (boundary) elements have relatively fewer neighboring elements than interior elements and thus the strain smoothing effect in the exterior region could be less than that in the interior region.

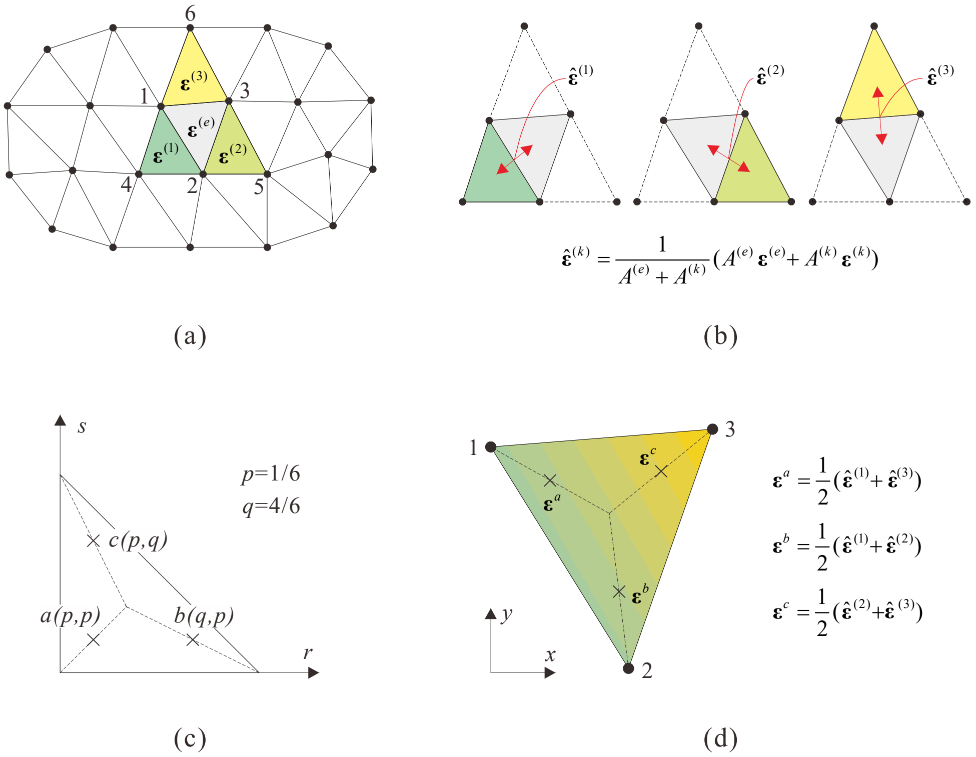

Fig. 2.2. Strain-smoothed element method for the 3-node triangular element: (a) Strains of a target element and its neighboring elements. Node numbers are used for explaining the formulation. (b) Strain smoothing between the target and each neighboring element. (c) Three Gauss integration points in the natural coordinate system (r,s). (d) Construction of the smoothed strain field through Gauss points.

2.2. The strain-smoothed 4-node tetrahedral 3D solid finite element

The geometry of the standard 4-node tetrahedral 3D solid element is described by

$$\mathbf{x} = \sum_{i=1}^{4} h_i(r,s,t)\mathbf{x}_i \quad \text{with} \quad \mathbf{x}_i = \begin{bmatrix} x_i & y_i & z_i \end{bmatrix}^T , \tag{2.13}$$

where $\mathbf{x}_i$ is the position vector of node i in the global Cartesian coordinate system, and $h_i(r,s,t)$ is the 3D interpolation function of the standard isoparametric procedure corresponding to node i given by

$$h_1 = 1-r-s-t\ ,\ \ h_2 = r\ ,\ \ h_3 = s\ ,\ \ h_4 = t\ . \tag{2.14}$$

The displacement of the standard 4-node tetrahedral 3D solid element is given by

$$\mathbf{u} = \sum_{i=1}^{4} h_i(r,s,t)\mathbf{u}_i \quad \text{with} \quad \mathbf{u}_i = \begin{bmatrix} u_i & v_i & w_i \end{bmatrix}^T , \tag{2.15}$$

where $\mathbf{u}_i$ is the displacement vector of node i in the global Cartesian coordinate system.

The strain-displacement relation of the standard tetrahedral element is

$$\boldsymbol{\varepsilon}^{(e)} = \mathbf{B}^{(e)}\mathbf{u}^{(e)} , \tag{2.16}$$

with

$$\mathbf{B}^{(e)} = \begin{bmatrix} \mathbf{B}_1 & \mathbf{B}_2 & \mathbf{B}_3 & \mathbf{B}_4 \end{bmatrix},\ \ \mathbf{u}^{(e)} = \begin{bmatrix} \mathbf{u}_1 & \mathbf{u}_2 & \mathbf{u}_3 & \mathbf{u}_4 \end{bmatrix}^T , \tag{2.17}$$

where $\boldsymbol{\varepsilon}^{(e)} = [\varepsilon_{xx} \quad \varepsilon_{yy} \quad \varepsilon_{zz} \quad 2\varepsilon_{xy} \quad 2\varepsilon_{yz} \quad 2\varepsilon_{zx}]^T$, $\mathbf{B}^{(e)}$ is the strain-displacement matrix of an element, and $\mathbf{u}^{(e)}$ is the displacement vector of the element.

In a tetrahedral element, configurations of neighboring elements through six element edges can differ. Smoothed strains between the target element and neighboring elements through the edges are calculated using the following equations

$$\hat{\boldsymbol{\varepsilon}}^{(k)} = \frac{1}{V^{(e)} + \sum_{i=1}^{n_k} V_i^{(k)}} \left(V^{(e)}\boldsymbol{\varepsilon}^{(e)} + \sum_{i=1}^{n_k} V_i^{(k)}\boldsymbol{\varepsilon}_i^{(k)}\right) \quad \text{with} \quad k = 1, 2, 3, 4, 5, 6, \tag{2.18}$$

where n_k is the number of elements neighboring the k th edge of the target element, $\boldsymbol{\varepsilon}^{(e)}$ and $\boldsymbol{\varepsilon}_i^{(k)}$ are the strains of the target element and the i th element neighboring the k th edge of the target element, respectively. Here, $V^{(e)}$ and $V_i^{(k)}$ are the volumes of the target element and the i th element neighboring the k th edge, respectively, see **Fig. 2.3**(a). Note that if the k th edge of the target element is located alone along a boundary without neighboring elements, $n_k = 0$ and thus $\hat{\boldsymbol{\varepsilon}}^{(k)} = \boldsymbol{\varepsilon}^{(e)}$.

The stiffness matrix of the tetrahedral element is calculated using the four point Gauss integration, see the positions of the Gauss points a, b, c, and d in **Fig. 2.3**(b). The strains at the Gauss points are directly assigned using the following equations, as shown in **Fig. 2.3**(c)

$$\boldsymbol{\varepsilon}^{a}=\frac{1}{5}(\hat{\boldsymbol{\varepsilon}}^{(1)}+\hat{\boldsymbol{\varepsilon}}^{(2)}+\hat{\boldsymbol{\varepsilon}}^{(3)}+\hat{\boldsymbol{\varepsilon}}+\boldsymbol{\varepsilon}^{(e)}),\quad \boldsymbol{\varepsilon}^{b}=\frac{1}{5}(\hat{\boldsymbol{\varepsilon}}^{(1)}+\hat{\boldsymbol{\varepsilon}}^{(4)}+\hat{\boldsymbol{\varepsilon}}^{(6)}+\hat{\boldsymbol{\varepsilon}}+\boldsymbol{\varepsilon}^{(e)}),$$
$$\boldsymbol{\varepsilon}^{c}=\frac{1}{5}(\hat{\boldsymbol{\varepsilon}}^{(2)}+\hat{\boldsymbol{\varepsilon}}^{(4)}+\hat{\boldsymbol{\varepsilon}}^{(5)}+\hat{\boldsymbol{\varepsilon}}+\boldsymbol{\varepsilon}^{(e)}),\quad \boldsymbol{\varepsilon}^{d}=\frac{1}{5}(\hat{\boldsymbol{\varepsilon}}^{(3)}+\hat{\boldsymbol{\varepsilon}}^{(5)}+\hat{\boldsymbol{\varepsilon}}^{(6)}+\hat{\boldsymbol{\varepsilon}}+\boldsymbol{\varepsilon}^{(e)})\ \text{ with }\ \hat{\boldsymbol{\varepsilon}}=\frac{1}{6}\sum_{k=1}^{6}\hat{\boldsymbol{\varepsilon}}^{(k)}\,. \tag{2.19}$$

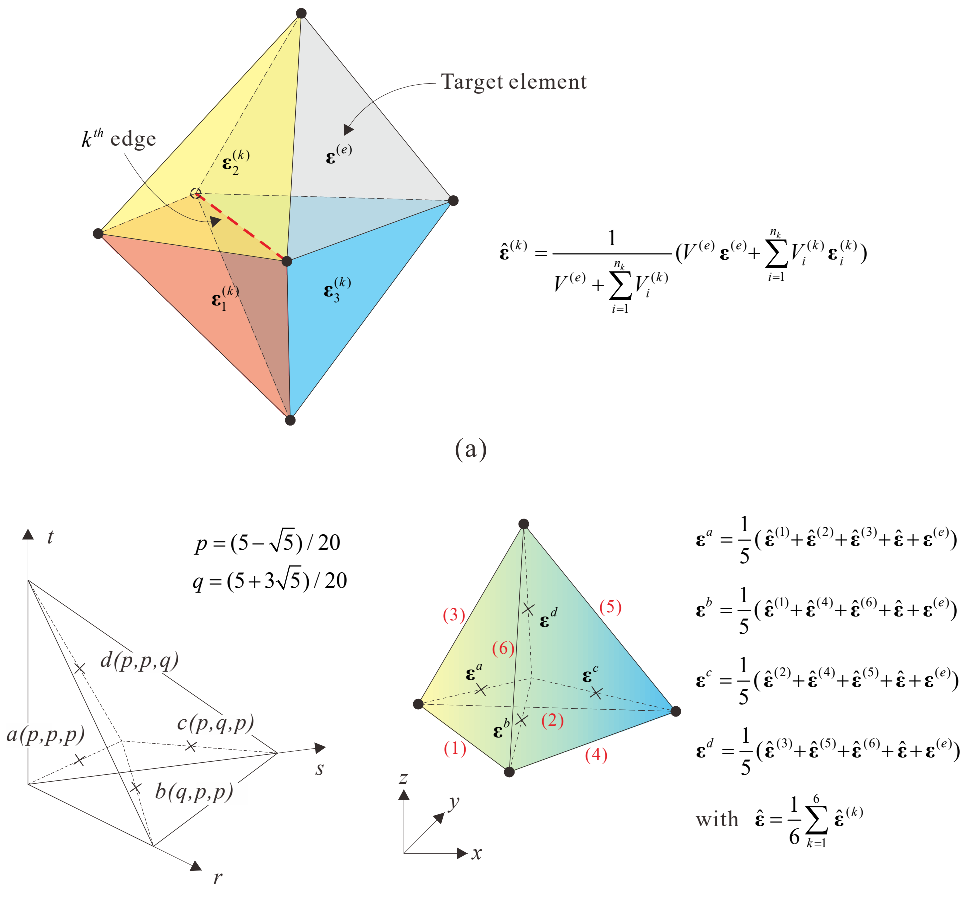

Fig. 2.3. Strain-smoothed element method for the 4-node tetrahedral element: (a) Strain smoothing between the target and neighboring elements for the k th edge of the target element marked with the red dotted line. There are three neighboring elements through the edge ($n_k=3$). (b) Four Gauss integration points in the natural coordinate system (r,s,t). (c) Construction of the smoothed strain field through Gauss points. Edge numbers are colored in red.

The strain field can be represented by

$$\bar{\boldsymbol{\varepsilon}}^{(e)} = \left[1 - \frac{1}{q-p}(r+s+t-3p)\right]\boldsymbol{\varepsilon}^a + \frac{r-p}{q-p}\boldsymbol{\varepsilon}^b + \frac{s-p}{q-p}\boldsymbol{\varepsilon}^c + \frac{t-p}{q-p}\boldsymbol{\varepsilon}^d , \tag{2.20}$$

with $p = (5-\sqrt{5})/20$ and $q = (5+3\sqrt{5})/20$. Note that this assumed strain field is not used in actual computations.

Strain smoothing methods do not require additional DOFs, but some additional processes are necessary to perform strain smoothing. Several studies have validated the efficiency of the strain smoothing methods by evaluating their computational cost and accuracy. It has been reported that the edge-based strain smoothing method is the most efficient strain smoothing method so far [10,15]. The strain-smoothed element method proposed in this study shows computational cost similar to that of the edge-based strain smoothing method.

2.3. **Basic numerical tests**

For the proposed triangular and tetrahedral elements, three basic numerical tests: the isotropy, patch and zero energy mode tests are performed [1-3].

The isotropy test is to check whether the finite elements give the same results regardless of the node numbering sequences used. The proposed triangular and tetrahedral elements pass the isotropy test.

In the patch tests, the minimum number of degrees of freedom is constrained to prevent rigid body motions, and proper loadings are applied to produce a constant stress field. To satisfy the patch tests, a constant stress value should be obtained at every point on elements. Normal and shear patch tests are performed using the meshes shown in **Fig. 2.4**. Stress values calculated (using 16 significant decimal digits of precision) are extracted from all Gauss integration points and compared with the analytical solutions. In the proposed triangular and tetrahedral elements, the maximum relative error in the normal and shear patch tests are on the order of 10^{-14} to 10^{-15}. Therefore, the proposed elements pass the patch tests with sufficient accuracy.

In the zero energy mode test, the number of zero eigenvalues of the stiffness matrix of unsupported smoothed elements is counted. The 2D and 3D solid elements should have three and six zero eigenvalues, respectively, corresponding to the physical rigid body modes. The proposed elements pass the zero energy mode test.

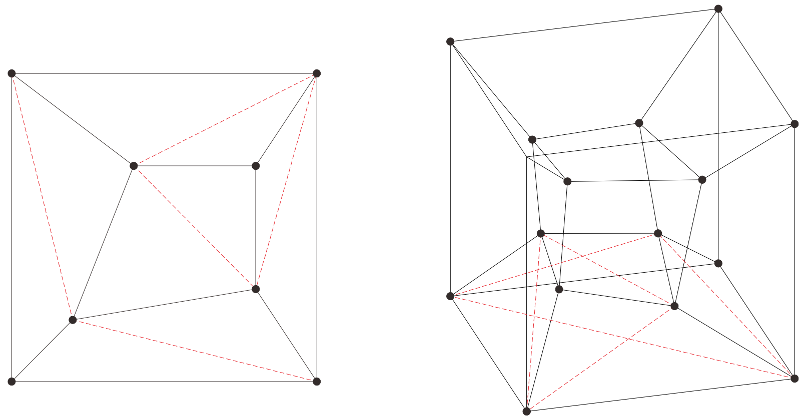

(a) (b)

Fig. 2.4. Finite element meshes used for the patch tests: (a) 2D patch test. Each quadrilateral element is divided into two triangular elements. (b) 3D patch test. Each hexahedral element is divided into six tetrahedral elements. Only the splits in the hexahedral element located at the bottom are depicted.

2.4. **Convergence studies**

In this section, we present the performance of the strain-smoothed elements using three 2D numerical examples (a block problem, Cook's skew beam problem, and an infinite plate with a central hole problem), and two 3D numerical examples (a cubic cantilever problem and Lame problem).

The performance of the proposed 3-node triangular element is compared with those of the standard linear triangular finite element and edge-based smoothed finite element [10]. The performance of the proposed 4-node tetrahedral element is compared with those of the standard linear tetrahedral finite element, edge-based, and face-based smoothed finite elements [15,17]. The edge-based and face-based smoothed elements are denoted by ES-FEM and FS-FEM, respectively.

In some examples, we compare the performance of the proposed triangular and tetrahedral elements with those of the standard quadratic 6-node triangular and 10-node tetrahedral elements, respectively. On the convergence curves, the element size is defined as $h = 1/N$ for linear elements and $h = 1/2N$ for quadratic elements. This allows comparison of linear and quadratic elements with the same DOFs.

We compare the displacements and stresses at a specific location. We also use energy norm. The relative error in the energy norm is given by

$$E_e^2 = \frac{\left| \left\| \mathbf{u}_{ref} \right\|_e^2 - \left\| \mathbf{u}_h \right\|_e^2 \right|}{\left\| \mathbf{u}_{ref} \right\|_e^2} \quad \text{with} \quad \left\| \mathbf{u} \right\|_e^2 = \int_\Omega \boldsymbol{\varepsilon}^T \boldsymbol{\sigma} d\Omega \,, \tag{2.21}$$

where the subscripts *"ref"* and *"h"* denote the reference and finite element solutions, respectively.

For the relative error in the energy norm, the optimal convergence behavior for the linear elements is estimated to be

$$E_e^2 \cong ch^2, \tag{2.22}$$

in which c is a constant and h denotes the element size [1].

2.4.1. Block problem

Here, we solve the 2D block problem shown in **Fig. 2.5**(a). The block is subjected to a distributed compression force of total magnitude $P = 1$ at the right half of the top edge, and the bottom edge of the block is clamped. Plane stress conditions are assumed with $E = 3\times10^7$ and $\nu = 0.3$, and density is given as $\rho = 1\times10^7$. We use structured meshes of $N \times N$ elements with N = 2, 4, 8 and 16 (shown in **Fig. 2.5**b), and unstructured meshes with the total number of elements N_e = 6, 32, 128, 500 (**Fig. 2.5**c). The unstructured meshes are acquired through the commercial software ANSYS. The equivalent values of N in the unstructured meshes are calculated by $N = \sqrt{N_e / 2}$.

Table 2.1 gives the predicted vertical displacement at point A for the structured mesh. **Fig. 2.6** gives the convergence curves obtained using the energy norm for both structured and unstructured meshes. The reference solutions are obtained using a 32×32 structured mesh of 9-node quadrilateral solid elements. The use of the proposed element gives much more accurate solutions than when using the standard and edge-based smoothed elements.

In addition, free vibration analysis is performed to compare the performance of the finite elements considered. The generalized eigenvalue problem is defined as

$$\mathbf{K}\boldsymbol{\varphi}_i = \lambda_i \mathbf{M}\boldsymbol{\varphi}_i \quad \text{with} \quad i = 1, 2, \ \ldots, \ n, \tag{2.23}$$

where $\mathbf{K}$ and $\mathbf{M}$ are the global stiffness and consistent mass matrices, respectively, λ_i and $\boldsymbol{\varphi}_i$ are the eigenvalue and eigenvector corresponding to the i^{th} mode, respectively, and n denotes the number of DOFs in the finite element model. **Table 2.2** presents the obtained eigenvalues corresponding to the 1$^{\text{st}}$ – 5$^{\text{th}}$ modes for the structured mesh with $N = 4$. The proposed element performs very well.

2.4.2. Cook's skew beam problem

We next consider Cook's skew beam problem [3], as shown in **Fig. 2.7**. The structure is subjected to distributed shearing force of total magnitude $P = 1$ at the right edge, and the left edge of the structure is clamped. The plane stress conditions with $E = 3\times10^7$ and $\nu = 0.3$ are considered. The solutions are obtained with $N \times N$

element meshes (N = 2, 4, 8, and 16).

Fig. 2.8 shows the distribution of the calculated strain component $2\varepsilon_{xy}$. The proposed triangular element shows the strain field most similar to the reference distribution. **Table 2.3** gives the von Mises stress at point A, shown in **Fig. 2.7**. The stress values are obtained by averaging stresses in the domains (elements in the proposed method) to which the point belongs. **Fig. 2.9** shows the convergence curves obtained using the energy norm. A 32×32 element mesh of 9-node 2D solid elements is used for the reference solutions. The proposed element shows much better convergence behavior than do the standard linear element and edge-based smoothed element. Interestingly, the convergence performance of the proposed (linear) element is comparable to that of the standard quadratic element.

2.4.3. Infinite plate with a central hole problem

The last 2D example is the problem of an infinite plate with a central hole [4]. The plate is subjected to a far field traction $p=1$ in the x-direction as shown in **Fig. 2.10**(a). The plane strain conditions are considered with $E=3\times 10^7$ and $\nu=0.3$. Due to its symmetry, only one-quarter of the plate is modeled. Symmetric boundary conditions are imposed: $u_x=0$ along AC and $u_y=0$ along BD, and the traction boundary conditions are imposed along CE and DE based on the following analytical solutions [33]:

$$\sigma_{11}(r,\theta)=p-\frac{pa^2}{r^2}\left[\frac{3}{2}\cos 2\theta+\cos 4\theta\right]+\frac{3pa^4}{2r^4}\cos 4\theta\,, \tag{2.24}$$

$$\sigma_{22}(r,\theta)=-\frac{pa^2}{r^2}\left[\frac{1}{2}\cos 2\theta-\cos 4\theta\right]-\frac{3pa^4}{2r^4}\cos 4\theta\,, \tag{2.25}$$

$$\sigma_{12}(r,\theta)=-\frac{pa^2}{r^2}\left[\frac{1}{2}\sin 2\theta+\sin 4\theta\right]+\frac{3pa^4}{2r^4}\sin 4\theta\,, \tag{2.26}$$

where r is the distance from the origin and θ is the angle from the positive x-axis to the counterclockwise direction. The geometry is divided into two parts and meshed for each part using $N\times N$ elements with N = 2, 4, 8 and 16, see **Fig. 2.10**(b).

Table 2.4 and **Fig. 2.11** show the horizontal displacement at point B and the convergence curves obtained using the energy norm, respectively. To obtain the reference solution, a mesh of 9-node 2D solid elements is used with N = 32. Compared with standard and edge-based smoothed elements, the proposed element shows significantly improved accuracy.

2.4.4. Cubic cantilever problem

Here, we solve the 3D cubic cantilever problem [34] shown in **Fig. 2.12**(a). The cubic cantilever is subjected to a uniform pressure $p = 1$ on its upper surface, and the outer surface on the xz -plane is clamped. The material properties are $E = 1$, $\nu = 0.25$, and $\rho = 1$. We use two types of meshes: structured meshes of $N \times N \times N$ elements with N = 2, 4, and 8 (see **Fig. 2.12**b), and unstructured meshes of N_e = 63, 352, and 2973 (see **Fig. 2.12**c). The equivalent values of N in the unstructured meshes are obtained using $N = \sqrt[3]{N_e / 6}$.

Table 2.5 gives the calculated eigenvalues corresponding to the 1st – 5th modes for the structured mesh with $N = 4$. **Fig. 2.13** shows the convergence curves obtained using the energy norm for the structured and unstructured meshes. A structured $16 \times 16 \times 16$ mesh of 27-node hexahedral solid finite elements is used for the reference solutions. The use of the proposed tetrahedral element gives better solutions than when using the standard linear elements and when using either face-based smoothed or edge-based smoothed elements. It is also observed that the performance of the proposed (linear) element is comparable to that of the standard quadratic element.

2.4.5. Lame problem

We last consider the 3D Lame problem [33] shown in **Fig. 2.14**(a). A hollow sphere is subjected to internal pressure $p = 100$, and the given material properties are $E = 1 \times 10^3$ and $\nu = 0.3$. Utilizing the symmetry condition, only one-eighth of the structure is considered. It is divided into three parts, each of which is meshed using $N \times N \times N$ elements with N = 2, 4, and 8 (see **Fig. 2.14**b). The symmetric boundary conditions imposed are $u_x = 0$ along $ACFE$, $u_y = 0$ along $BDFE$, and $u_z = 0$ along $CABD$.

Table 2.6 shows the von-Mises stress at point G, obtained by averaging stresses in the domains (elements in the proposed method) to which the point belongs. **Fig. 2.15** presents the convergence curves obtained using the energy norm. A mesh of 27-node hexahedral solid finite elements with $N = 16$ is used for the reference solution. It is again observed that the proposed element shows significantly improved convergence behavior compared to the standard linear, face-based smoothed, and edge-based smoothed elements.

Table 2.1. Vertical displacement ($\times 10^{-8}$) at point A in the block problem. The values in parentheses indicate relative errors obtained by $\left|u_{ref} - u_h\right| / u_{ref} \times 100$.

N	Standard FEM	ES-FEM	SSE (proposed)
2	-5.7442 (26.71)	-7.3025 (6.82)	-8.1969 (4.59)
4	-6.9824 (10.91)	-7.7441 (1.19)	-7.8770 (0.51)
8	-7.5945 (3.10)	-7.8176 (0.25)	-7.8431 (0.07)
	Reference solution: -7.8372		

Table 2.2. Eigenvalues corresponding to the 1st – 5th modes for the 2D block problem when the structured mesh with $N = 4$ is adopted.

Mode	Reference	Standard FEM	ES-FEM	SSE (proposed)
1	0.3249	0.3828	0.3465	0.3327
2	1.8713	1.9249	1.8934	1.8759
3	2.3552	2.8456	2.4728	2.3634
4	5.9470	7.8848	6.4520	5.7638
5	6.9164	8.5072	7.5547	7.0044

Table 2.3. von-Mises stress at point A in Cook's skew beam problem. The values in parentheses indicate relative errors obtained by $\left|\sigma_{ref} - \sigma_h\right| / \sigma_{ref} \times 100$.

N	Standard FEM	ES-FEM	SSE (proposed)
2	0.0740 (68.77)	0.1009 (57.43)	0.1209 (48.99)
4	0.1123 (52.63)	0.1889 (20.33)	0.2105 (11.19)
8	0.1685 (28.90)	0.2228 (6.03)	0.2290 (3.40)
	Reference solution: 0.2371		

Table 2.4. Horizontal displacement ($\times 10^{-8}$) at point B in the infinite plate with central hole problem. The values in parentheses indicate relative errors obtained by $\left|u_{ref} - u_h\right| / u_{ref} \times 100$.

N	Standard FEM	ES-FEM	SSE (proposed)
2	6.0622 (33.38)	7.5364 (17.18)	8.3902 (7.80)
4	7.3026 (19.75)	8.2955 (8.84)	8.7312 (4.05)
8	8.2250 (9.62)	8.7763 (3.56)	8.9807 (1.31)
	Analytical solution: 9.1000		

Table 2.5. Eigenvalues corresponding to the 1^{st} – 5^{th} modes for the 3D cubic cantilever problem when the structured mesh with $N = 4$ is adopted.

Mode	Reference	Standard FEM	FS-FEM	ES-FEM	SSE (proposed)
1	0.4484	0.5137	0.4946	0.4633	0.4509
2	0.4484	0.5471	0.5211	0.4791	0.4668
3	0.8563	1.1884	1.0718	0.9147	0.8791
4	2.5216	2.6204	2.5970	2.5527	2.5328
5	3.1823	3.7323	3.5445	3.2582	3.1645

Table 2.6. von-Mises stress at point G in Lame problem. The values in parentheses indicate relative errors obtained by $\left|\sigma_{ref} - \sigma_h\right| / \sigma_{ref} \times 100$.

N	Standard FEM	FS-FEM	ES-FEM	SSE (proposed)
2	106.2858 (38.00)	125.3865 (26.86)	150.2877 (12.33)	166.7563 (2.73)
4	132.7286 (22.58)	143.6493 (16.20)	157.3288 (8.22)	166.3370 (2.97)
8	149.4181 (12.84)	155.2355 (9.45)	162.2212 (5.37)	166.6823 (2.77)
16	159.4205 (7.00)	162.5707 (5.17)	167.5228 (2.28)	169.5621 (1.09)
	Analytical solution: 171.4286			

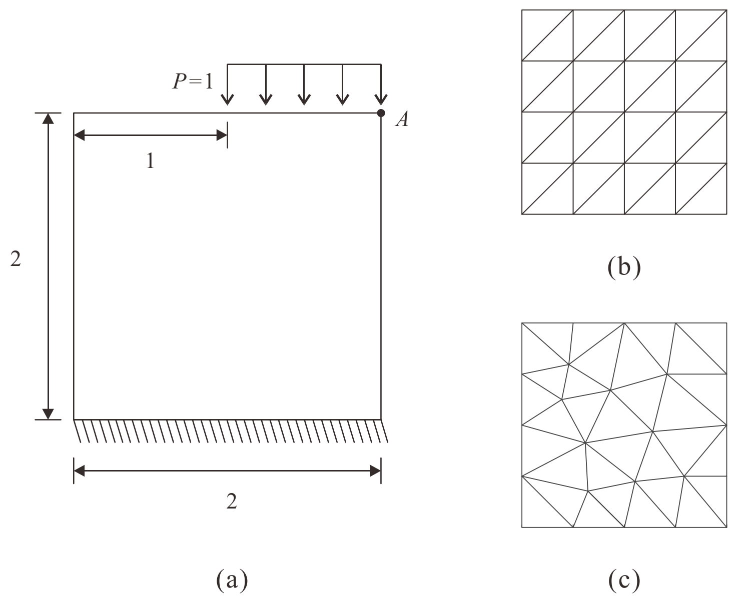

Fig. 2.5. 2D block problem: (a) Problem description ($E = 3\times10^7$ and $\nu = 0.3$). (b) Structured mesh used with $N = 4$. (c) Unstructured mesh used with $N_e = 32$.

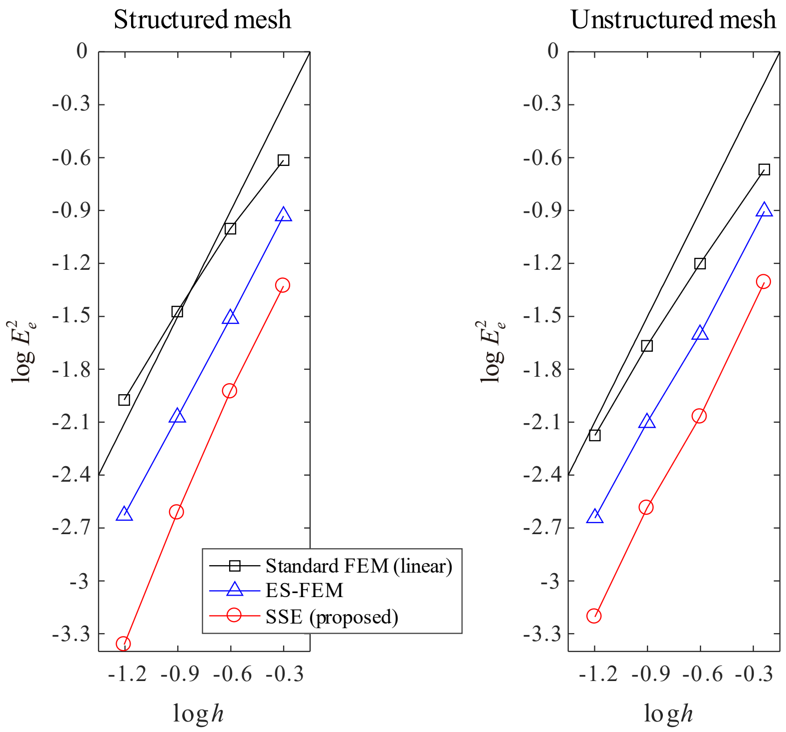

Fig. 2.6. Convergence curves for the 2D block problem. The bold line represents the optimal convergence rate.

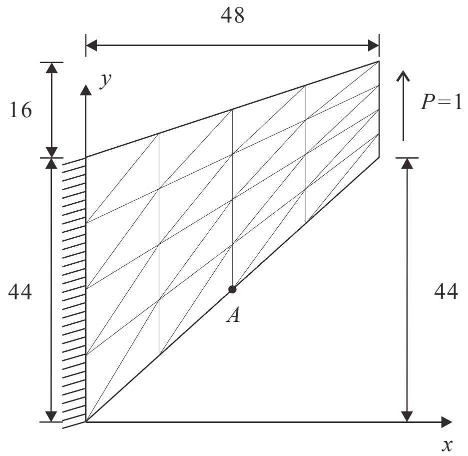

Fig. 2.7. Cook's skew beam problem (4×4 mesh, $E = 3 \times 10^7$ and $\nu = 0.3$).

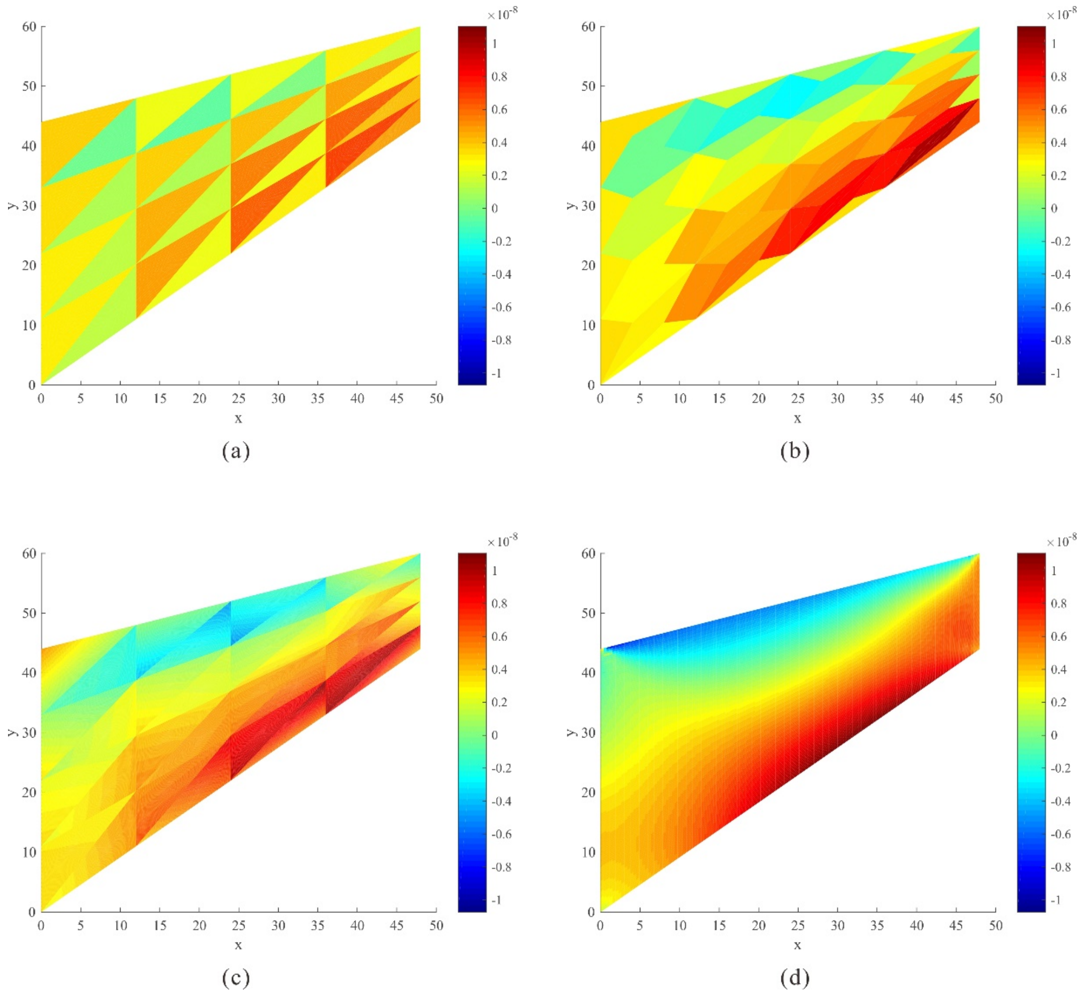

Fig. 2.8. Strain distributions ($2\varepsilon_{xy}$) calculated for Cook's skew beam problem: (a) Standard 3-node triangular element ($N = 4$), (b) Edge-based smoothed element ($N = 4$), (c) Strain-smoothed triangular element ($N = 4$), (d) Standard 9-node quadrilateral element ($N = 32$).

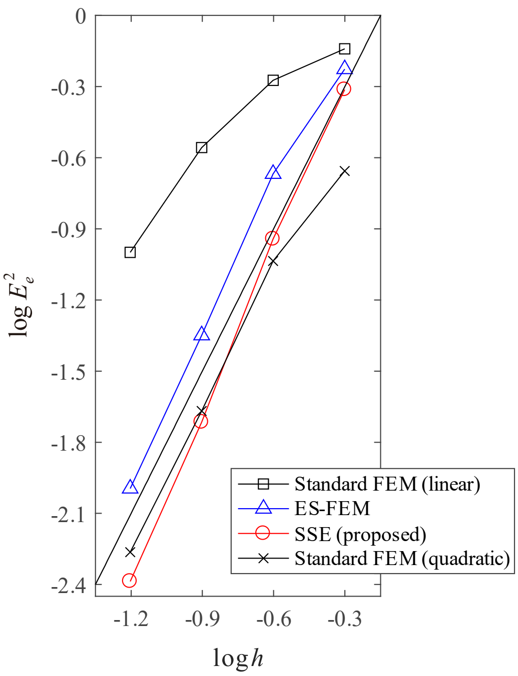

Fig. 2.9. Convergence curves for Cook's skew beam problem: The bold line represents the optimal convergence rate for the linear elements. The element size is $h = 1/N$ for the linear elements and $h = 1/2N$ for the quadratic element.

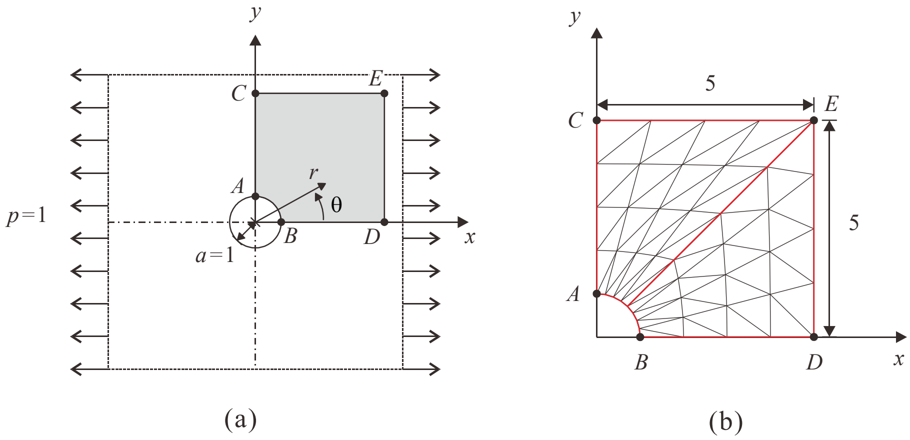

Fig. 2.10. Infinite plate with central hole problem: (a) Problem description ($E = 3\times10^7$ and $\nu = 0.3$). (b) Mesh used with $N = 4$ for the shaded domain in (a).

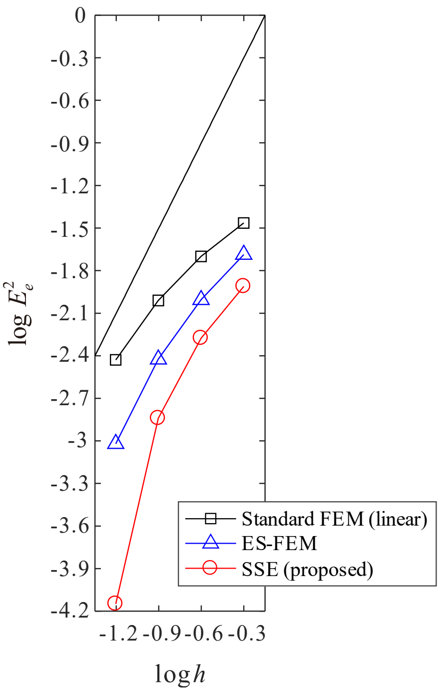

Fig. 2.11. Convergence curves for the infinite plate with central hole problem. The bold line represents the optimal convergence rate.

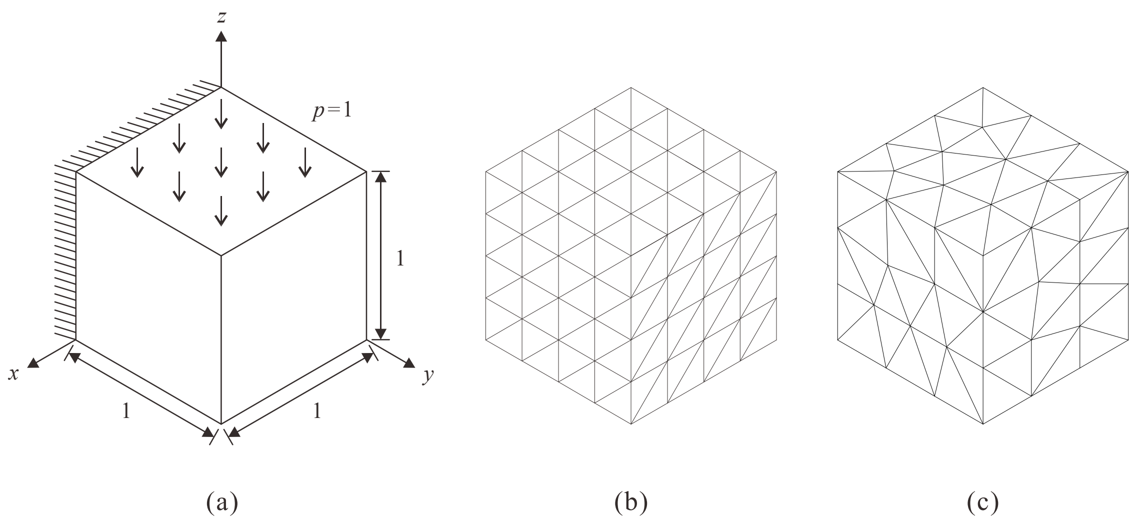

Fig. 2.12. Cubic cantilever problem: (a) Problem description ($E = 1$ and $\nu = 0.25$). (b) Structured mesh with $N = 4$. (c) Unstructured mesh with $N_e = 352$.

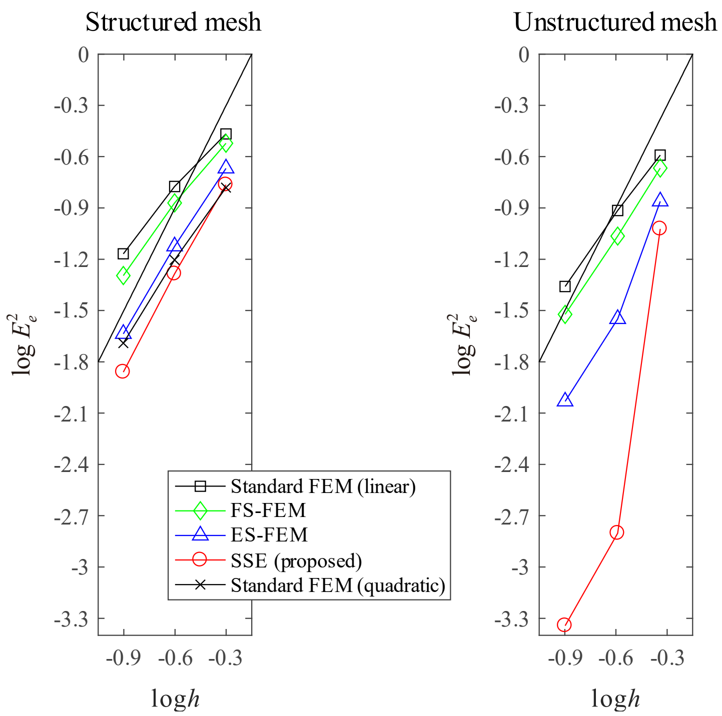

Fig. 2.13. Convergence curves for the cubic cantilever problem: The bold line represents the optimal convergence rate for the linear elements. The element size is $h = 1/N$ for the linear elements and $h = 1/2N$ for the quadratic element.

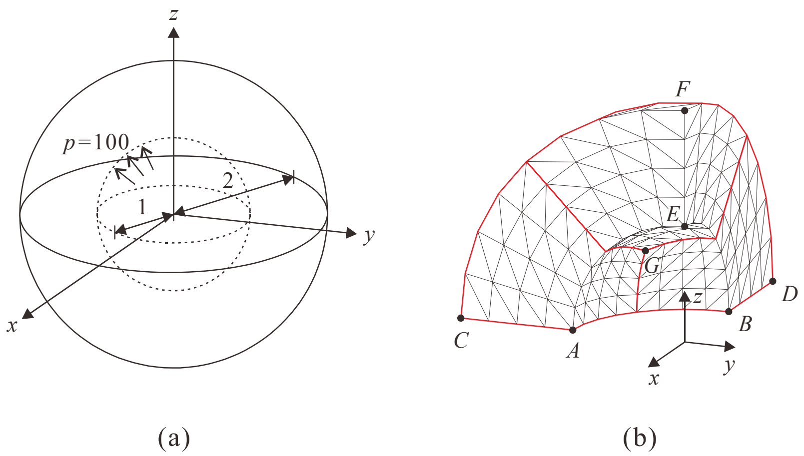

Fig. 2.14. Lame problem: (a) Problem description ($E = 1\times 10^3$ and $\nu = 0.3$). (b) Mesh used with $N = 4$.

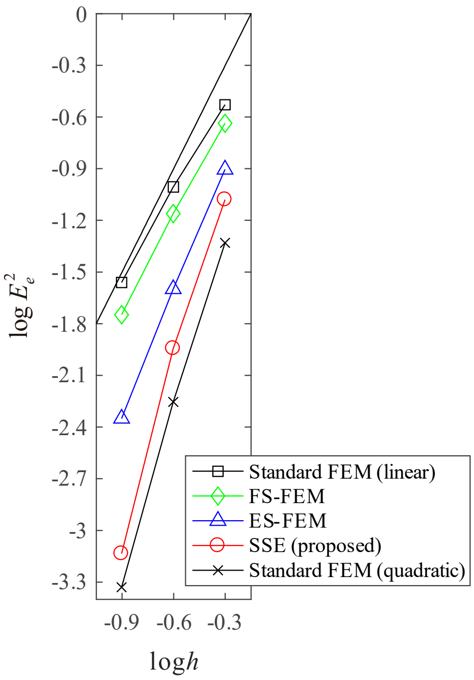

Fig. 2.15. Convergence curves for Lame problem: The bold line represents the optimal convergence rate for the linear elements. The element size is $h = 1/N$ for the linear elements and $h = 1/2N$ for the quadratic element.

Chapter 3. The strain-smoothed 4-node quadrilateral 2D solid finite elements

In this chapter, the SSE method is extended to a 4-node quadrilateral finite element and thus a strain-smoothed 4-node quadrilateral finite element is developed. The piecewise linear shape functions are adopted instead of the standard bilinear shape functions. The proposed strain-smoothed element has a bilinear strain field where the strains of neighboring elements are integrated within an element formulation.

We present the formulation of the strain-smoothed 4-node quadrilateral element including geometry and displacement interpolations, strain smoothing, strain-displacement relation and stiffness matrix.

3.1. Formulation of the strain-smoothed quadrilateral element

3.1.1. Geometry and displacement interpolations

Unlike the standard 4-node quadrilateral element, the element domain is subdivided into four non-overlapping triangular domains (from T1 to T4) based on its nodes and center point ($r = s = 0$) as shown in **Fig. 3.1**(a).

The piecewise linear shape functions $h_i(r,s)$ are defined for each sub-triangle [31]

$$h_1 = (1-2r-s)/4\,,\ \ h_2 = (1+2r-s)/4\,,\ \ h_3 = (1+s)/4\,,\ \ h_4 = (1+s)/4 \quad \text{on T1,} \tag{3.1}$$

$$h_1 = (1-r)/4\,,\ \ h_2 = (1+r-2s)/4\,,\ \ h_3 = (1+r+2s)/4\,,\ \ h_4 = (1-r)/4 \quad \text{on T2,} \tag{3.2}$$

$$h_1 = (1-s)/4\,,\ \ h_2 = (1-s)/4\,,\ \ h_3 = (1+2r+s)/4\,,\ \ h_4 = (1-2r+s)/4 \quad \text{on T3,} \tag{3.3}$$

$$h_1 = (1-r-2s)/4\,,\ \ h_2 = (1+r)/4\,,\ \ h_3 = (1+r)/4\,,\ \ h_4 = (1-r+2s)/4 \quad \text{on T4.} \tag{3.4}$$

Employing the shape functions in Eqs. (3.1)-(3.4), the geometry of the 4-node element is interpolated by

$$\mathbf{x} = \sum_{i=1}^{4} h_i(r,s)\mathbf{x}_i \quad \text{with} \quad \mathbf{x}_i = \begin{bmatrix} x_i & y_i \end{bmatrix}^T, \tag{3.5}$$

where $\mathbf{x}_i$ is the position vector of node i in the global Cartesian coordinate system as shown in **Fig. 3.1**(b).

The corresponding displacement interpolation is given by

$$\mathbf{u} = \sum_{i=1}^{4} h_i(r,s)\mathbf{u}_i \quad \text{with} \quad \mathbf{u}_i = \begin{bmatrix} u_i & v_i \end{bmatrix}^T, \tag{3.6}$$

in which $\mathbf{u}_i$ is the displacement vector of node i .

Fig. 3.2 illustrates the piecewise linear shape function h_3 in Eqs. (3.1)-(3.4) compared with the standard bilinear shape function, $\hat{h}_3 = (1+r)(1+s)/4$ [31,32].

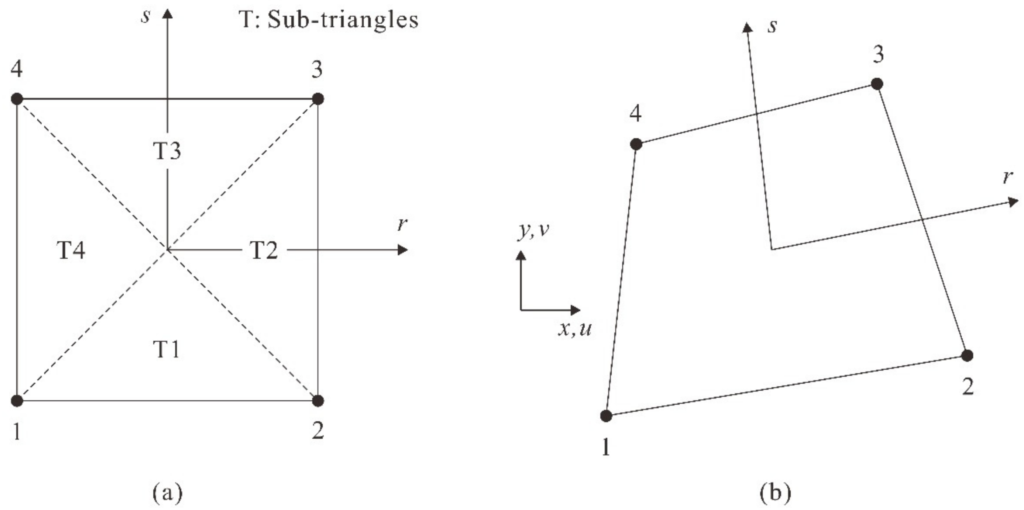

Fig. 3.1. A 4-node quadrilateral element in (a) the natural coordinate system and (b) the global Cartesian coordinate system. A triangular subdivision of the quadrilateral element is depicted in (a).

.

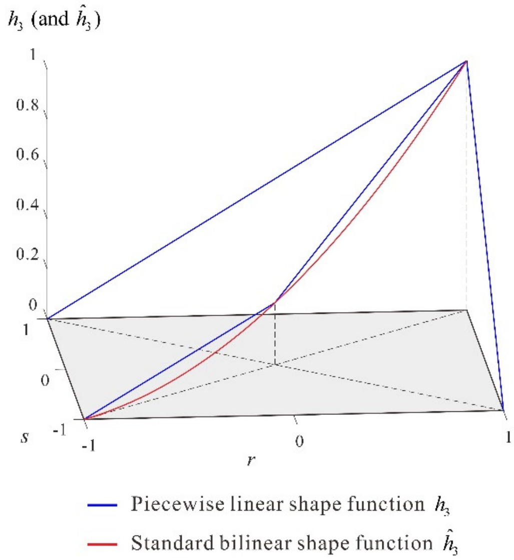

Fig. 3.2. Comparison of the standard bilinear and piecewise linear shape functions corresponding to node 3 along element edges and a diagonal $r = s$. The two shape functions show different variations along the diagonal.

3.1.2. Strain smoothing

Let us consider a 4-node quadrilateral element m in a finite element mesh as shown in **Fig. 3.3**. The strain field within the target element m can be calculated by employing the standard isoparametric finite element procedure as follows [1]

$$\boldsymbol{\varepsilon}^{(m)} = \nabla \mathbf{u}^{(m)}, \tag{3.7}$$

where $\boldsymbol{\varepsilon}^{(m)} = [\varepsilon_{xx} \quad \varepsilon_{yy} \quad 2\varepsilon_{xy}]^T$, ∇ is the gradient operator and $\mathbf{u}^{(m)}$ is the nodal displacement vector of the element.

Substituting Eqs. (3.1)-(3.6) into Eq. (3.7), the strain field in the k th sub-triangle of the target element m is defined by

$${}^{k}\boldsymbol{\varepsilon}^{(m)} = {}^{k}\mathbf{B}^{(m)}\mathbf{u}^{(m)} \quad \text{with} \quad k = 1, 2, 3, 4, \tag{3.8}$$

$${}^{k}\mathbf{B}^{(m)} = \left[{}^{k}\mathbf{B}_1 \quad {}^{k}\mathbf{B}_2 \quad {}^{k}\mathbf{B}_3 \quad {}^{k}\mathbf{B}_4 \right], \tag{3.9}$$

$$\mathbf{u}^{(m)} = [\mathbf{u}_1 \quad \mathbf{u}_2 \quad \mathbf{u}_3 \quad \mathbf{u}_4]^T, \tag{3.10}$$

where ${}^{k}\mathbf{B}^{(m)}$ is the strain-displacement relation matrix of the k th sub-triangle and ${}^{k}\mathbf{B}_i$ is the strain-displacement matrix corresponding to node i.

In the strain-smoothed element method, strains of neighboring elements are utilized to construct the strain field of the target element. The 4-node quadrilateral element can have up to four neighboring elements through its four edges as shown in **Fig. 3.3**. The smoothed strain between the k th sub-triangle of the target element m and its neighboring sub-triangle (belonging to the neighboring element) is defined by

$$\hat{\boldsymbol{\varepsilon}}^{(k)} = \frac{1}{A_k^{(m)} + A^{(k)}} (A_k^{(m)}\, {}^{k}\boldsymbol{\varepsilon}^{(m)} + A^{(k)}\boldsymbol{\varepsilon}^{(k)}) \quad \text{with} \quad k = 1, 2, 3, 4, \tag{3.11}$$

where $A_k^{(m)}$ and $A^{(k)}$ are the areas of the k th sub-triangle of the target element and its neighboring sub-triangle, respectively, seen in **Fig. 3.4**. If the k th sub-triangle is located on boundary, $\hat{\boldsymbol{\varepsilon}}^{(k)} = {}^{k}\boldsymbol{\varepsilon}^{(m)}$ is used [22].

As in the standard 4-node quadrilateral element, the 2×2 Gauss quadrature is adopted to calculate the stiffness matrix. As shown in **Fig. 3.5,** the smoothed strain values in Eq. (3.11) are simply assigned to the four integration points of the target element as follows

$$\bar{\boldsymbol{\varepsilon}}_1 = \frac{1}{A_4^{(m)} + A_1^{(m)}} (A_4^{(m)}\hat{\boldsymbol{\varepsilon}}^{(4)} + A_1^{(m)}\hat{\boldsymbol{\varepsilon}}^{(1)}) \quad \text{for Gauss point 1}, \tag{3.12}$$

$$\bar{\boldsymbol{\varepsilon}}_2 = \frac{1}{A_1^{(m)} + A_2^{(m)}} (A_1^{(m)}\hat{\boldsymbol{\varepsilon}}^{(1)} + A_2^{(m)}\hat{\boldsymbol{\varepsilon}}^{(2)}) \quad \text{for Gauss point 2}, \tag{3.13}$$

$$\bar{\boldsymbol{\varepsilon}}_3 = \frac{1}{A_2^{(m)} + A_3^{(m)}} (A_2^{(m)}\hat{\boldsymbol{\varepsilon}}^{(2)} + A_3^{(m)}\hat{\boldsymbol{\varepsilon}}^{(3)}) \quad \text{for Gauss point 3}, \tag{3.14}$$

$$\bar{\boldsymbol{\varepsilon}}_4 = \frac{1}{A_3^{(m)} + A_4^{(m)}} (A_3^{(m)} \hat{\boldsymbol{\varepsilon}}^{(3)} + A_4^{(m)} \hat{\boldsymbol{\varepsilon}}^{(4)}) \quad \text{for Gauss point 4,} \tag{3.15}$$

in which $\bar{\boldsymbol{\varepsilon}}_j$ is the strain value assigned to the Gauss point j.

It is interesting to note that the bilinear strain field of the target element m is represented in a form of assumed strain as follows

$$\bar{\boldsymbol{\varepsilon}}^{(m)} = \sum_{i=1}^{4} \bar{h}_i(r,s) \bar{\boldsymbol{\varepsilon}}_i \quad \text{with} \quad \bar{h}_i(r,s) = \frac{3}{4}\left(\frac{1}{\sqrt{3}} - \eta_i r\right)\left(\frac{1}{\sqrt{3}} - \zeta_i r\right), \tag{3.16}$$

and

$$\begin{bmatrix} \eta_1 & \eta_2 & \eta_3 & \eta_4 \end{bmatrix} = \begin{bmatrix} 1 & -1 & -1 & 1 \end{bmatrix}, \tag{3.17}$$

$$\begin{bmatrix} \zeta_1 & \zeta_2 & \zeta_3 & \zeta_4 \end{bmatrix} = \begin{bmatrix} 1 & 1 & -1 & -1 \end{bmatrix}. \tag{3.18}$$

Note that Eq. (3.16) is not utilized in the actual computation of the stiffness matrix and the assigned strains in Eqs. (3.12)-(3.15) are directly used in the 2×2 Gauss integration. The Jacobian determinant is constant for each sub-triangle and the value at a Gauss point is obtained by averaging the values of two adjacent sub-triangles. For example, the average of the determinants in sub-triangles 1 and 4 is assigned to Gauss point 1, see **Fig. 3.5**.

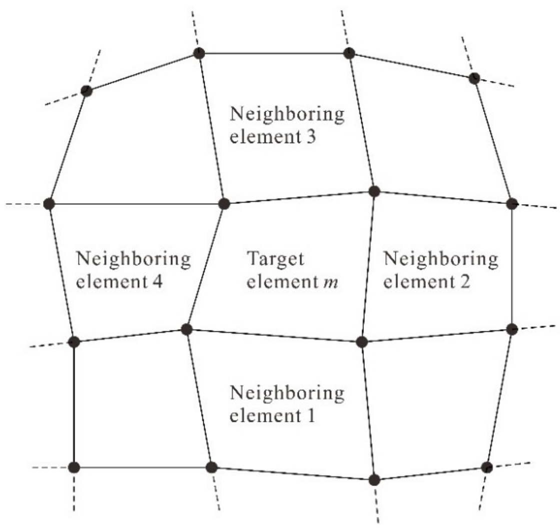

Fig. 3.3. Target element in a mesh and its four neighboring elements connected through element edges.

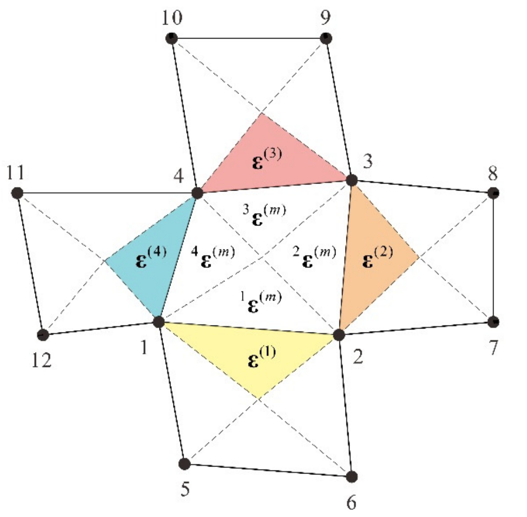

$$\hat{\boldsymbol{\varepsilon}}^{(k)} = \frac{1}{A_k^{(m)} + A^{(k)}}\left(A_k^{(m)}\,{}^{k}\boldsymbol{\varepsilon}^{(m)} + A^{(k)}\boldsymbol{\varepsilon}^{(k)}\right)$$

with $k = 1, 2, 3, 4$

Fig. 3.4. Strain smoothing through the edges of the target element. Four colored sub-triangles belong to four neighboring elements, respectively.

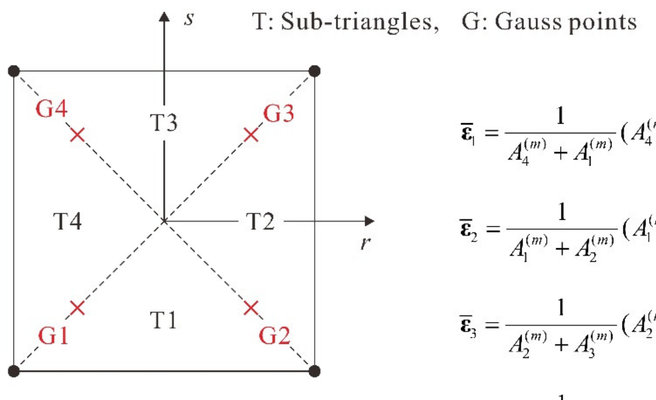

	r	s
G1	$-1/\sqrt{3}$	$-1/\sqrt{3}$
G2	$1/\sqrt{3}$	$-1/\sqrt{3}$
G3	$1/\sqrt{3}$	$1/\sqrt{3}$
G4	$-1/\sqrt{3}$	$1/\sqrt{3}$

$$\bar{\boldsymbol{\varepsilon}}_1 = \frac{1}{A_4^{(m)} + A_1^{(m)}}\left(A_4^{(m)}\,\hat{\boldsymbol{\varepsilon}}^{(4)} + A_1^{(m)}\,\hat{\boldsymbol{\varepsilon}}^{(1)}\right) \quad \text{for G1}$$

$$\bar{\boldsymbol{\varepsilon}}_2 = \frac{1}{A_1^{(m)} + A_2^{(m)}}\left(A_1^{(m)}\,\hat{\boldsymbol{\varepsilon}}^{(1)} + A_2^{(m)}\,\hat{\boldsymbol{\varepsilon}}^{(2)}\right) \quad \text{for G2}$$

$$\bar{\boldsymbol{\varepsilon}}_3 = \frac{1}{A_2^{(m)} + A_3^{(m)}}\left(A_2^{(m)}\,\hat{\boldsymbol{\varepsilon}}^{(2)} + A_3^{(m)}\,\hat{\boldsymbol{\varepsilon}}^{(3)}\right) \quad \text{for G3}$$

$$\bar{\boldsymbol{\varepsilon}}_4 = \frac{1}{A_3^{(m)} + A_4^{(m)}}\left(A_3^{(m)}\,\hat{\boldsymbol{\varepsilon}}^{(3)} + A_4^{(m)}\,\hat{\boldsymbol{\varepsilon}}^{(4)}\right) \quad \text{for G4}$$

Fig. 3.5. Smoothed strains assigned to four Gauss points.

3.1.3. Strain-displacement relation and stiffness matrix

In vector and matrix forms, for the target element m, the relation between the nodal displacement vector and the smoothed strain field is expressed as

$$\bar{\boldsymbol{\varepsilon}}^{(m)} = \bar{\mathbf{B}}^{(m)}\bar{\mathbf{u}}^{(m)} \tag{3.19}$$

with

$$\bar{\mathbf{B}}^{(m)} = \begin{bmatrix} \bar{\mathbf{B}}_1 & \bar{\mathbf{B}}_2 & \bar{\mathbf{B}}_3 & \bar{\mathbf{B}}_4 & \bar{\mathbf{B}}_5 & \cdots & \bar{\mathbf{B}}_{12} \end{bmatrix}, \tag{3.20}$$

$$\bar{\mathbf{u}}^{(m)} = \begin{bmatrix} \mathbf{u}_1 & \mathbf{u}_2 & \mathbf{u}_3 & \mathbf{u}_4 & \mathbf{u}_5 & \cdots & \mathbf{u}_{12} \end{bmatrix}, \tag{3.21}$$

where $\bar{\mathbf{B}}^{(m)}$ is the smoothed strain-displacement matrix and $\bar{\mathbf{u}}^{(m)}$ is the corresponding displacement vector of the element. The number of components in the strain-displacement relation matrix and the nodal displacement vector is determined by the total number of nodes in neighboring elements through element edges as shown in **Fig. 3.4**.

Finally, the stiffness matrix of the strain-smoothed 4-node quadrilateral finite element is obtained as

$$\mathbf{K}^{(m)} = \int_{V^{(m)}} \bar{\mathbf{B}}^{(m)T}\mathbf{C}^{(m)}\bar{\mathbf{B}}^{(m)}dV^{(m)}, \tag{3.22}$$

in which $V^{(m)}$ is the element volume and $\mathbf{C}^{(m)}$ is the material law matrix for the element *m*.

3.2. Basic numerical tests

Three basic numerical tests (the isotropic element, zero energy mode and patch tests) [1] are performed for the proposed strain-smoothed 4-node quadrilateral element.

The finite elements are required to be spatially isotropic, which means that the same response is obtained regardless of the element node numbering sequences. The proposed element satisfies this requirement.

A single 2D solid finite element with no support should have only three zero energy modes corresponding to the rigid body modes. Through the zero energy mode test, it is verified that the proposed element correctly possesses three zero energy modes.

The normal and shear patch tests are conducted using the mesh shown in **Fig. 3.6**. We can say that the patch tests are passed if a constant stress field is correctly formed within the elements under the minimum number of constraints in nodal DOFs to prevent rigid body motions. The proposed element passes the patch tests.

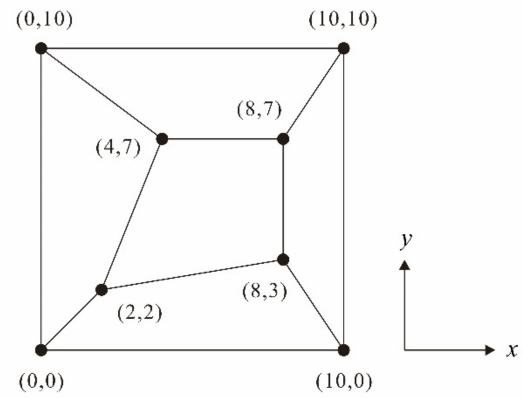

Fig. 3.6. Mesh used for the patch tests.

3.3. Numerical examples

In this section, we demonstrate the performance of the strain-smoothed 4-node quadrilateral element by solving various numerical problems: Cook's skew beam, a block under complex forces, an infinite plate with a central hole, an L-shaped structure, and a dam problem.

The standard 4-node quadrilateral element (Q4), the edge-based smoothed 4-node quadrilateral element (ES-Q4) [12] and the incompatible modes 4-node quadrilateral element (ICM-Q4) [35-37] are considered for the performance comparison with the proposed 4-node element (SSE-Q4). It is well known that the edge-based S-FEM performs better than cell and node-based S-FEMs.

For the convergence studies, we evaluate displacements at specific locations, von Mises stress distributions and energy norms. The following relative error E_e^2 in an energy norm $\|\mathbf{u}\|_e$ is utilized

$$E_e^2 = \frac{\left| \|\mathbf{u}_{ref}\|_e^2 - \|\mathbf{u}_h\|_e^2 \right|}{\|\mathbf{u}_{ref}\|_e^2} \quad \text{with} \quad \|\mathbf{u}\|_e^2 = \int_{\Omega} \boldsymbol{\varepsilon}^T \boldsymbol{\sigma} d\Omega \,, \tag{3.23}$$

where the reference and finite element solutions are denoted by the subscripts '*ref*' and '*h*', respectively.

The optimal convergence behavior of linear elements for the relative error is expected to be

$$E_e^2 \cong ch^2 \,, \tag{3.24}$$

in which c is a constant and h represents the element size [1].

To create distorted meshes for finite element models, we construct them for a square by repositioning the interior nodes of regular meshes randomly as follows:

$$x' = x - \alpha h_x, \tag{3.25}$$

$$y' = y + \beta\gamma h_y, \tag{3.26}$$

where (x, y) and (x', y') are the nodal coordinates in the regular and distorted meshes, respectively, h_x and h_y are the regular element sizes in the x - and y -directions, respectively, and $\alpha, \beta \in [0.3, 0.4]$ and γ (having a random value of 1 or -1) are random constants, see **Fig. 3.7**. The distorted meshes in the square domain in **Fig. 3.7** are linearly mapped to obtain distorted meshes in domains of different shapes.

The reference solutions are either analytical solutions or well-converged numerical solutions calculated using 9-node quadrilateral finite elements.

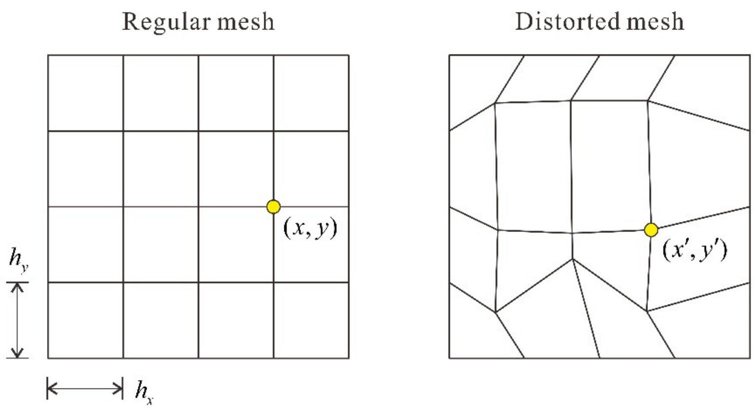

Fig. 3.7. Regular and distorted meshes when $N = 4$.

3.3.1. Cook's skew beam

We solve the well-known Cook's skew beam problem as shown in **Fig. 3.8** [3]. The left edge of the beam structure is clamped, and a distributed shearing force $f_S = 1/16$ (force per length) is acting on the right edge. The plane stress condition is considered with Young's modulus $E = 3\times10^7$ and Poisson's ratio $\nu = 0.3$. The solutions are obtained for both regular and distorted $N \times N$ meshes (N = 2, 4, 8 and 16). The distorted meshes used for the problem are depicted in **Fig. 3.9**.

Convergences in the normalized horizontal and vertical displacements at point A are depicted in **Figs. 3.10** and **3.11**, respectively. The relative errors in the horizontal and vertical displacements are given in **Tables 3.1** and **3.2**, respectively. The convergence curves obtained using the energy norm in Eq. (3.23) are presented in **Fig. 3.12**. A 256×256 mesh of 9-node quadrilateral elements is used to calculate the reference solutions. The proposed strain-smoothed element shows the best convergence behavior among the compared elements in both regular and distorted meshes.

In addition, we compare the computational efficiency of the considered elements by plotting the relations between computation times versus solution accuracies (relative errors in the energy norm) as shown in **Fig. 3.13**. The regular meshes with N = 32, 64 and 128 are used for the assessment. Computations are performed in a personal computer (PC) with Intel Core i7-6700, 3.40GHz CPU and 64GB RAM. The compressed sparse row format is used for storing matrices and Intel MKL PARDISO is used for solving a linear system of equations [38]. Computation times taken from obtaining the stiffness matrices to solving the linear equations are measured. At similar accuracy levels, the proposed element gives less computation times compared with other elements. That is, the proposed element provides the best computational efficiency among the elements considered.

3.3.2. Block under complex forces

A square block is subjected to a compressive body force $f_B = (y+1)^2$ (force per area) and an eccentric tensile traction $f_S = 3.2$ (force per length) in the y-direction as shown in **Fig. 3.14**. The block is supported along its bottom, and the plane stress condition is employed with Young's modulus $E = 3\times10^7$ and Poisson's ratio $\nu = 0.25$. We use both regular and distorted meshes of $N \times N$ elements (N = 2, 4, 8 and 16) to obtain solutions. The configurations of the distorted meshes used for the problem are given in **Fig. 3.15**.

The von Mises stress distributions calculated for the entire model and along the line $x = -1$ (left edge) are depicted in **Figs. 3.16** and **3.17**, respectively, for the regular meshes. The proposed strain-smoothed element provides the most converged stress fields to the reference for all the meshes considered. In **Fig. 3.18**, the convergence curves obtained using the energy norm in Eq. (3.23) are presented. The reference solutions are obtained using a 64×64 mesh of 9-node quadrilateral elements. The proposed element gives much better convergence behaviors compared with the standard, edge-based smoothed and incompatible modes 4-node elements, especially for the distorted meshes.

3.3.3. Infinite plate with a central hole

The problem of an infinite plate with a central hole of radius $a = 1$ shown in **Fig. 3.19**(a) is solved [4,22]. A far field traction $p = 1$ acts only in the x-direction on the infinite plate. The plane strain condition is adopted with $E = 3 \times 10^7$ and $\nu = 0.3$. Only one-quarter of the plate is modeled due to symmetry as shown in **Fig. 3.19**(b), and the corresponding boundary conditions are imposed as: $u = 0$ along AC and $v = 0$ along BD.

The traction boundary conditions are given along CE and DE using the following analytical solutions [33]:

$$\sigma_{xx}(r,\theta) = p - \frac{a^2 p}{r^2}\left[\frac{3}{2}\cos 2\theta + \cos 4\theta\right] + \frac{3a^4 p}{2r^4}\cos 4\theta\,, \tag{3.27}$$

$$\sigma_{yy}(r,\theta) = -\frac{a^2 p}{r^2}\left[\frac{1}{2}\cos 2\theta - \cos 4\theta\right] - \frac{3a^4 p}{2r^4}\cos 4\theta\,, \tag{3.28}$$

$$\sigma_{xy}(r,\theta) = -\frac{a^2 p}{r^2}\left[\frac{1}{2}\sin 2\theta + \sin 4\theta\right] + \frac{3a^4 p}{2r^4}\sin 4\theta\,, \tag{3.29}$$

where r and θ are the distance from the origin ($x = y = 0$) and the counterclockwise angle from the positive x-axis, respectively.

The modeled region of dimensions 5×5 is divided into two areas, and each area is meshed with $N \times N$ finite elements (N = 2, 4, 8 and 16) as shown in **Fig. 3.19**(b).

Table 3.3 and **Fig. 3.20** show relative errors in the horizontal displacement at point B and the convergence curves obtained using the energy norm in Eq. (3.23), respectively. A 64×64 mesh of 9-node quadrilateral elements is used to obtain the reference solutions. Compared with the standard, edge-based smoothed and incompatible modes quadrilateral elements, the proposed element shows a significantly improved solution accuracy.

3.3.4. L-shaped structure

An L-shaped structure under a distributed load $f_S = 1$ (force per length) is considered as shown in **Fig. 3.21** [39]. The plane stress condition is used with material properties $E = 1$ and $\nu = 0.22$, and the boundary conditions are imposed as: $v = 0$ along AB and $u = 0$ along CD. The structure is divided into three square parts, and each part is modeled with $N \times N$ element meshes (N = 2, 4, 8 and 16) to obtain the solutions.

Table 3.4 and **Fig. 3.22** give relative errors in the horizontal displacement at point B and convergence curves calculated using the energy norm in Eq. (3.23), respectively. The reference solutions are calculated using a 64×64 mesh of 9-node quadrilateral elements. The strain-smoothed quadrilateral element produces much more accurate solutions than using the standard, edge-based smoothed and incompatible modes quadrilateral elements.

3.3.5. Dam problem

Finally, we consider the dam problem as shown in **Fig. 3.23**. The structure is subjected to a varying surface force along its left edge given by

$$f_S = \begin{cases} 5-y & 0 \le y \le 5 \\ (y-5)^{1/5} & 5 \le y \le 10 \end{cases} . \tag{3.30}$$

The bottom of the structure is clamped. The plane strain condition is employed and the material properties are given as $E = 3\times 10^{10}$ and $\nu = 0.2$. The finite element models are constructed using meshes of $N \times 2N$ elements with N = 2, 4, 8 and 16.

Figs. 3.24 and **3.25** present distributions of the strain component ε_{xx} and the convergence curves obtained using the energy norm in Eq. (3.23), respectively. A mesh of 9-node quadrilateral elements with $N = 64$ is used for calculating the reference solutions. It is again observed that the strain-smoothed 4-node element gives highly accurate solutions compared with the other elements considered.

Table 3.1. Relative errors in the horizontal displacement ($\left|u_{ref} - u_h\right| / u_{ref} \times 100$) at point A in Cook's skew beam.

	N	Q4	ES-Q4	ICM-Q4	SSE-Q4
Regular mesh	2	61.421	49.332	48.012	24.177
	4	25.730	11.832	11.242	1.210
	8	8.058	2.941	3.150	0.042
	16	2.378	1.018	0.901	0.076
Distorted mesh	2	50.316	47.323	44.635	23.230
	4	23.050	12.964	6.079	1.845
	8	7.833	3.694	4.680	0.173
	16	1.866	1.114	0.776	0.223
Reference solution: $u_{ref} = -1.535\times 10^{-7}$					

Table 3.2. Relative errors in the vertical displacement ($\left|v_{ref}-v_h\right|/v_{ref}\times 100$) at point A in Cook's skew beam.

	N	Q4	ES-Q4	ICM-Q4	SSE-Q4
Regular mesh	2	50.095	42.784	13.102	16.987
	4	22.986	10.724	3.612	0.627
	8	7.705	2.233	1.225	0.012
	16	2.337	0.709	0.447	0.114
Distorted mesh	2	52.121	50.214	28.423	30.899
	4	31.221	19.855	8.983	4.957
	8	9.784	4.083	2.228	0.603
	16	2.992	1.205	0.754	0.385
Reference solution: $v_{ref}=7.721\times 10^{-7}$					

Table 3.3. Relative errors in the horizontal displacement ($\left|u_{ref}-u_h\right|/u_{ref}\times 100$) at point B in the infinite plate with a central hole.

N	Q4	ES-Q4	ICM-Q4	SSE-Q4
2	18.965	25.120	11.922	9.334
4	10.568	11.485	7.176	3.240
8	4.313	3.892	3.170	0.413
16	1.339	0.859	1.009	0.371
Analytical solution: $u_{ref}=9.100\times 10^{-8}$				

Table 3.4. Relative errors in the horizontal displacement ($\left|u_{ref}-u_h\right|/u_{ref}\times 100$) at point B in the L-shaped structure.

N	Q4	ES-Q4	ICM-Q4	SSE-Q4
2	15.816	15.668	9.465	0.872
4	5.517	4.287	3.358	1.485
8	1.874	1.251	1.206	0.530
16	0.657	0.415	0.448	0.165
Reference solution: $u_{ref}=-4.539\times 10^{2}$				

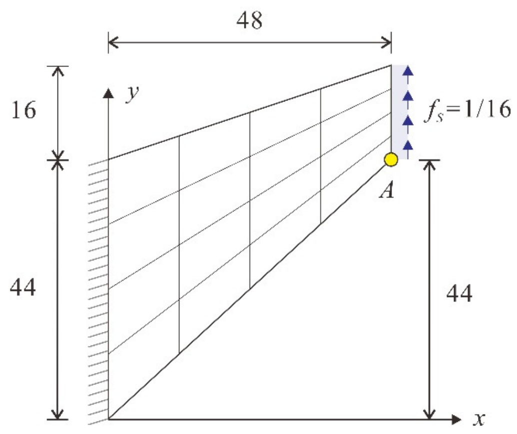

Fig. 3.8. Cook's skew beam ($E = 3\times10^7$, $\nu = 0.3$ and regular 4×4 mesh).

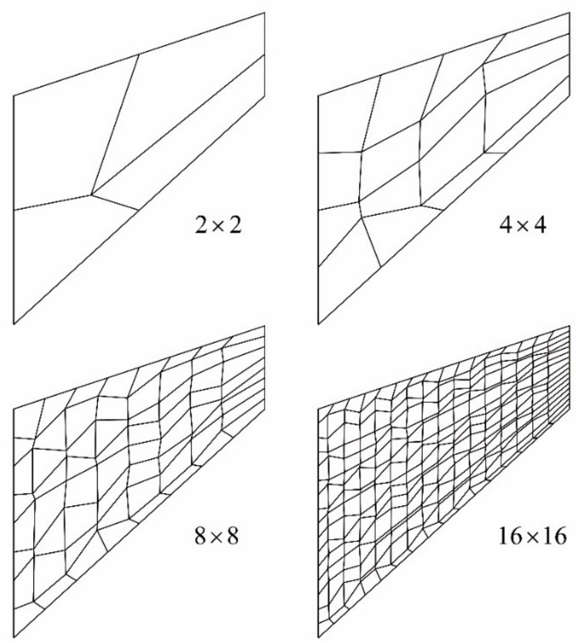

Fig. 3.9. Distorted meshes used for Cook's skew beam.

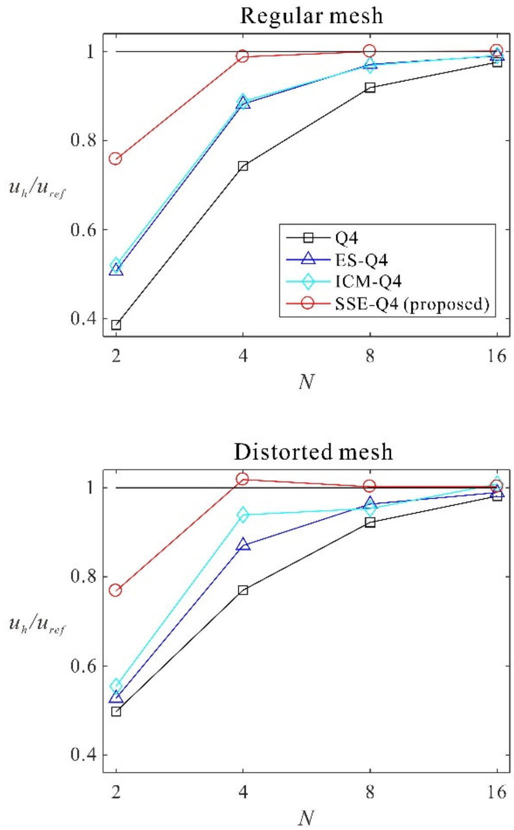

Fig. 3.10. Normalized horizontal displacements (u_h / u_{ref}) at point A in Cook's skew beam.

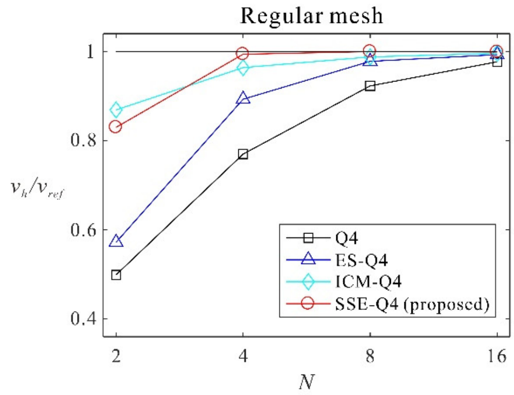

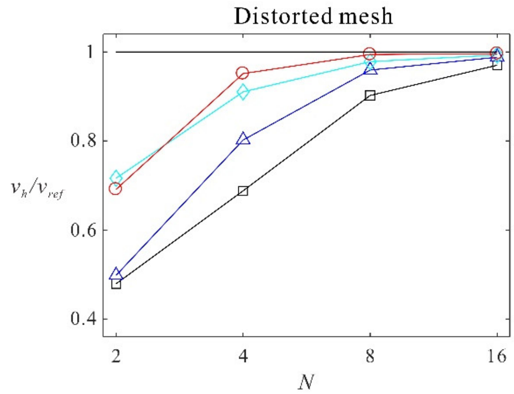

Fig. 3.11. Normalized vertical displacements (v_h / v_{ref}) at point A in Cook's skew beam.

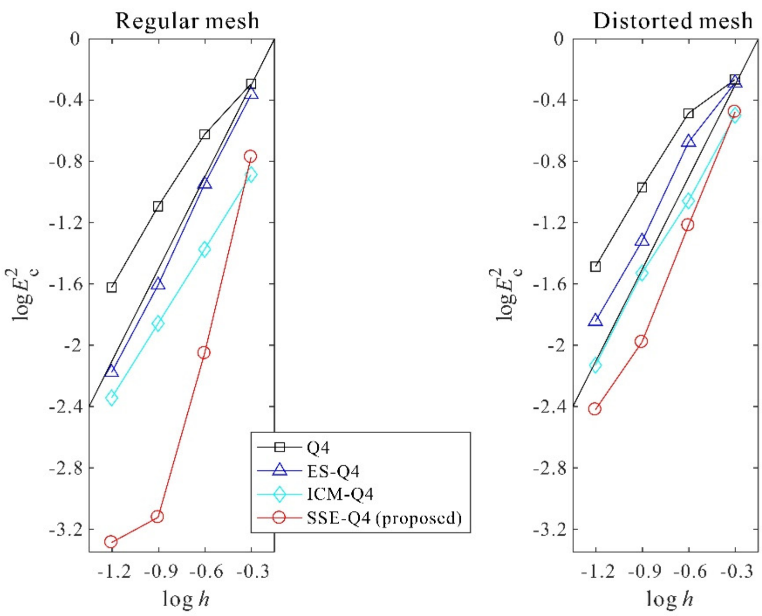

Fig. 3.12. Convergence curves for Cook's skew beam. The bold line represents the optimal convergence rate.

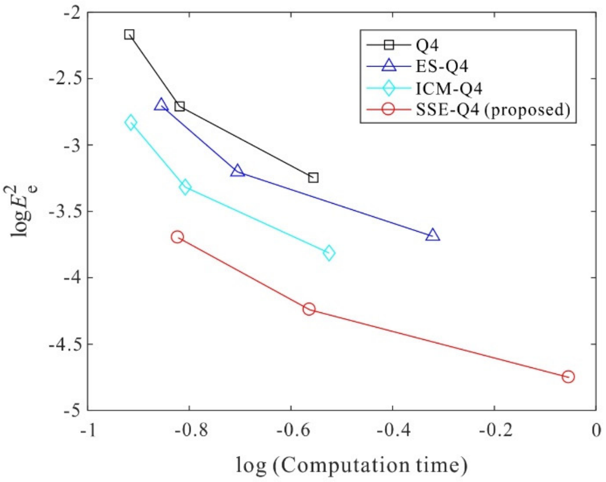

Fig. 3.13. Computational efficiency curves for Cook's skew beam. The computation times are measured in seconds.

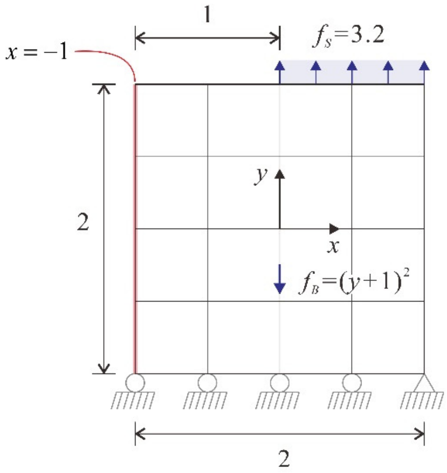

Fig. 3.14. Block under complex forces ($E=3\times10^7$, $\nu=0.25$ and regular 4×4 mesh).

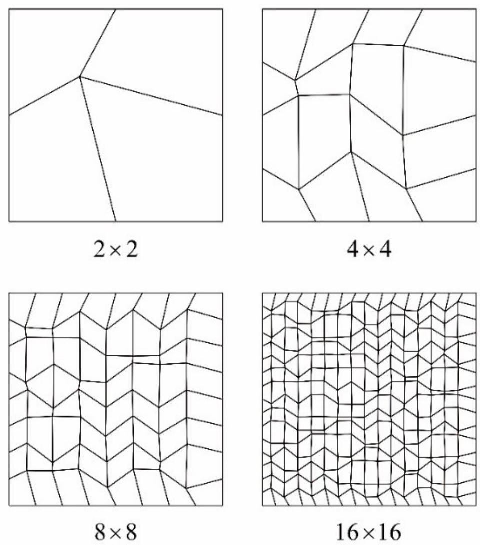

Fig. 3.15. Distorted meshes used for the block under complex forces.

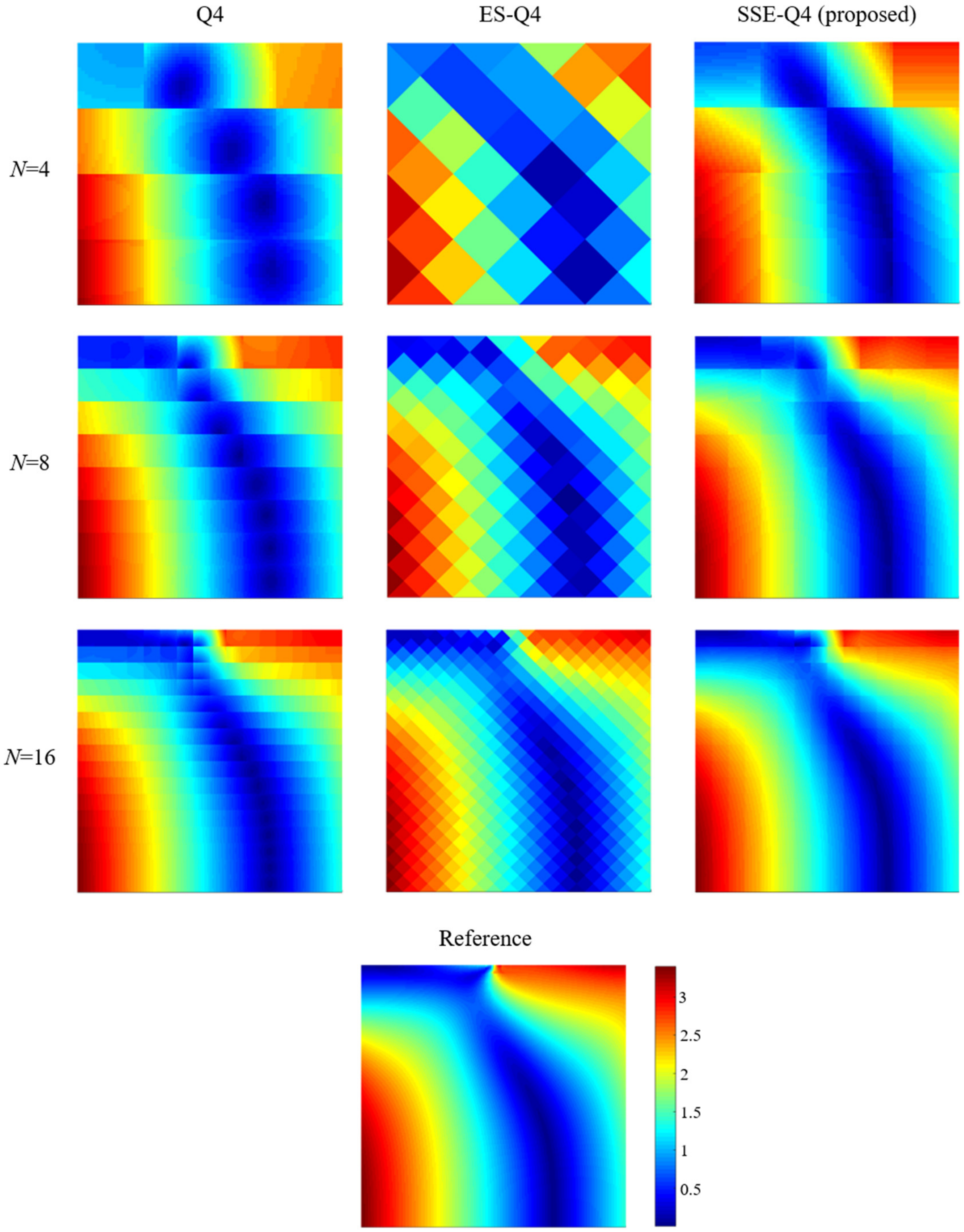

Fig. 3.16. von Mises stress distributions of the block under complex forces when using regular meshes. The reference stress distribution is obtained using a 32×32 mesh of 9-node quadrilateral elements.

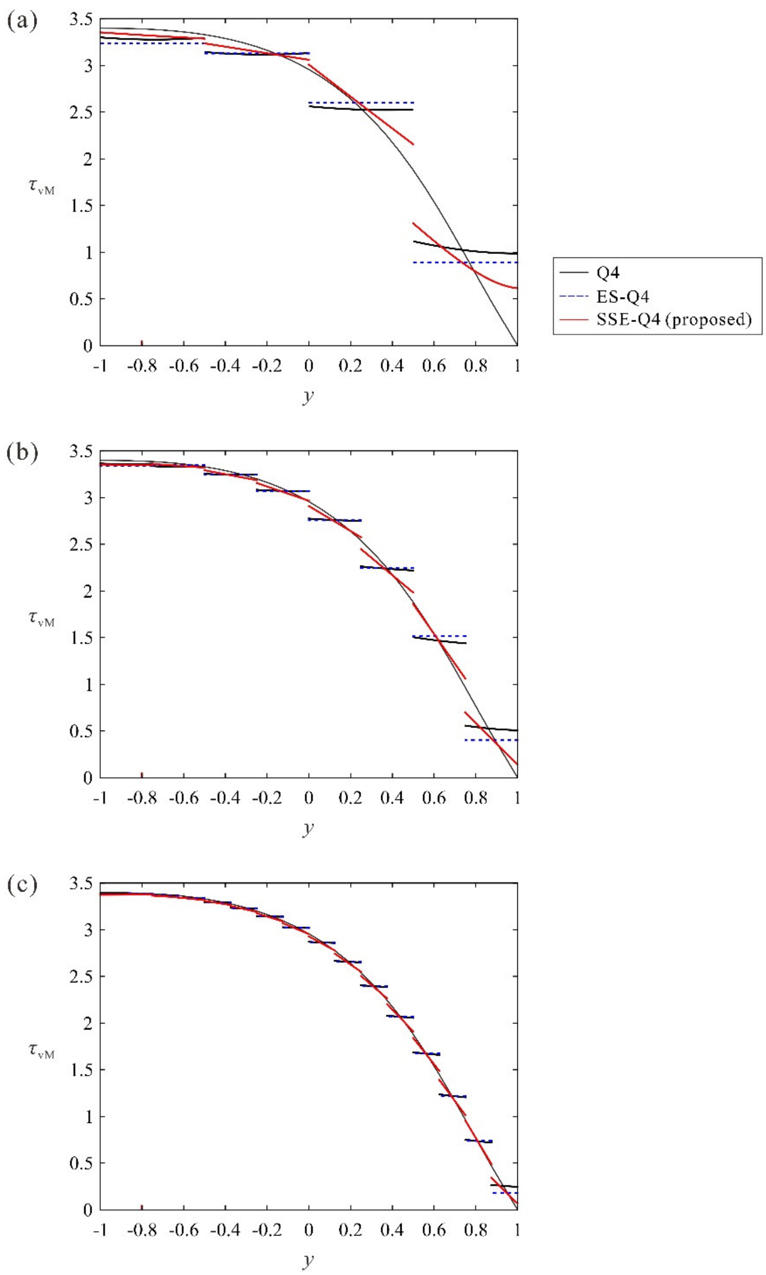

Fig. 3.17. von Mises stress distributions along the line $x = -1$ of the block under complex forces for (a) 4×4, (b) 8×8 and (c) 16×16 regular meshes used.

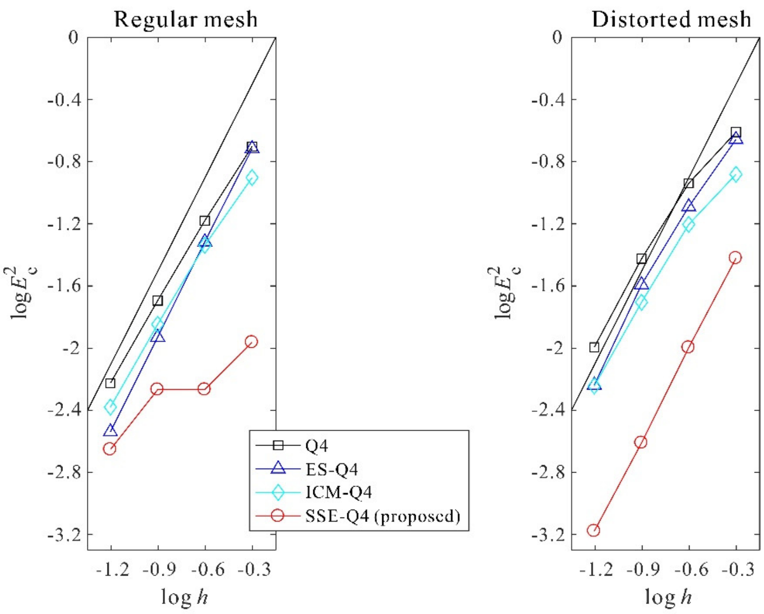

Fig. 3.18. Convergence curves for the block under complex forces. The bold line represents the optimal convergence rate.

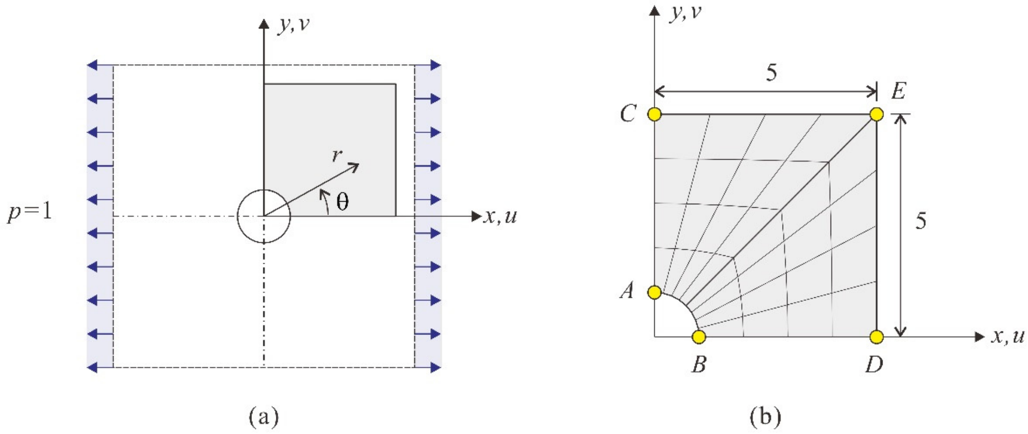

Fig. 3.19. Infinite plate with a central hole of radius $a = 1$: (a) Problem description ($E = 3\times10^7$ and $\nu = 0.3$). (b) 4×4 element mesh for the shaded domain in (a).

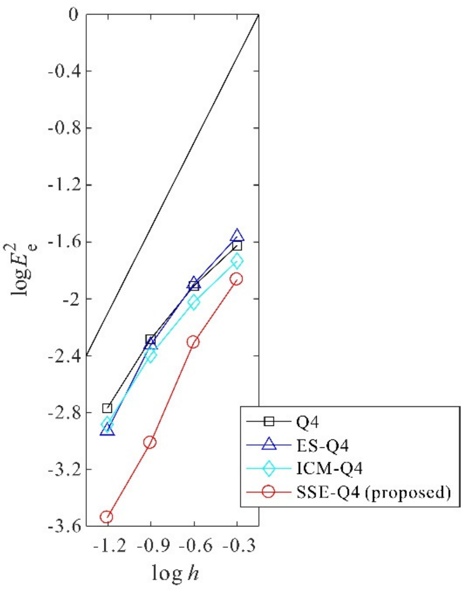

Fig. 3.20. Convergence curves for the infinite plate with a central hole. The bold line represents the optimal convergence rate.

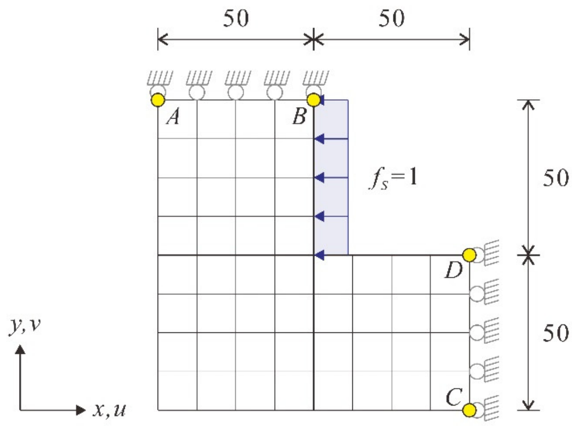

Fig. 3.21. L-shaped structure ($E = 1$, $\nu = 0.22$ and 4×4 mesh).

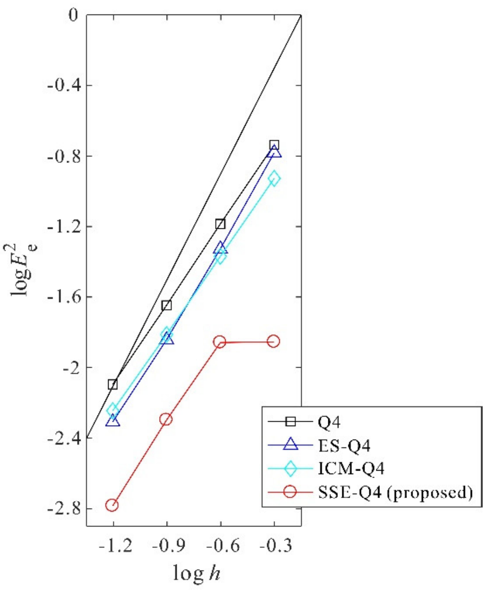

Fig. 3.22. Convergence curves for the L-shaped structure. The bold line represents the optimal convergence rate.

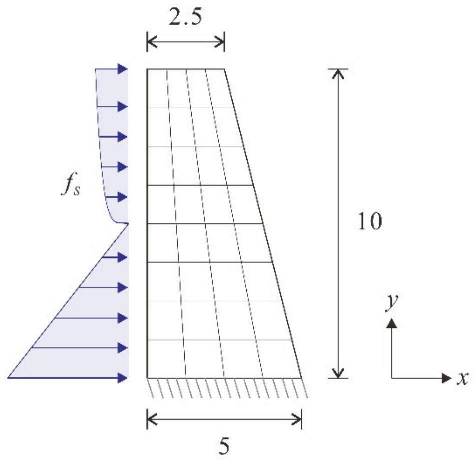

Fig. 3.23. Dam problem ($E = 3\times10^{10}$, $\nu = 0.2$ and 4×8 mesh).

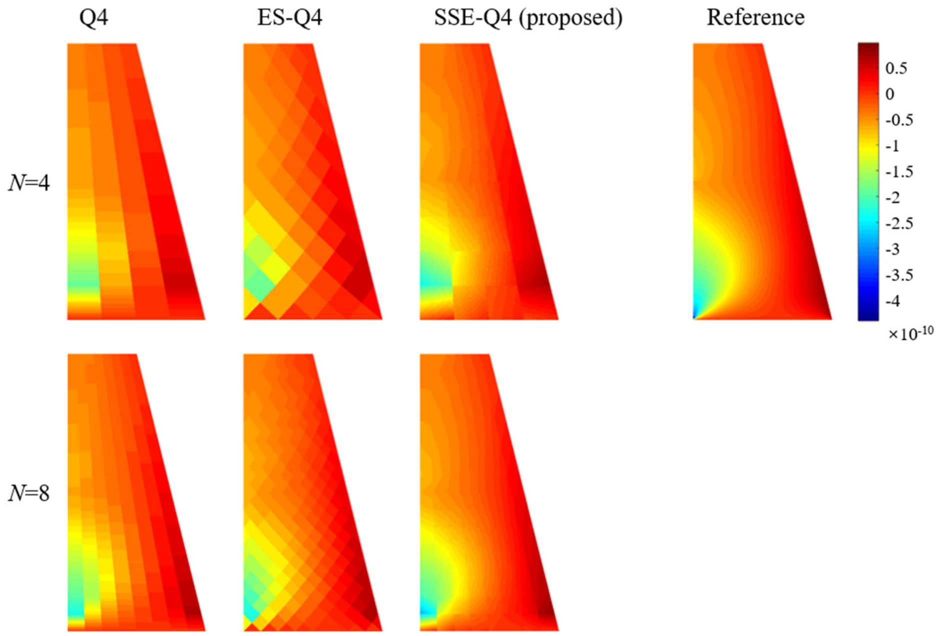

Fig. 3.24. Strain distributions (ε_{xx}) for the dam problem. The reference strain distribution is obtained using a 32×64 mesh of 9-node quadrilateral elements.

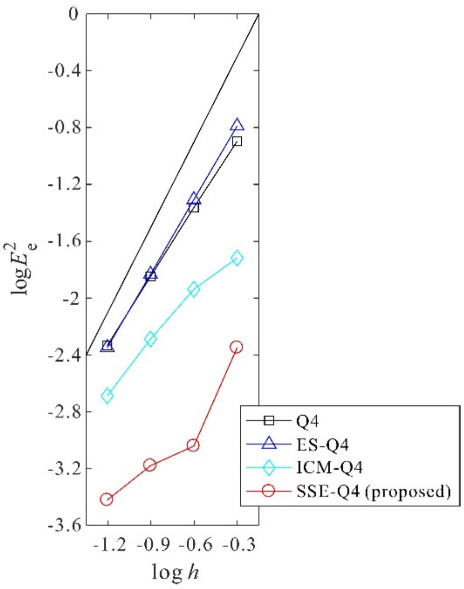

Fig. 3.25. Convergence curves for the dam problem. The bold line represents the optimal convergence rate.

Chapter 4. The strain-smoothed MITC3+ shell element

Shell structures have been widely used for manufacturing automobiles, airplanes and ships due to their excellent strength to weight ratio. Finite element method is the main tool for such analysis of shell structures, in which it is important to develop ideal shell finite elements. Among various shell finite elements, 3-node triangular shell elements have the obvious advantages of being simple and efficient.

Shell finite elements inherently have locking problems which happen when the finite element discretization cannot accurately represent pure bending displacement fields. Locking seriously deteriorates solution accuracy as the shell thickness decreases in bending-dominated shell problems. There are various methods to alleviate locking such as reduced integration and assumed strain methods [40-62]. Among those methods, the mixed interpolation of tensorial components (MITC) method was significantly successful [50-62].

Recently, the 3-node MITC3+ triangular shell element was developed based on the MITC method to reduce shear locking for out of plane bending behaviors. The shell element shows almost optimal convergence behavior in bending-dominated shell problems. However, shear locking for in-plane bending behaviors was not treated and thus its membrane performance is the same as that of displacement-based 3-node triangular shell element.

In this chapter, a strain-smoothed MITC3+ shell element is proposed by adopting the strain-smoothed element (SSE) method to the MITC3+ shell element. After reviewing the formulations of the displacement-based 3-node triangular shell elements and the MITC3+ shell finite element, the formulation of the strain-smoothed MITC3+ shell finite element is presented [25].

4.1. The displacement-based 3-node triangular shell finite element

The geometry of the 3-node triangular displacement-based shell finite element is interpolated by [54]

$$\vec{x}(r,s,t) = \sum_{i=1}^{3} h_i(r,s)\vec{x}_i + \frac{t}{2}\sum_{i=1}^{3} a_i h_i(r,s)\vec{V}_n^i \quad \text{with} \quad h_1 = 1-r-s\,,\;\; h_2 = r\,,\;\; h_3 = s\,,$$

where h_i is the 2D interpolation function of the standard isoparametric procedure corresponding to node i, $\vec{x}_i$ is the position vector at node i in the global Cartesian coordinate system, and a_i and $\vec{V}_n^i$ denote the shell thickness and the director vector at the node i, respectively, see **Fig 4.1**. Note that the vector $\vec{V}_n^i$ does not have to be normal to the shell midsurface in this description.

The corresponding displacement interpolation of the element is given by

$$\vec{u}(r,s,t)=\sum_{i=1}^{3}h_i(r,s)\vec{u}_i+\frac{t}{2}\sum_{i=1}^{3}a_i h_i(r,s)\left(-\alpha_i\vec{V}_2^i+\beta_i\vec{V}_1^i\right),$$

where $\vec{u}_i$ is the nodal displacement vector in the global Cartesian coordinate system, $\vec{V}_1^i$ and $\vec{V}_2^i$ are unit vectors orthogonal to $\vec{V}_n^i$ and to each other, and α_i and β_i are the rotations of the director vector $\vec{V}_n^i$ about $\vec{V}_1^i$ and $\vec{V}_2^i$ at node i.

The linear part of the displacement-based covariant strains is calculated by

$$e_{ij}=\frac{1}{2}(\vec{g}_i\cdot\vec{u}_{,j}+\vec{g}_j\cdot\vec{u}_{,i}),$$

where

$$\vec{g}_i=\frac{\partial\vec{x}}{\partial r_i},\quad \vec{u}_{,i}=\frac{\partial\vec{u}}{\partial r_i}\quad\text{with}\quad r_1=r,\ r_2=s,\ r_3=t.$$

The 3-node triangular displacement-based shell finite element passes all basic numerical tests: zero energy mode test, isotropic test and patch tests. However, this shell finite element strongly has the shear locking problem and therefore, it exhibits extremely stiff behaviors in bending-dominated problems.

4.2. The MITC3+ shell finite element

In the geometry and displacement interpolations, the MITC3+ shell finite element has an internal bubble node at element center ($r=s=1/3$) that only has two rotational degrees of freedom with a cubic bubble function.

The geometry of the MITC3+ shell finite element, shown in **Fig. 4.1**, is interpolated by [24]

$$\mathbf{x}(r,s,t)=\sum_{i=1}^{3}h_i(r,s)\mathbf{x}_i+\frac{t}{2}\sum_{i=1}^{4}a_i f_i(r,s)\mathbf{V}_n^i, \tag{4.1}$$

$$\text{with}\quad h_1=1-r-s,\ h_2=r,\ h_3=s,\ a_4\mathbf{V}_n^4=\frac{1}{3}\left(a_1\mathbf{V}_n^1+a_2\mathbf{V}_n^2+a_3\mathbf{V}_n^3\right), \tag{4.2}$$

where $h_i(r,s)$ is the 2D interpolation function of the standard isoparametric procedure corresponding to node i, $\mathbf{x}_i$ is the position vector of node i in the global Cartesian coordinate system, a_i and $\mathbf{V}_n^i$ are the shell thickness and the director vector at node i, respectively, and $f_i(r,s)$ is the 2D interpolation function with the cubic bubble function f_4 corresponding to internal node 4:

$$f_1=h_1-\frac{1}{3}f_4,\ f_2=h_2-\frac{1}{3}f_4,\ f_3=h_3-\frac{1}{3}f_4,\ f_4=27rs(1-r-s). \tag{4.3}$$

The displacement interpolation of the element is given by

$$\mathbf{u}(r,s,t)=\sum_{i=1}^{3}h_i(r,s)\mathbf{u}_i+\frac{t}{2}\sum_{i=1}^{4}a_i f_i(r,s)\left(-\alpha_i\mathbf{V}_2^i+\beta_i\mathbf{V}_1^i\right), \tag{4.4}$$

in which $\mathbf{u}_i$ is the nodal displacement vector in the global Cartesian coordinate system, $\mathbf{V}_1^i$ and $\mathbf{V}_2^i$ are unit vectors orthogonal to $\mathbf{V}_n^i$ and to each other, and α_i and β_i are the rotations of the director vector $\mathbf{V}_n^i$ about $\mathbf{V}_1^i$ and $\mathbf{V}_2^i$, respectively, at node i. Note that the displacement interpolation has a linear variation along its edges.

The linear part of the displacement-based covariant strain components is obtained by

$$e_{ij}=\frac{1}{2}(\mathbf{g}_i\cdot\mathbf{u}_{,j}+\mathbf{g}_j\cdot\mathbf{u}_{,i})\,, \tag{4.5}$$

$$\text{with}\quad \mathbf{g}_i=\frac{\partial\mathbf{x}}{\partial r_i},\quad \mathbf{u}_{,i}=\frac{\partial\mathbf{u}}{\partial r_i}\quad \text{with}\quad r_1=r,\ \ r_2=s,\ \ r_3=t\,, \tag{4.6}$$

where $\mathbf{g}_i$ and $\mathbf{u}_{,i}$ are the covariant base vectors and the displacement derivatives, respectively.

To alleviate transverse shear locking, the following assumed covariant transverse shear strain fields with six tying points are employed for the MITC3+ shell element [24]

$$e_{13}^{MITC3+}=\frac{2}{3}\left(e_{13}^{(B)}-\frac{1}{2}e_{23}^{(B)}\right)+\frac{1}{3}\left(e_{13}^{(A)}+e_{23}^{(A)}\right)+\frac{1}{3}\hat{c}(3s-1)\,, \tag{4.7}$$

$$e_{23}^{MITC3+}=\frac{2}{3}\left(e_{23}^{(C)}-\frac{1}{2}e_{13}^{(C)}\right)+\frac{1}{3}\left(e_{13}^{(A)}+e_{23}^{(A)}\right)+\frac{1}{3}\hat{c}(1-3r)\,, \tag{4.8}$$

where $\hat{c}=e_{13}^{(F)}-e_{13}^{(D)}-e_{23}^{(F)}+e_{23}^{(E)}$ and the tying points *(A)-(F)* are given in **Fig. 4.2** and **Table 4.1**.

In order to calculate the stiffness matrix, in principle, the 7-point Gauss integration should be used in the $r-s$ plane, but the 3-point Gauss integration also gives similar results. For this study, the 3-point Gauss integration is adopted. Note that in the MITC3+ shell element, membrane locking is not treated due to its flat geometry.

The MITC3+ shell finite element passes all the basic tests; zero energy mode, isotropy and patch tests, and shows excellent convergence behaviors in both linear and nonlinear analyses of various shell problems [24,57].

Table 4.1. Tying points (A)-(F) for the assumed transverse shear strain fields of the MITC3+ shell element. The distance d is defined in **Fig. 4.2**, and d = 1/10000 is recommended [24].

	Tying points	*r*	*s*
	(A)	1/6	1/6
Fig. 4.2(a)	*(B)*	2/3	1/6
	(C)	1/6	2/3
	(D)	$1/3 + d$	$1/3 - 2d$
Fig. 4.2(b)	*(E)*	$1/3 - 2d$	$1/3 + d$
	(F)	$1/3 + d$	$1/3 + d$

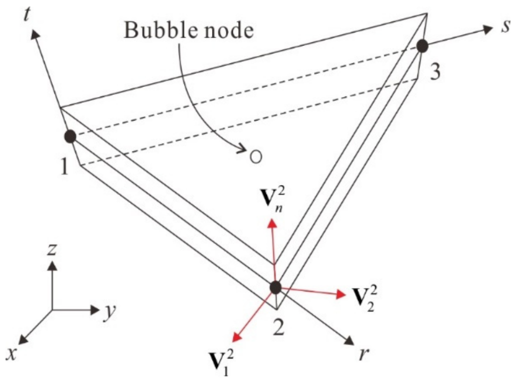

Fig. 4.1. Geometry of the MITC3+ shell finite element.

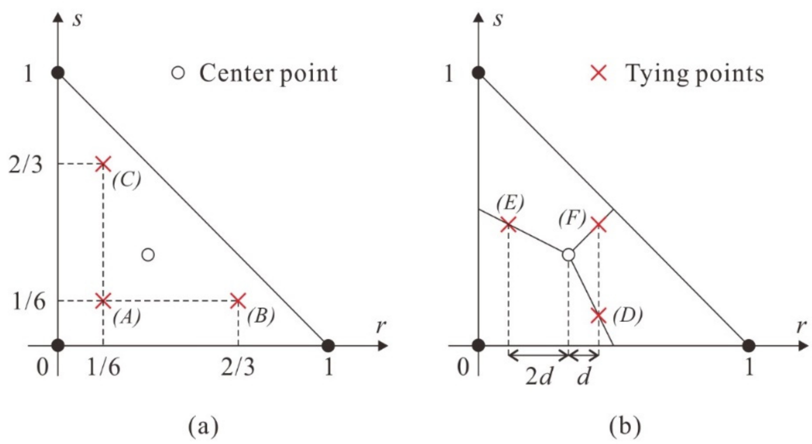

Fig. 4.2. Tying points (A)-(F) for the assumed transverse shear strain fields of the MITC3+ shell element. The points (A)-(C) also correspond to Gauss integration points.

4.3. The strain-smoothed MITC3+ shell finite element

The covariant in-plane strain components in Eq. (4.5) can be decomposed as follows

$$e_{ij} = {}^{m}e_{ij} + t\,{}^{b_1}e_{ij} + t^2\,{}^{b_2}e_{ij} \quad \text{with} \;\; i\,,\, j = 1,\, 2, \tag{4.9}$$

$${}^{m}e_{ij} = \frac{1}{2}\left(\frac{\partial \mathbf{x}_m}{\partial r_i} \cdot \frac{\partial \mathbf{u}_m}{\partial r_j} + \frac{\partial \mathbf{x}_m}{\partial r_j} \cdot \frac{\partial \mathbf{u}_m}{\partial r_i} \right), \tag{4.10}$$

$${}^{b_1}e_{ij} = \frac{1}{2}\left(\frac{\partial \mathbf{x}_m}{\partial r_i} \cdot \frac{\partial \mathbf{u}_b}{\partial r_j} + \frac{\partial \mathbf{x}_m}{\partial r_j} \cdot \frac{\partial \mathbf{u}_b}{\partial r_i} + \frac{\partial \mathbf{x}_b}{\partial r_i} \cdot \frac{\partial \mathbf{u}_m}{\partial r_j} + \frac{\partial \mathbf{x}_b}{\partial r_j} \cdot \frac{\partial \mathbf{u}_m}{\partial r_i} \right), \tag{4.11}$$

$${}^{b_2}e_{ij} = \frac{1}{2}\left(\frac{\partial \mathbf{x}_b}{\partial r_i} \cdot \frac{\partial \mathbf{u}_b}{\partial r_j} + \frac{\partial \mathbf{x}_b}{\partial r_j} \cdot \frac{\partial \mathbf{u}_b}{\partial r_i} \right), \tag{4.12}$$

with

$$\mathbf{x}_m(r,s) = \sum_{i=1}^{3} h_i(r,s)\mathbf{x}_i\,,\;\; \mathbf{x}_b(r,s) = \frac{1}{2}\sum_{i=1}^{4} a_i f_i(r,s)\mathbf{V}_n^i\,, \tag{4.13}$$

$$\mathbf{u}_m(r,s) = \sum_{i=1}^{3} h_i(r,s)\mathbf{u}_i\,,\;\; \mathbf{u}_b(r,s) = \frac{1}{2}\sum_{i=1}^{4} a_i f_i(r,s)(-\alpha_i \mathbf{V}_2^i + \beta_i \mathbf{V}_1^i)\,, \tag{4.14}$$

in which ${}^{m}e_{ij}$ is the covariant membrane strain, and ${}^{b_1}e_{ij}$ and ${}^{b_2}e_{ij}$ are the covariant bending strains [60,61].

A triangular element can have up to three neighboring elements through its edges. In order to employ the strain-smoothed element (SSE) method, a target element and its three neighboring elements as shown in **Fig. 4.3**(a) are considered. In shell finite element models, the target and neighboring elements are not placed in the same plane in general. For additive operations in the strain smoothing procedure, the base coordinate systems of strains of the target and neighboring elements must be matched.

The covariant membrane strains of the target element (${}^{m}e_{ln}^{(e)}$) and of the k th neighboring element (${}^{m}e_{ln}^{(k)}$) are calculated at element centers ($r = s = 1/3$ and $t = 0$) using Eq. (4.10). The covariant membrane strain of the neighboring element is then transformed into the convected coordinates defined at the center of the target element using the following relation:

$${}^{m}\overline{e}_{ij}^{(k)} = {}^{m}e_{ln}^{(k)}({}^{(e)}\mathbf{g}_i \cdot {}^{(k)}\mathbf{g}^l)({}^{(e)}\mathbf{g}_j \cdot {}^{(k)}\mathbf{g}^n) \;\; \text{with} \;\; i, j, l, n = 1,\, 2, \tag{4.15}$$

where ${}^{(e)}\mathbf{g}_i$ and ${}^{(k)}\mathbf{g}^l$ are the covariant base vectors of the target element and the contravariant base vectors of the k th neighboring element, respectively, as seen in **Fig. 4.3**(b). In Eq. (4.15), the contravariant base vectors are calculated using the covariant base vectors in Eq. (4.6) and ${}^{(k)}\mathbf{g}_i \cdot {}^{(k)}\mathbf{g}^j = \delta_i^j$. Note that, in this strain transformation, the effect of out-of-plane strains is simply neglected.

The smoothed membrane strain between the target element and the k th neighboring element is calculated by [22]

$$ {}^m\hat{e}_{ij}^{(k)} = \frac{1}{A^{(e)} + \bar{A}^{(k)}} \left({}^m e_{ij}^{(e)} A^{(e)} + {}^m \bar{e}_{ij}^{(k)} \bar{A}^{(k)} \right) \quad \text{with} \quad i, j = 1, 2, \tag{4.16} $$

$$ \bar{A}^{(k)} = (\mathbf{n}^{(e)} \cdot \mathbf{n}^{(k)}) A^{(k)}, \quad \mathbf{n}^{(e)} = {}^{(e)}\mathbf{g}_3 / \left\| {}^{(e)}\mathbf{g}_3 \right\|, \quad \mathbf{n}^{(k)} = {}^{(k)}\mathbf{g}_3 / \left\| {}^{(k)}\mathbf{g}_3 \right\|, \tag{4.17} $$

where $A^{(e)}$ and $A^{(k)}$ are the mid-surface areas ($t = 0$) of the target and the k th neighboring elements, respectively, $\mathbf{n}^{(e)}$ and $\mathbf{n}^{(k)}$ are the unit normal vectors defined at the centers of the target and neighboring elements, respectively, and $\bar{A}^{(k)}$ is the area obtained by projecting $A^{(k)}$ into the mid-surface plane of the target element, see **Fig. 4.3**(c). Note that we use ${}^m\hat{e}_{ij}^{(k)} = {}^m e_{ij}^{(e)}$ if the k th edge of the target element is located along boundary.

Then, the membrane strains obtained through Eq. (4.16) are assigned at three Gauss points using the following equations, shown in **Fig. 4.3**(d)

$$ {}^m e_{ij}^{(A)} = \frac{1}{2}({}^m\hat{e}_{ij}^{(3)} + {}^m\hat{e}_{ij}^{(1)}), \quad {}^m e_{ij}^{(B)} = \frac{1}{2}({}^m\hat{e}_{ij}^{(1)} + {}^m\hat{e}_{ij}^{(2)}), \quad {}^m e_{ij}^{(C)} = \frac{1}{2}({}^m\hat{e}_{ij}^{(2)} + {}^m\hat{e}_{ij}^{(3)}) \tag{4.18} $$

with $i, j = 1, 2$.

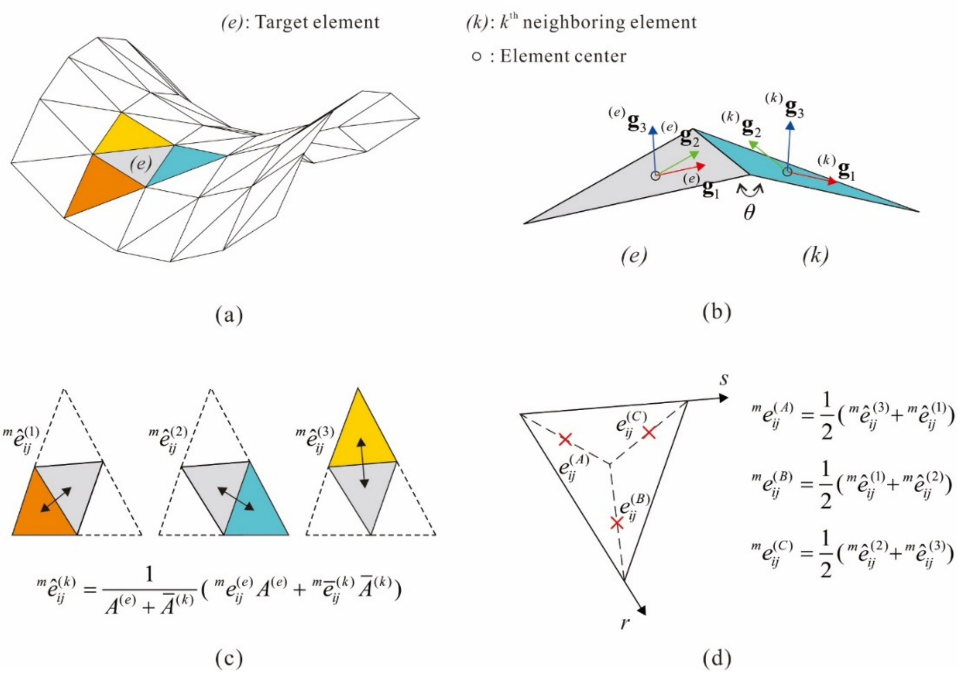

Fig. 4.3. Application of the strain-smoothed element method to the MITC3+ shell element: (a) Finite element discretization of a shell. A target element and its neighboring elements are colored. (b) Coordinate systems for strain smoothing in shell elements. (c) Strain smoothing between the target element and each neighboring element. (d) Construction of the smoothed strain field through three Gauss points.

It is very interesting that the covariant membrane strain field within the element can be explicitly expressed in a form of assumed strain

$$ {}^{m}e_{ij}^{smoothed} = \left[1 - \frac{1}{q-p}(r+s-2p) \right] {}^{m}e_{ij}^{(A)} + \frac{r-p}{q-p}\, {}^{m}e_{ij}^{(B)} + \frac{s-p}{q-p}\, {}^{m}e_{ij}^{(C)} \quad \text{with} \quad i, j = 1, 2, \tag{4.19} $$

where $p = 1/6$ and $q = 2/3$ are constants indicating the positions of the Gauss points. Note that Eq. (4.19) is not utilized in actual computation of the stiffness matrix. The assigned strains in Eq. (4.18) are used directly in the 3-point Gauss integration.

The smoothed covariant membrane strain ${}^{m}e_{ij}^{smoothed}$ in Eq. (4.19) replaces the covariant membrane strain ${}^{m}e_{ij}$ in Eq. (4.10). The originally defined ${}^{b_1}e_{ij}$ and ${}^{b_2}e_{ij}$ in Eqs. (4.11) and (4.12) are used for the covariant bending strains. For the covariant transverse shear strains, the assumed strains of the MITC3+ shell element, e_{i3}^{MITC3+} in Eqs. (4.7) and (4.8) are adopted.

In Eqs. (4.16) and (4.17), the projected element areas are used and thus the effect of membrane strain smoothing depends on the angle between the target and neighboring elements (marked with θ in **Fig. 4.3**b). As the angle approached 90 degrees, the smoothing effect gradually vanishes. This is a desirable feature.

When the angle is smaller than 90 degrees or more than two shell elements are connected through shared edges, the use of strain smoothing is not recommended. The strain smoothing is also not suitable along the boundary where material properties changes rapidly. In other words, the strain smoothing is effective, when shell geometry or material properties vary smoothly. These are also the limitations of most strain smoothing techniques.

Note that there is an alternative approach to obtain smoothed membrane strains between the target and neighboring shell elements, see Ref. [63]. It is also valuable to note that there is an interesting approach to improving stress solutions with the help of adjacent elements, see Ref. [64].

4.4. **Convergence studies**

In the following sections, we investigate the performance of the proposed strain-smoothed MITC3+ shell element using several appropriate benchmark problems: Cook's skew beam, partially clamped hyperbolic paraboloid shell, Scordelis-Lo roof shell, and clamped/free hyperboloid shell problems. The proposed element passes all the basic tests: patch, isotropy and zero energy mode tests [1]. A list of previously developed shell elements used for comparison is given in **Table 4.2** with brief descriptions.

Table 4.2. List of the shell elements used for comparison.

Element	Description
Allman	A flat shell element that combines a triangular membrane element with Allman's drilling DOFs and the discrete Kirchhoff-Mindlin triangular (DKMT) plate element. It requires 18 DOFs for an element [63,65,66].
ANDES (OPT)	A flat shell element that combines the assumed natural deviatoric strain (ANDES) triangular membrane element with 3 drilling DOFs and optimal parameters and the DKMT plate element. It has 18 DOFs for an element [63,66-68].
Shin and Lee	As a flat shell element, the edge-based strain smoothing method is applied to the ANDES formulation-based membrane element with 3 drilling DOFs, and the DKMT plate element is combined. New values of the free parameters in the ANDES formulation are introduced. It requires 18 DOFs for an element [63].
MITC3+	A continuum mechanics based 3-node shell element with a bubble node. The bubble node has 2 rotational DOFs which can be condensed out on the element level. It has 15 DOFs for an element [24,59].
Enriched MITC3+	The MITC3+ shell element enriched in membrane displacements by interpolation covers. 4 DOFs per node are added and thus the element has 27 DOFs for an element in total [58].
MITC4+	The continuum mechanics based 4-node MITC shell element with membrane locking treatment. It has 20 DOFs for an element [59,61].

For convergence studies, we use displacement or stress values at a specific location. We also use the s-norm defined by [52,55]

$$\left\|\mathbf{u}_{ref}-\mathbf{u}_{h}\right\|_{s}^{2}=\int_{\Omega}\Delta\boldsymbol{\varepsilon}^{T}\Delta\boldsymbol{\tau}\,d\Omega \quad \text{with} \quad \Delta\boldsymbol{\varepsilon}=\boldsymbol{\varepsilon}_{ref}-\boldsymbol{\varepsilon}_{h}, \quad \Delta\boldsymbol{\tau}=\boldsymbol{\tau}_{ref}-\boldsymbol{\tau}_{h}, \tag{4.20}$$

where $\mathbf{u}_{ref}$ is the reference solution, $\mathbf{u}_{h}$ is the solution of the finite element discretization, $\boldsymbol{\varepsilon}$ is the strain vector and $\boldsymbol{\tau}$ is the stress vector.

To consider various shell thicknesses, we use the relative error E_h

$$E_h = \frac{\left\| \mathbf{u}_{ref} - \mathbf{u}_h \right\|_s^2}{\left\| \mathbf{u}_{ref} \right\|_s^2}. \tag{4.21}$$

The optimal convergence behavior of the 3-node triangular shell finite elements with linear interpolation is given by

$$E_h \cong ch^2, \tag{4.22}$$

where h is the element size, and c is a constant [1].

In this study, the MITC9 shell element is used to obtain reference solutions. The MITC9 shell element satisfies the consistency and ellipticity conditions, and gives well-converged solutions [51].

4.4.1. Cook's skew beam problem

Let us consider the Cook's skew beam problem [3] shown in **Fig. 4.4**. The skew cantilever beam with unit thickness is subjected to a distributed shearing force $p = 1/16$ per unit length at its right end, and the clamped boundary condition is given at the left end. Plane stress condition is assumed, Young's modulus is $E = 1$, and Poisson's ratio is $\nu = 1/3$. We use $N \times N$ meshes with N = 2, 4, 8, 16 and 32. Two patterns of meshes (Mesh I and Mesh II) are used as shown in **Fig. 4.4**.

Normalized vertical displacements at point A are given in **Table 4.3** and **Fig. 4.5** for both mesh patterns. The s-norm convergence curves of the MITC3+ shell element, the enriched MITC3+ shell element and the strain-smoothed MITC3+ shell element for Mesh II are given in **Fig. 4.6**. The reference solutions used for s-norm are obtained using a 64×64 mesh of MITC9 shell finite elements, and the element size is $h = 1/N$. This example is purely for comparing membrane performance, and the strain-smoothed MITC3+ shell element offers very accurate solutions comparable to the enriched MITC3+ shell element.

4.4.2. Partially clamped hyperbolic paraboloid shell problem

The hyperbolic paraboloid shell problem [50] shown in **Fig. 4.7** is also considered. The mid-surface of the shell is given by

$$z = y^2 - x^2; \quad x, y \in [-1/2, 1/2]. \tag{4.23}$$

It has a uniform thickness $t = 1/1000$, and a self-weight loading $f_z = 8$ per unit area is acting on the shell.

Material properties given are $E = 2\times10^{11}$ and $\nu = 0.3$. One end of the shell is clamped, and due to its symmetry, we model only one-half of the structure with the following boundary conditions: $u_x = \beta = 0$ along *CD* and $u_x = u_y = u_z = \alpha = \beta = 0$ along *AC*. We use $N\times 2N$ meshes with N = 2, 4, 8, 16 and 24.

Table 4.4 and **Fig. 4.8** show normalized vertical displacements at point *D*. The reference solutions are obtained using a 32×64 mesh of MITC9 shell finite elements. Among the various shell elements considered, the proposed element shows the best solution accuracy.

4.4.3. Scordelis-Lo roof shell problem

The third example is the Scordelis-Lo roof shell problem [53,56] shown in **Fig. 4.9**. The shell is a part of a cylinder with length $L = 25$, radius $R = 25$, and uniform thickness t. It is subjected to a self-weight loading $f_z = 90$ per unit area. Young's modulus is $E = 4.32\times10^{8}$ and Poisson ratio is $\nu = 0$.

The shell structure is supported by rigid diaphragms at both ends. Due to symmetry, one-quarter of the structure is considered with the following boundary conditions: $u_x = u_z = 0$ along *AC*, $u_y = \alpha = 0$ along *BD* and $u_x = \beta = 0$ along *CD*. Under these conditions, a mixed bending-membrane behavior occurs in the structure. Two mesh patterns (Mesh I and Mesh II) are used, as shown in **Fig. 4.9**. The solutions are obtained with $N\times N$ element meshes (N = 4, 8, 16 and 32).

Table 4.5 gives relative errors in von-Mises stress at point *B* (for both mesh patterns with $t/L = 1/100$**),** and **Fig. 4.10** shows the von-Mises stress distributions (for Mesh I with $t/L = 1/100$). **Table 4.6** and **Fig. 4.11** show convergences in the vertical displacement at point *B* (for both mesh patterns with $t/L = 1/100$). **Fig. 4.12** shows the s-norm convergence curves of the MITC3+ shell element, the enriched MITC3+ shell element and the strain-smoothed MITC3+ shell element (for Mesh II with three different thickness to length ratios: t/L = 1/100, 1/1000 and 1/10000). The reference solutions are obtained using a 64×64 mesh of MITC9 shell finite elements. The element size is $h = 1/N$. The strain-smoothed MITC3+ shell finite element gives significantly improved solutions comparable to the enriched MITC3+ shell element.

Fig. 4.13 shows how the total number of DOFs increases when increasing the number of element layers *N*. **Table 4.7** shows the measured computation time for the MITC3+, enriched MITC3+ and smoothed MITC3+ shell elements. It includes all the time from constructing stiffness matrices to solving linear equations. We use a symmetric skyline solver, and the computations are performed using a PC with Intel Core i7-6700, 3.40GHz CPU and 64GB RAM. The strain-smoothed MITC3+ shell element requires less computation time than the enriched MITC3+ shell element, providing similarly accurate solutions.

4.4.4. Hyperboloid shell problems

We lastly consider the hyperboloid shell problems [24] shown in **Fig. 4.14**. The mid-surface geometry of the shell structure with uniform thickness *t* is given by

$$x^2 + z^2 = 1 + y^2 , \quad y \in [-1,1] . \tag{4.24}$$

The structure is subjected to a varying pressure $p(\theta) = \cos(2\theta)$. Material properties given are $E = 3\times 10^7$ and $\nu = 0.3$.

The shell structure shows different asymptotic behaviors depending on the boundary conditions. It shows a membrane-dominated behavior when both ends are clamped, and shows a bending-dominated behavior when both ends are free. Due to symmetry, only one-eighth of the shell structure is modeled. The clamped boundary condition is given as $u_x = \beta = 0$ along *BD*, $u_z = \beta = 0$ along *AC*, $u_y = \alpha = 0$ along *AB* and $u_x = u_y = u_z = \alpha = \beta = 0$ along *CD*. The free boundary condition is given as $u_x = \beta = 0$ along *BD*, $u_z = \beta = 0$ along *AC* and $u_y = \alpha = 0$ along *AB*. Finite element solutions are obtained using $N \times N$ element meshes (N = 4, 8, 16 and 32).

Fig. 4.15 and **Fig. 4.16** show the s-norm convergence curves of the MITC3+ shell element, the enriched MITC3+ shell element and the strain-smoothed MITC3+ shell element for the clamped and free boundary conditions, respectively. A 64×64 mesh of MITC9 shell finite elements is used to obtain the reference solutions. The thickness to length ratios (t/L) considered are 1/100, 1/1000 and 1/10000 with $L=1$. The element size is $h = 1/N$. In the membrane-dominated case (with the clamped boundary condition), the strain-smoothed MITC3+ shell finite element shows improved solution accuracy comparable to the enriched MITC3+ shell finite element. The three shell finite elements give good convergence behaviors in the bending-dominated case (with the free boundary condition).

Table 4.3. Normalized vertical displacements (v/v_{ref}) at point A in the Cook's skew beam problem.

	Element	DOFs per element	Mesh			
			2×2	4×4	8×8	16×16
Mesh I	Allman	18	0.8212	0.9358	0.9792	0.9939
	ANDES (OPT)	18	0.8584	0.9373	0.9782	0.9937
	Shin and Lee	18	0.7945	0.9640	0.9946	0.9992
	MITC3+	15	0.5007	0.7634	0.9195	0.9775
	Enriched MITC3+	27	0.9531	0.9871	0.9962	–
	Smoothed MITC3+	15	0.8828	1.0048	1.0057	1.0021
Mesh II	MITC3+	15	0.2815	0.4698	0.7236	0.9016
	Enriched MITC3+	27	0.8393	0.9611	0.9916	–
	Smoothed MITC3+	15	0.5154	0.8873	0.9830	0.9968
	MITC4+	20	0.7271	0.9106	0.9744	0.9933
Reference solution: $v_{ref} = 23.95$ [3]						

Table 4.4. Normalized vertical displacements (w/w_{ref}) at point D in the partially clamped hyperbolic paraboloid shell problem.

Element	DOFs per element	Mesh				
		2×4	4×8	8×16	16×32	24×48
Allman	18	0.1364	0.0656	0.2866	0.7729	0.8899
ANDES (OPT)	18	0.0067	0.0598	0.4150	0.8521	0.9111
Shin and Lee	18	1.1512	1.0093	0.9457	0.9310	0.9315
MITC3+	15	1.0552	0.9541	0.9597	0.9736	0.9823
Smoothed MITC3+	15	1.0581	0.9856	0.9858	0.9909	0.9943
Reference solution: $w_{ref} = -6.3905\times10^{-3}$						

Table 4.5. Relative errors (%) in von Mises stress obtained by $\left|\sigma_{ref}-\sigma_h\right|/\sigma_{ref}\times100$ at point B in the Scordelis-Lo roof shell problem when $t/L=1/100$.

	Element	DOFs per element	Mesh		
			8×8	16×16	32×32
Mesh I	MITC3+	15	45.56	22.52	10.66
	Smoothed MITC3+	15	24.76	13.30	6.99
Mesh II	MITC3+	15	13.94	3.51	0.96
	Smoothed MITC3+	15	0.96	1.16	0.85
Reference solution: $\sigma_{ref} = 3.0306\times10^{5}$					

Table 4.6. Normalized vertical displacements (w/w_{ref}) at point B in the Scordelis-Lo roof shell problem when $t/L = 1/100$.

	Element	DOFs per element	Mesh		
			4×4	8×8	16×16
Mesh I	Allman	18	1.0046	0.9874	–
	ANDES (OPT)	18	1.0830	1.0139	–
	Shin and Lee	18	1.0231	1.0043	–
	MITC3+	15	0.7409	0.8793	0.9618
	Enriched MITC3+	27	0.9610	0.9931	0.9983
	Smoothed MITC3+	15	1.1017	1.0323	1.0075
Mesh II	MITC3+	15	0.6744	0.8606	0.9566
	Enriched MITC3+	27	0.8922	0.9762	0.9950
	Smoothed MITC3+	15	0.9649	0.9986	0.9998
	MITC4+	20	1.0476	1.0053	0.9977
Reference solution: $w_{ref} = -0.3024$ [53,56]					

Table 4.7. Computation time (in seconds) for the Scordelis-Lo roof shell problem.

Mesh	Element	Computation time (s)		
		Constructing stiffness matrices	Solving linear equations	Total
16×16	MITC3+	0.022	0.003	0.025
	Enriched MITC3+	0.060	0.013	0.073
	Smoothed MITC3+	0.024	0.007	0.031
32×32	MITC3+	0.087	0.033	0.120
	Enriched MITC3+	0.244	0.174	0.418
	Smoothed MITC3+	0.103	0.105	0.207
64×64	MITC3+	0.369	0.449	0.818
	Enriched MITC3+	1.005	2.244	3.249
	Smoothed MITC3+	0.437	1.333	1.770

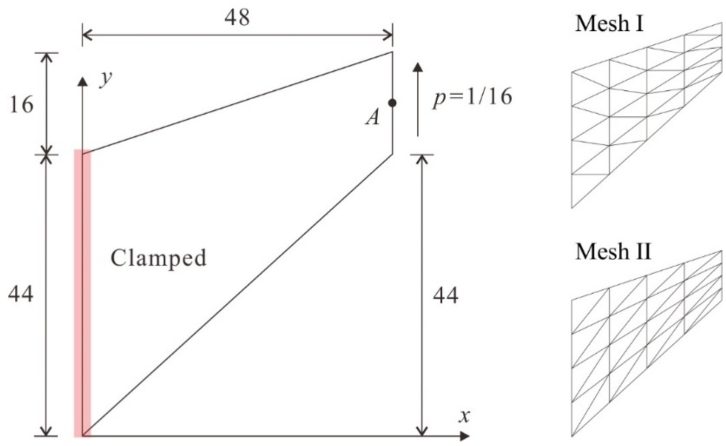

Fig. 4.4. Cook's skew beam problem and two 4×4 mesh patterns.

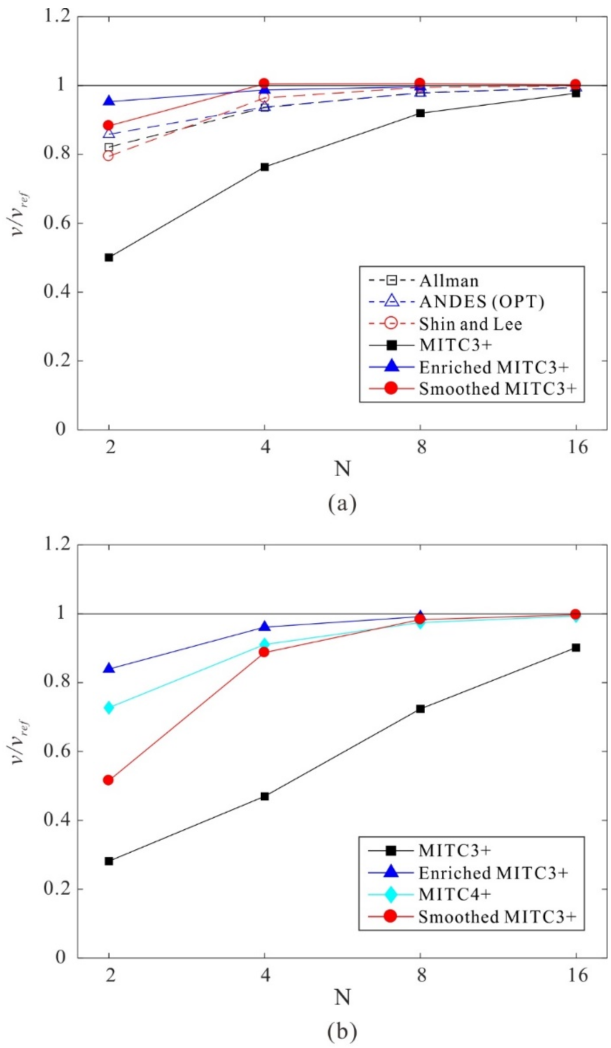

Fig. 4.5. Normalized vertical displacements at point A in the Cook's skew beam problem: (a) and (b) are the results for Mesh I and Mesh II, respectively.

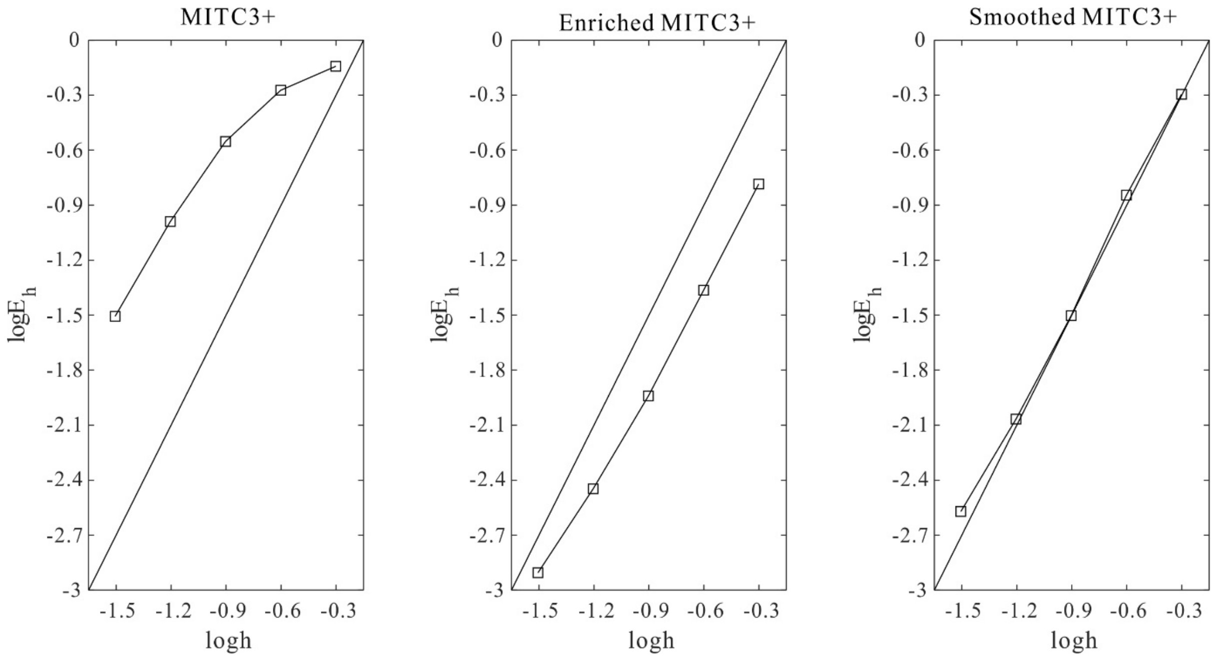

Fig. 4.6. Convergence curves for the Cook's skew beam problem when Mesh II is used. The bold line represents the optimal convergence rate.

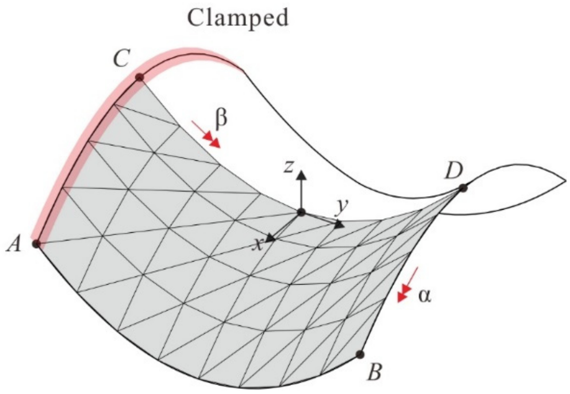

Fig. 4.7. Partially clamped hyperbolic paraboloid shell problem (4×8 mesh).

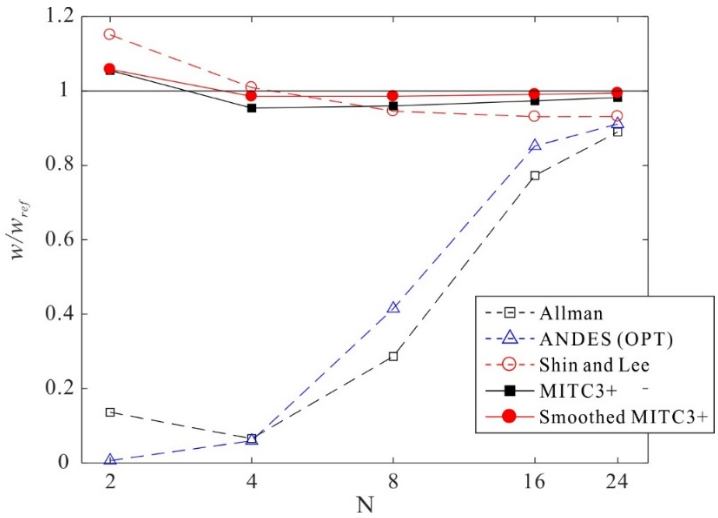

Fig. 4.8. Normalized vertical displacements at point D in the partially clamped hyperbolic paraboloid shell problem.

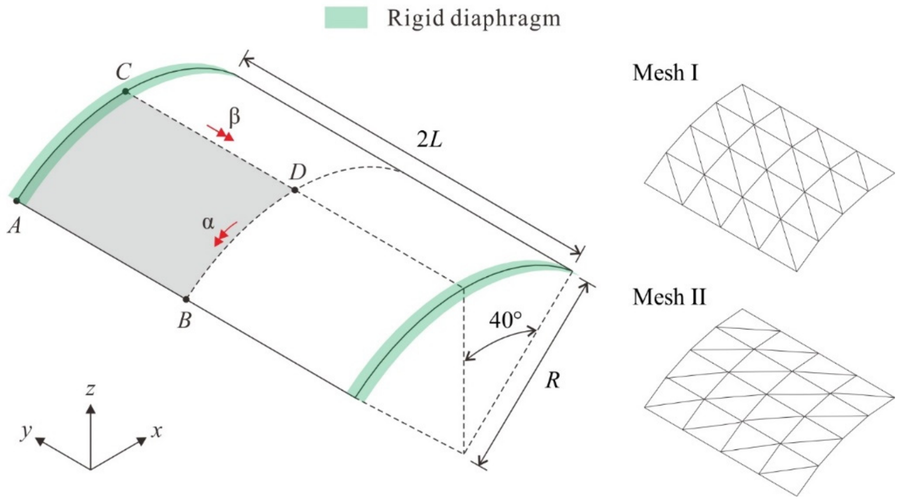

Fig. 4.9. Scordelis-Lo roof shell problem and two 4×4 mesh patterns.

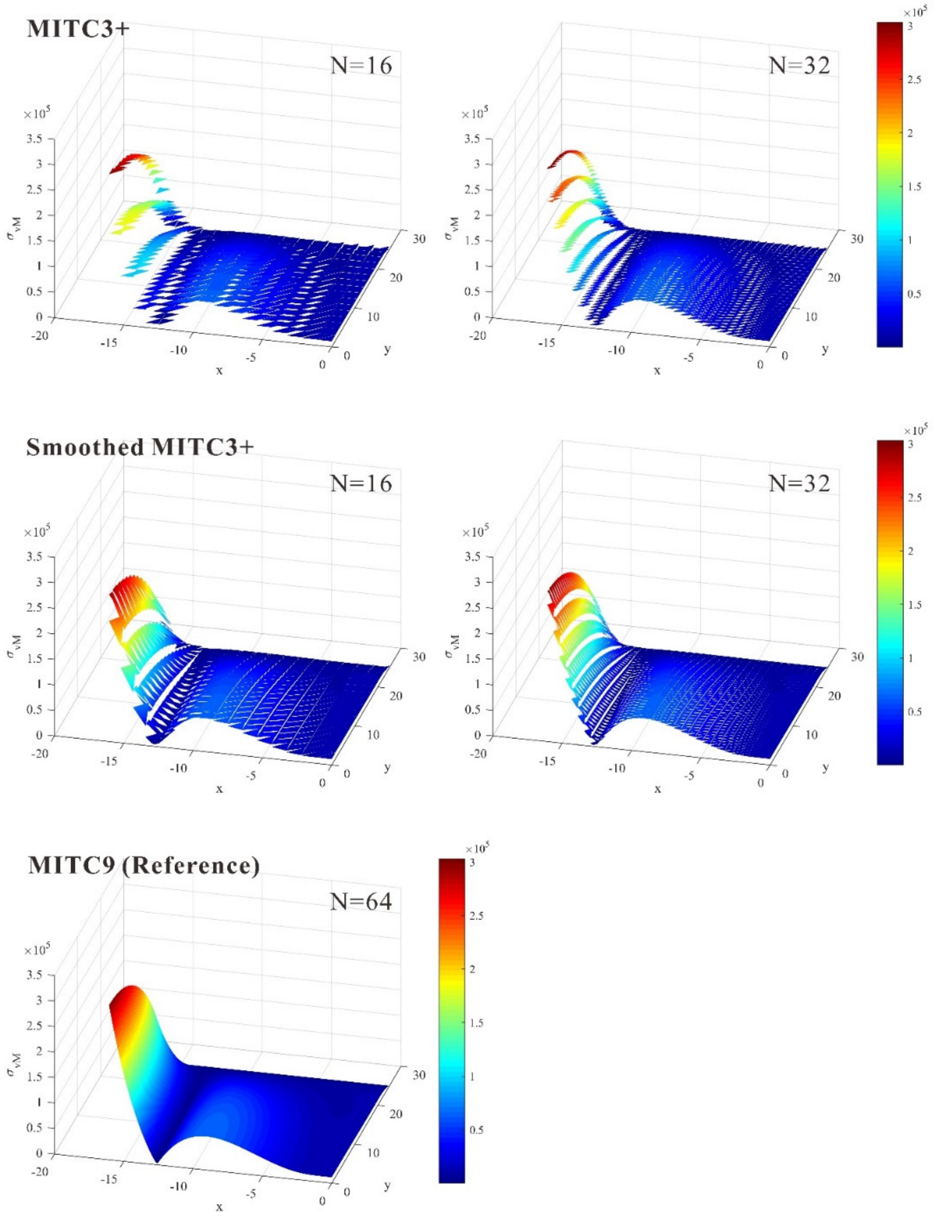

Fig. 4.10. von-Mises stress distributions for the Scordelis-Lo roof shell problem when $t/L = 1/100$ and Mesh I is used for the MITC3+ shell element and the strain-smoothed MITC3+ shell element.

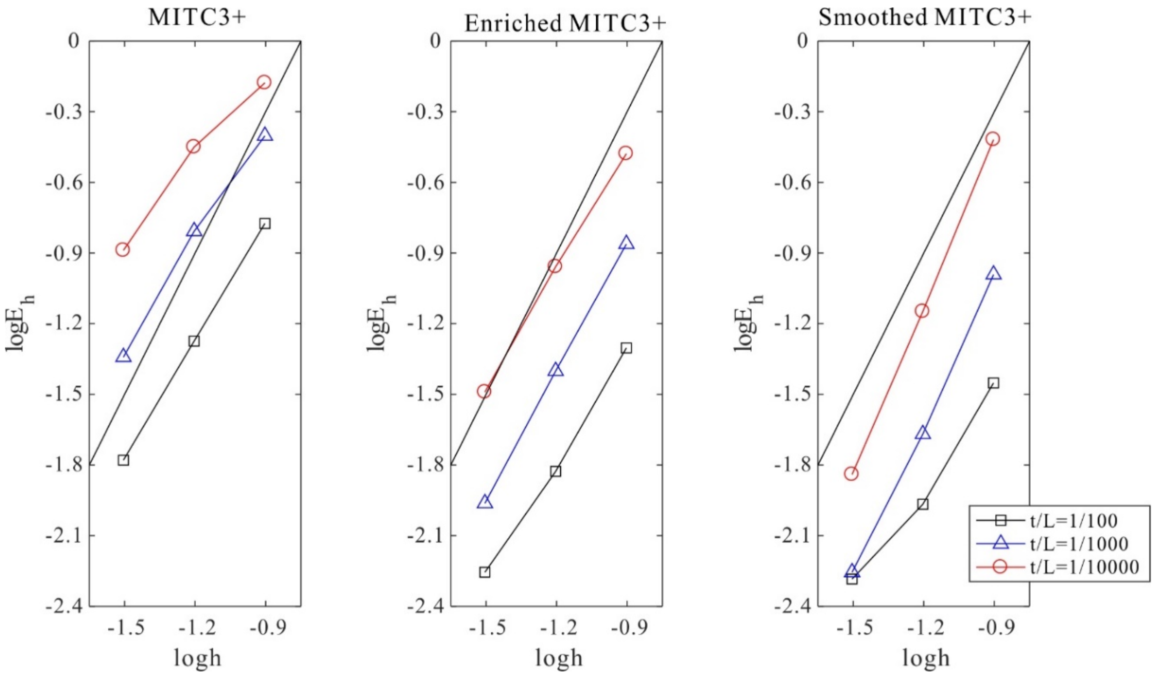

Fig. 4.11. Convergence curves for the Scordelis-Lo roof shell problem when Mesh II is used. The bold line represents the optimal convergence rate.

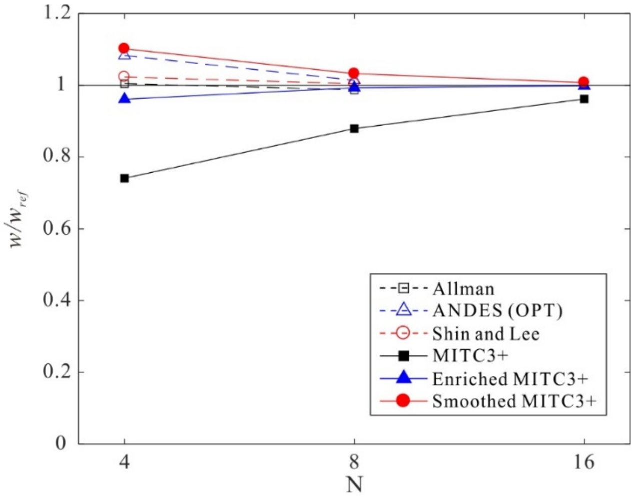

(a)

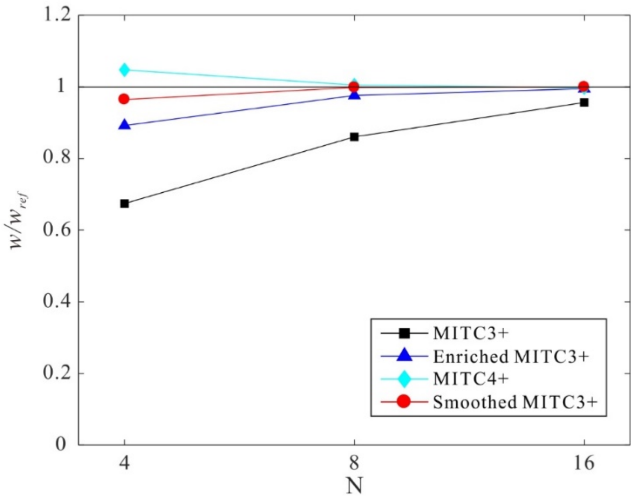

(b)

Fig. 4.12. Normalized vertical displacements at point B in the Scordelis-Lo roof shell problem when $t/L = 1/100$: (a) and (b) are the results for Mesh I and Mesh II, respectively.

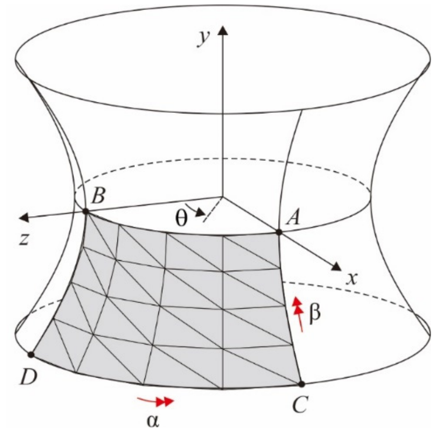

Fig. 4.13. Hyperboloid shell problem (4×4 mesh).

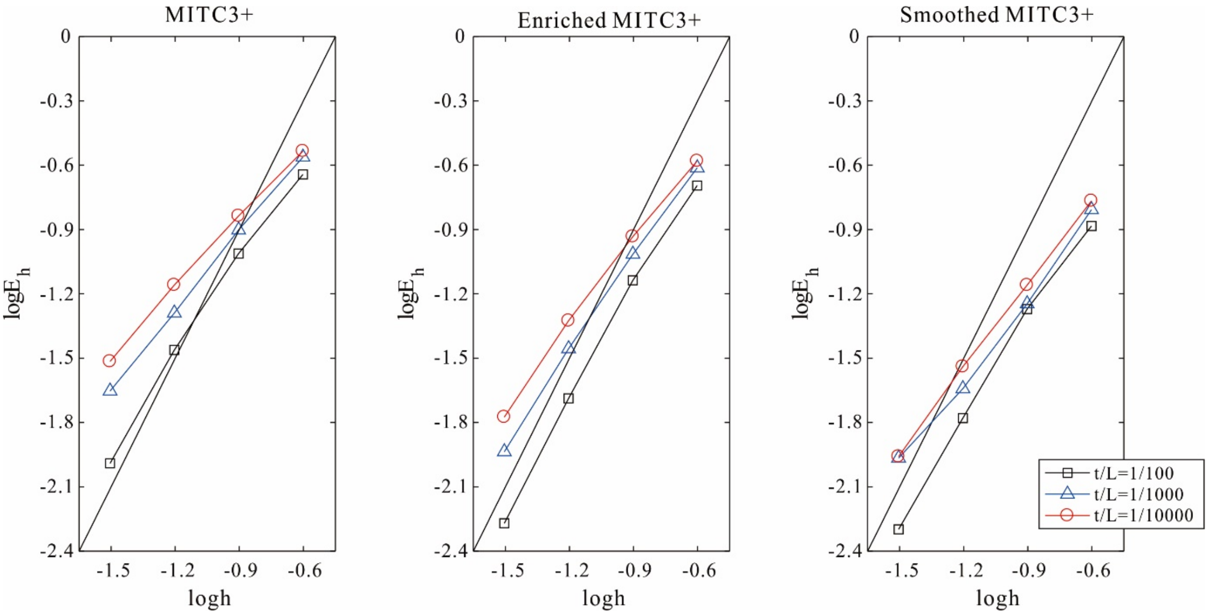

Fig. 4.14. Convergence curves for the clamped hyperboloid shell problem. The bold line represents the optimal convergence rate.

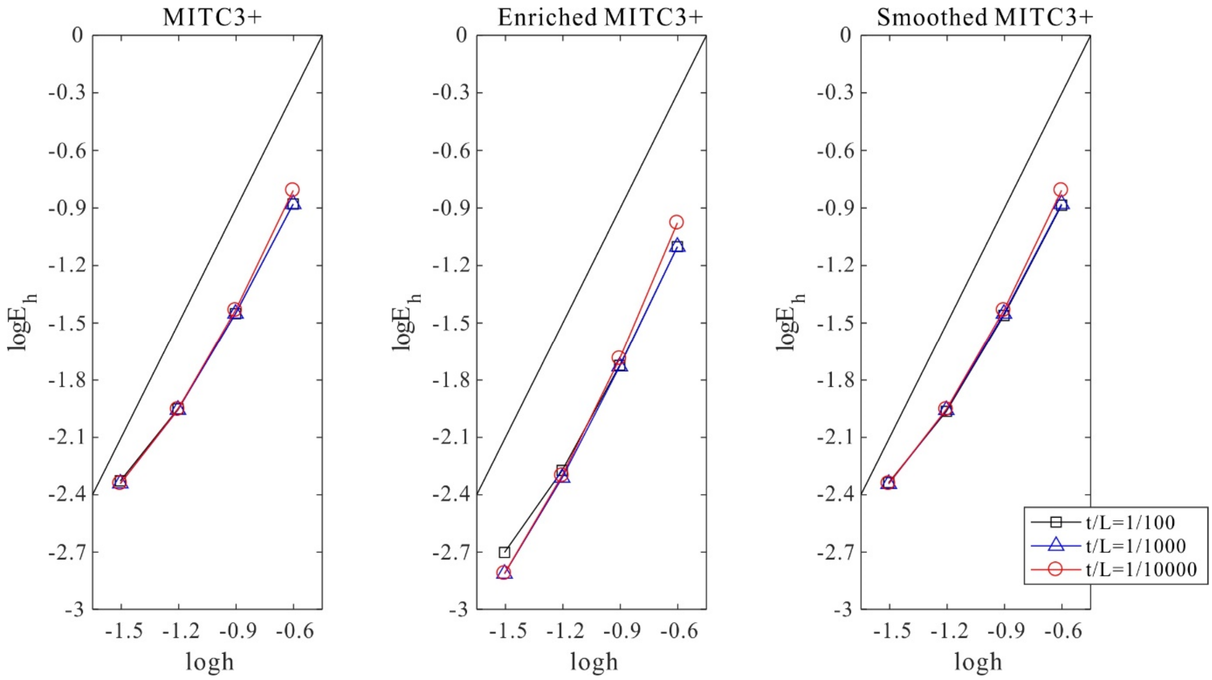

Fig. 4.15. Convergence curves for the free hyperboloid shell problem. The bold line represents the optimal convergence rate.

Chapter 5. Geometric nonlinear formulation of the strain-smoothed MITC3+ shell element

Linear and nonlinear analyses are essential for the strength evaluation of structures. In particular, nonlinear analysis is becoming more and more popular. In this chapter, the total Lagrangian formulation is employed to represent large displacements and rotations for geometric nonlinear extension of the strain-smoothed MITC3+ shell element.

The geometric nonlinear formulation of the MITC3+ shell finite element is reviewed, and then the geometric nonlinear formulation of the strain-smoothed MITC3+ shell element is presented. In the total Lagrangian formulation, the left superscript t, which usually denotes time for general analysis, represents load step for static analysis [1,57].

5.1. Formulation

5.1.1. Geometry and displacement interpolations

The geometry interpolation of the MITC3+ shell finite element in the configuration at time *t*, seen in **Fig. 5.1**, is given by [24,57]

$$ {}^{t}\mathbf{x}(r,s,\xi) = {}^{t}\mathbf{x}_m + \xi\, {}^{t}\mathbf{x}_b \quad \text{with} \quad {}^{t}\mathbf{x}_m = \sum_{i=1}^{3} h_i(r,s)\, {}^{t}\mathbf{x}_i \,, \quad {}^{t}\mathbf{x}_b = \frac{1}{2}\sum_{i=1}^{4} a_i f_i(r,s)\, {}^{t}\mathbf{V}_n^i \,, \tag{5.1} $$

where ${}^{t}\mathbf{x}_i$ is the position vector of node i in the configuration at time t, a_i is the shell thickness at node i, ${}^{t}\mathbf{V}_n^i$ is the director vector at node i in the configuration at time t, and $h_i(r,s)$ are the standard finite element shape functions and $f_i(r,s)$ are the shape functions involving the cubic bubble function f_4 corresponding to the internal node 4:

$$ h_1 = 1 - r - s \,, \quad h_2 = r \,, \quad h_3 = s \,, \tag{5.2} $$

$$ f_1 = h_1 - \frac{1}{3} f_4 \,, \quad f_2 = h_2 - \frac{1}{3} f_4 \,, \quad f_3 = h_3 - \frac{1}{3} f_4 \,, \quad f_4 = 27rs(1 - r - s) \,. \tag{5.3} $$

In Eq. (5.1), the director vector of the internal node is obtained by

$$ a_4\, {}^{t}\mathbf{V}_n^4 = \frac{1}{3}\left(a_1\, {}^{t}\mathbf{V}_n^1 + a_2\, {}^{t}\mathbf{V}_n^2 + a_3\, {}^{t}\mathbf{V}_n^3 \right). \tag{5.4} $$

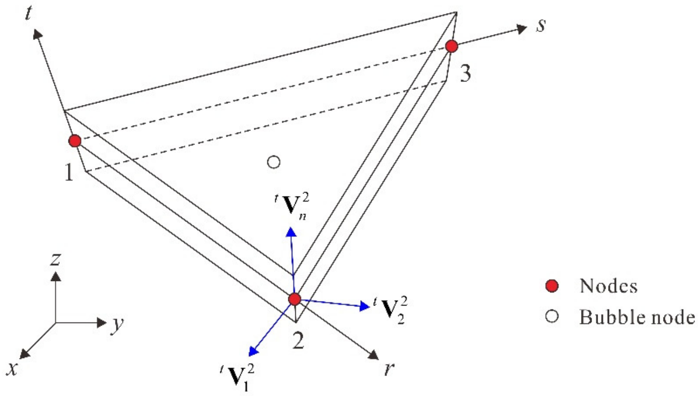

Fig. 5.1. Geometry of the MITC3+ shell finite element.

The incremental displacement vector $\mathbf{u}$ from the configuration at time t to the configuration at time $t+\Delta t$ is

$$\mathbf{u}(r,s,\xi) = {}^{t+\Delta t}\mathbf{x}(r,s,\xi) - {}^{t}\mathbf{x}(r,s,\xi)\,, \tag{5.5}$$

and thus

$$\mathbf{u}(r,s,\xi) = \sum_{i=1}^{3} h_i(r,s)\mathbf{u}_i + \frac{\xi}{2}\sum_{i=1}^{4} a_i f_i(r,s)\left({}^{t+\Delta t}\mathbf{V}_n^i - {}^{t}\mathbf{V}_n^i\right), \tag{5.6}$$

in which $\mathbf{u}_i$ is the vector of incremental nodal displacements at node i.

The difference between two director vectors in successive times in Eq. (5.6) is defined as follows by considering up to quadratic order [57]

$${}^{t+\Delta t}\mathbf{V}_n^i - {}^{t}\mathbf{V}_n^i = \boldsymbol{\theta}_i \times {}^{t}\mathbf{V}_n^i + \frac{1}{2}\boldsymbol{\theta}_i \times (\boldsymbol{\theta}_i \times {}^{t}\mathbf{V}_n^i) \quad \text{with} \quad \boldsymbol{\theta}_i = \alpha_i\,{}^{t}\mathbf{V}_1^i + \beta_i\,{}^{t}\mathbf{V}_2^i\,, \tag{5.7}$$

and it can be rewritten as

$${}^{t+\Delta t}\mathbf{V}_n^i - {}^{t}\mathbf{V}_n^i = -\alpha_i\,{}^{t}\mathbf{V}_2^i + \beta_i\,{}^{t}\mathbf{V}_1^i - \frac{1}{2}(\alpha_i^2 + \beta_i^2)\,{}^{t}\mathbf{V}_n^i\,, \tag{5.8}$$

where ${}^{t}\mathbf{V}_1^i$ and ${}^{t}\mathbf{V}_2^i$ are the unit vectors orthogonal to ${}^{t}\mathbf{V}_n^i$ and to each other, and α_i and β_i are the incremental rotations of the director vector ${}^{t}\mathbf{V}_n^i$ about ${}^{t}\mathbf{V}_1^i$ and ${}^{t}\mathbf{V}_2^i$, respectively, at node i.

Substituting Eq. (5.8) into Eq. (5.6), the incremental displacement vector can be expressed as

$$\mathbf{u}(r,s,\xi) = \mathbf{u}_m + \xi(\mathbf{u}_{b1} + \mathbf{u}_{b2})\,, \tag{5.9a}$$

with

$$\mathbf{u}_m = \sum_{i=1}^{3} h_i(r,s)\mathbf{u}_i \,, \tag{5.9b}$$

$$\mathbf{u}_{b1} = \frac{1}{2}\sum_{i=1}^{4} a_i f_i(r,s)\left(-\alpha_i\, {}^t\mathbf{V}_2^i + \beta_i\, {}^t\mathbf{V}_1^i\right), \tag{5.9c}$$

$$\mathbf{u}_{b2} = -\frac{1}{4}\sum_{i=1}^{4} a_i f_i(r,s)\left[\left(\alpha_i^2 + \beta_i^2\right){}^t\mathbf{V}_n^i\right]. \tag{5.9d}$$

The incremental displacement vector in Eq. (5.9a) could be grouped as

$$\mathbf{u}_l = \mathbf{u}_m + \xi\mathbf{u}_{b1}\,, \quad \mathbf{u}_q = \xi\mathbf{u}_{b2}\,, \tag{5.10}$$

in which $\mathbf{u}_l$ and $\mathbf{u}_q$ are the linear and quadratic parts of the incremental displacement vector $\mathbf{u}$, respectively.

5.1.2. Green-Lagrange strain

The covariant base vectors at time t is given by

$${}^t\mathbf{g}_i = \frac{\partial\, {}^t\mathbf{x}}{\partial r_i} \quad \text{with} \quad r_1 = r\,, \quad r_2 = s\,, \quad r_3 = \xi\,, \tag{5.11}$$

and the covariant base vectors at time t and time 0 has the following relation:

$${}^t\mathbf{g}_i = {}^0\mathbf{g}_i + {}^t\mathbf{u}_{,i} \quad \text{with} \quad {}^t\mathbf{u}_{,i} = \frac{\partial\, {}^t\mathbf{u}}{\partial r_i}\,, \quad {}^t\mathbf{u} = {}^t\mathbf{x} - {}^0\mathbf{x}\,. \tag{5.12}$$

The covariant Green-Lagrange strain components in the configuration at time t with respect to the reference configuration at time 0 are given by

$${}_0^t\varepsilon_{ij} = \frac{1}{2}\left({}^t\mathbf{g}_i \cdot {}^t\mathbf{g}_j - {}^0\mathbf{g}_i \cdot {}^0\mathbf{g}_j\right) \quad \text{with} \quad i\,,\, j = 1, 2, 3, \tag{5.13}$$

and its in-plane strain components (i, j = 1, 2) are expressed as [62]

$${}_0^t\varepsilon_{ij} = {}_0^t\varepsilon_{ij}^m + \xi\, {}_0^t\varepsilon_{ij}^{b1} + \xi^2\, {}_0^t\varepsilon_{ij}^{b2} \quad \text{with} \quad i\,,\, j = 1, 2, \tag{5.14a}$$

in which

$${}_0^t\varepsilon_{ij}^m = \frac{1}{2}\left({}^t\mathbf{x}_{m,i} \cdot {}^t\mathbf{x}_{m,j} - {}^0\mathbf{x}_{m,i} \cdot {}^0\mathbf{x}_{m,j}\right), \tag{5.14b}$$

$${}_0^t\varepsilon_{ij}^{b1} = \frac{1}{2}\left[\left({}^t\mathbf{x}_{m,i} \cdot {}^t\mathbf{x}_{b,j} + {}^t\mathbf{x}_{m,j} \cdot {}^t\mathbf{x}_{b,i}\right) - \left({}^0\mathbf{x}_{m,i} \cdot {}^0\mathbf{x}_{b,j} + {}^0\mathbf{x}_{m,j} \cdot {}^0\mathbf{x}_{b,i}\right)\right], \tag{5.14c}$$

$${}_0^t\varepsilon_{ij}^{b2} = \frac{1}{2}\left({}^t\mathbf{x}_{b,i} \cdot {}^t\mathbf{x}_{b,j} - {}^0\mathbf{x}_{b,i} \cdot {}^0\mathbf{x}_{b,j}\right) \quad \text{with} \quad {}^t\mathbf{x}_{m,i} = \frac{\partial\, {}^t\mathbf{x}_m}{\partial r_i}\,, \quad {}^t\mathbf{x}_{b,i} = \frac{\partial\, {}^t\mathbf{x}_b}{\partial r_i}\,. \tag{5.14d}$$

The incremental covariant Green-Lagrange strain components are defined by

$${}_0\varepsilon_{ij} = {}^{t+\Delta t}_{\ 0}\varepsilon_{ij} - {}^{t}_{0}\varepsilon_{ij} = \frac{1}{2}(\mathbf{u}_{,i} \cdot {}^t\mathbf{g}_j + {}^t\mathbf{g}_i \cdot \mathbf{u}_{,j} + \mathbf{u}_{,i} \cdot \mathbf{u}_{,j}) \quad \text{with} \quad \mathbf{u}_{,i} = \frac{\partial \mathbf{u}}{\partial r_i}. \tag{5.15}$$

By retaining the strain terms up to the second order of unknowns, the incremental covariant strain components are approximated as

$${}_0\varepsilon_{ij} = {}_0e_{ij} + {}_0\eta_{ij} \quad \text{with} \quad i\,,\, j = 1, 2, 3, \tag{5.16a}$$

and

$${}_0e_{ij} = \frac{1}{2}(\frac{\partial \mathbf{u}_l}{\partial r_i} {}^t\mathbf{g}_j + {}^t\mathbf{g}_i \frac{\partial \mathbf{u}_l}{\partial r_j}), \tag{5.16b}$$

$${}_0\eta_{ij} = \frac{1}{2}\left(\frac{\partial \mathbf{u}_l}{\partial r_i} \cdot \frac{\partial \mathbf{u}_l}{\partial r_j}\right) + \frac{1}{2}\left(\frac{\partial \mathbf{u}_q}{\partial r_i} {}^t\mathbf{g}_j + {}^t\mathbf{g}_i \frac{\partial \mathbf{u}_q}{\partial r_j}\right), \tag{5.16c}$$

in which ${}_0e_{ij}$ and ${}_0\eta_{ij}$ are the linear and nonlinear parts of the incremental strain, respectively [57].

The in-plane components (i , j = 1, 2) of the incremental covariant strain in Eq. (5.16a) can be decomposed as follows. For the linear part,

$${}_0e_{ij} = {}_0e_{ij}^{m} + \xi\, {}_0e_{ij}^{b1} + \xi^2\, {}_0e_{ij}^{b2} \quad \text{with} \quad i\,,\, j = 1, 2, \tag{5.17a}$$

with

$${}_0e_{ij}^{m} = \frac{1}{2}\left({}^t\mathbf{x}_{m,i} \cdot \mathbf{u}_{m,j} + {}^t\mathbf{x}_{m,j} \cdot \mathbf{u}_{m,i} \right), \tag{5.17b}$$

$${}_0e_{ij}^{b1} = \frac{1}{2}\left({}^t\mathbf{x}_{m,i} \cdot \mathbf{u}_{b1,j} + {}^t\mathbf{x}_{m,j} \cdot \mathbf{u}_{b1,i} + {}^t\mathbf{x}_{b,i} \cdot \mathbf{u}_{m,j} + {}^t\mathbf{x}_{b,j} \cdot \mathbf{u}_{m,i} \right), \tag{5.17c}$$

$${}_0e_{ij}^{b2} = \frac{1}{2}\left({}^t\mathbf{x}_{b,i} \cdot \mathbf{u}_{b1,j} + {}^t\mathbf{x}_{b,j} \cdot \mathbf{u}_{b1,i} \right), \tag{5.17d}$$

and, for the nonlinear part,

$${}_0\eta_{ij} = {}_0\eta_{ij}^{m} + \xi\, {}_0\eta_{ij}^{b1} + \xi^2\, {}_0\eta_{ij}^{b2} \quad \text{with} \quad i\,,\, j = 1, 2, \tag{5.18a}$$

with

$${}_0\eta_{ij}^{m} = \frac{1}{2}\mathbf{u}_{m,i} \cdot \mathbf{u}_{m,j}, \tag{5.18b}$$

$${}_0\eta_{ij}^{b1} = \frac{1}{2}\left(\mathbf{u}_{m,i} \cdot \mathbf{u}_{b1,j} + \mathbf{u}_{m,j} \cdot \mathbf{u}_{b1,i} + {}^t\mathbf{x}_{m,i} \cdot \mathbf{u}_{b2,j} + {}^t\mathbf{x}_{m,j} \cdot \mathbf{u}_{b2,i} \right), \tag{5.18c}$$

$${}_0\eta_{ij}^{b2} = \frac{1}{2}\left(\mathbf{u}_{b1,i} \cdot \mathbf{u}_{b1,j} + {}^t\mathbf{x}_{b,i} \cdot \mathbf{u}_{b2,j} + {}^t\mathbf{x}_{b,j} \cdot \mathbf{u}_{b2,i} \right). \tag{5.18d}$$

The in-plane components (i , j = 1, 2) of the incremental covariant Green-Lagrange strain in Eqs. (5.17a)-(5.18d) can be grouped as

$$ {}_0\varepsilon_{ij} = {}_0\varepsilon_{ij}^{m} + \xi\, {}_0\varepsilon_{ij}^{b1} + \xi^2\, {}_0\varepsilon_{ij}^{b2} \tag{5.19a} $$

and

$$ {}_0\varepsilon_{ij}^{m} = {}_0e_{ij}^{m} + {}_0\eta_{ij}^{m} , \tag{5.19b} $$

$$ {}_0\varepsilon_{ij}^{b1} = {}_0e_{ij}^{b1} + {}_0\eta_{ij}^{b1} , \tag{5.19c} $$

$$ {}_0\varepsilon_{ij}^{b2} = {}_0e_{ij}^{b2} + {}_0\eta_{ij}^{b2} . \tag{5.19d} $$

where ${}_0\varepsilon_{ij}^{m}$ denotes the incremental covariant membrane strain, and ${}_0\varepsilon_{ij}^{b1}$ and ${}_0\varepsilon_{ij}^{b2}$ denote the incremental covariant bending strains.

5.1.3. Assumed transverse shear strain

The assumed transverse shear strain fields of the MITC3+ shell element are employed to alleviate shear locking [24,57]. The transverse shear strain components in Eq. (5.16a) are substituted by

$$ {}_0\varepsilon_{i3}^{MITC3+} = {}_0e_{i3}^{MITC3+} + {}_0\eta_{i3}^{MITC3+} \quad \text{with } i , j = 1, 2, \tag{5.20a} $$

and

$$ {}_0\varepsilon_{13}^{MITC3+} = \frac{2}{3}\left({}_0\varepsilon_{13}^{B} - \frac{1}{2}\, {}_0\varepsilon_{23}^{B} \right) + \frac{1}{3}\left({}_0\varepsilon_{13}^{A} + {}_0\varepsilon_{23}^{A} \right) + \frac{1}{3}\, {}_0\hat{c}(3s-1) , \tag{5.20b} $$

$$ {}_0\varepsilon_{23}^{MITC3+} = \frac{2}{3}\left({}_0\varepsilon_{23}^{C} - \frac{1}{2}\, {}_0\varepsilon_{13}^{C} \right) + \frac{1}{3}\left({}_0\varepsilon_{13}^{A} + {}_0\varepsilon_{23}^{A} \right) + \frac{1}{3}\, {}_0\hat{c}(1-3r) , \tag{5.20c} $$

where ${}_0\hat{c} = {}_0\varepsilon_{13}^{F} - {}_0\varepsilon_{13}^{D} - {}_0\varepsilon_{23}^{F} + {}_0\varepsilon_{23}^{E}$ and the tying points *(A)-(F)* are given in **Fig. 5.2** and **Table 5.1**.

For the MITC3+ shell element, the two rotational DOFs of the internal node can be statically condensed out in the element level [24]. We use the 3-point Gauss integration in the $r-s$ plane and the 2-point Gauss integration in the ξ -direction to evaluate the stiffness matrix and internal force vector.

Table 5.1. Tying points for the assumed transverse shear strain fields of the MITC3+ shell finite element, seen in Fig. 5.2.

Tying points	r	s
(A)	1/6	1/6
(B)	2/3	1/6
(C)	1/6	2/3
(D)	1/3 + 1/10000	1/3 – 1/5000
(E)	1/3 - 1/5000	1/3 + 1/10000
(F)	1/3 + 1/10000	1/3 + 1/10000

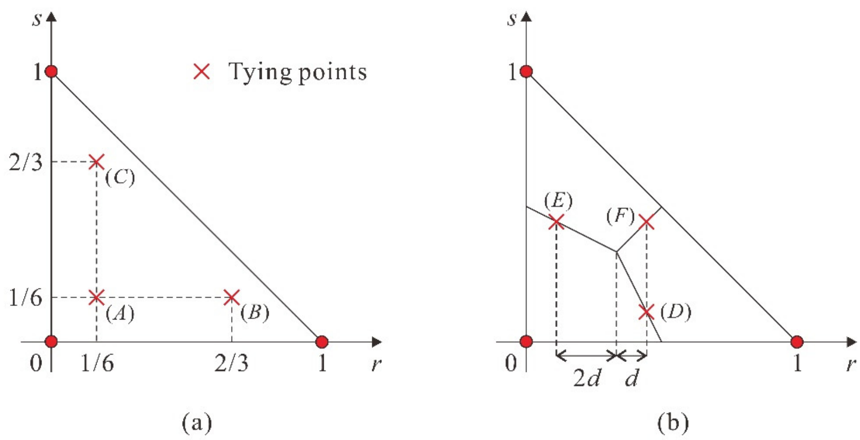

Fig. 5.2. Tying points for the assumed transverse shear strain fields of the MITC3+ shell finite element. The points (A)-(C) are also Gauss integration points.

5.1.4. Smoothed membrane strain

For triangular elements, there can be up to three adjacent elements through its edges. The strains of all adjacent elements are fully used for the SSE method [22,23,25]. **Fig. 5.3** depicts a target element e and its three adjacent elements k ($k = 1, 2, 3$). Considering that the shell elements do not lie on the same plane in general, we match the base coordinate systems of strains of the target and neighboring elements before strain smoothing.

The incremental covariant membrane strains of the target element ${}_0\varepsilon_{ln}^{m,(e)}$ and of the k th adjacent element ${}_0\varepsilon_{ln}^{m,(k)}$ at element centers ($r = s = 1/3$ and $\xi = 0$) are obtained using Eq. (5.19b). Then, we transform the strains of the adjacent elements into the convected coordinates of the target element as follows

$$ {}_0\bar{\varepsilon}_{ij}^{m,(k)} = {}_0\varepsilon_{ln}^{m,(k)} ({}^{(e)}\mathbf{g}_i \cdot {}^{(k)}\mathbf{g}^l)({}^{(e)}\mathbf{g}_j \cdot {}^{(k)}\mathbf{g}^n) \quad \text{with} \quad i,j,l,n = 1, 2, \tag{5.21} $$

where ${}^{(e)}\mathbf{g}_i$ and ${}^{(k)}\mathbf{g}^l$ are the covariant base vectors of the target element and the contravariant base vectors of the k th adjacent element, respectively, in the configuration at time t, as shown in **Fig. 5.4**. The contravariant base vectors are obtained using the covariant base vectors and the relation ${}^{(k)}\mathbf{g}_i \cdot {}^{(k)}\mathbf{g}^j = \delta_i^j$. Note that we neglect the influence of out-of-plane strains in the transformation [25].

Then, we calculate the smoothed incremental membrane strains ($i, j = 1, 2$) between the target element e and the adjacent elements k ($k = 1, 2, 3$) as follows

$$ {}_0\hat{\varepsilon}_{ij}^{m,(k)} = \frac{1}{A^{(e)} + \bar{A}^{(k)}} ({}_0\varepsilon_{ij}^{m,(e)} A^{(e)} + {}_0\bar{\varepsilon}_{ij}^{m,(k)} \bar{A}^{(k)}) \quad \text{with} \quad \bar{A}^{(k)} = (\mathbf{n}^{(e)} \cdot \mathbf{n}^{(k)}) A^{(k)} \tag{5.22} $$

where $\mathbf{n}^{(e)} = {}^{(e)}\mathbf{g}_3 / \|{}^{(e)}\mathbf{g}_3\|$ and $\mathbf{n}^{(k)} = {}^{(k)}\mathbf{g}_3 / \|{}^{(k)}\mathbf{g}_3\|$ are the unit normal vectors of the target and the k th adjacent elements calculated at element centers, respectively, $A^{(e)}$ and $A^{(k)}$ are the mid-surface areas ($\xi = 0$) of the target and the k th adjacent elements, respectively, and $\bar{A}^{(k)}$ is the area obtained by projecting $A^{(k)}$ onto the mid-surface plane of the target element, as shown in **Fig. 5.5**(a). Note that, if there is no adjacent element to the k th edge of the target element, we use ${}_0\hat{\varepsilon}_{ij}^{m,(k)} = {}_0\varepsilon_{ij}^{m,(e)}$ instead.

Then, the smoothed incremental membrane strains in Eq. (5.22) are assigned at three Gauss integration points as follows, as shown in **Fig. 5.5**(b),

$$ \begin{aligned} &{}_0\varepsilon_{ij}^{m,(A)} = \frac{1}{2}({}_0\hat{\varepsilon}_{ij}^{m,(3)} + {}_0\hat{\varepsilon}_{ij}^{m,(1)}), \quad {}_0\varepsilon_{ij}^{m,(B)} = \frac{1}{2}({}_0\hat{\varepsilon}_{ij}^{m,(1)} + {}_0\hat{\varepsilon}_{ij}^{m,(2)}), \\ &{}_0\varepsilon_{ij}^{m,(C)} = \frac{1}{2}({}_0\hat{\varepsilon}_{ij}^{m,(2)} + {}_0\hat{\varepsilon}_{ij}^{m,(3)}) \quad \text{with} \quad i, j = 1, 2. \end{aligned} \tag{5.23} $$

Note that the smoothed strains in Eq. (5.23) are used directly at the Gauss integration points to compute the tangent stiffness matrix and internal force vector.

The incremental covariant membrane strain in Eq. (5.19b) is substituted by the smoothed membrane strain in Eq. (23) obtained using the SSE method. The incremental covariant transverse shear strain in Eq. (16a) is replaced with the assumed transverse shear strain in Eq. (5.20a) obtained using the MITC method.

Due to the strain transformation in Eq. (5.21) and area projection in Eq. (5.22), the effect of strain smoothing is affected by the angle between the target and adjacent elements (θ in **Fig. 5.5**a). The smoothing effect is designed to gradually vanish as the angle approaches 90 degrees.

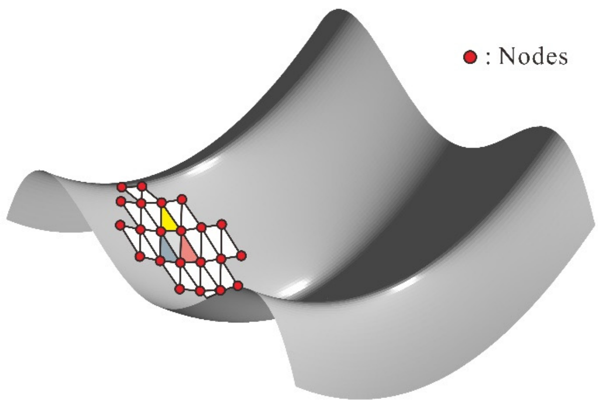

Fig. 5.3. Finite element discretization of a shell structure. A target element and its neighboring elements are colored.

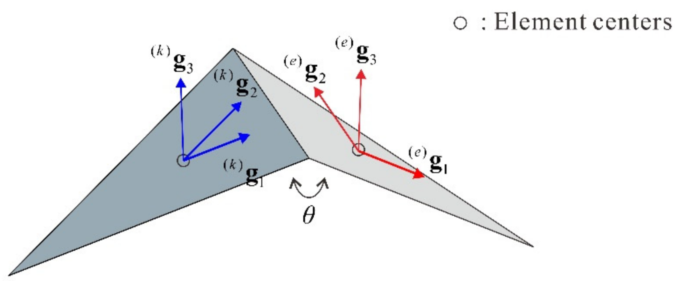

Fig. 5.4. Coordinate systems for strain smoothing in shell elements.

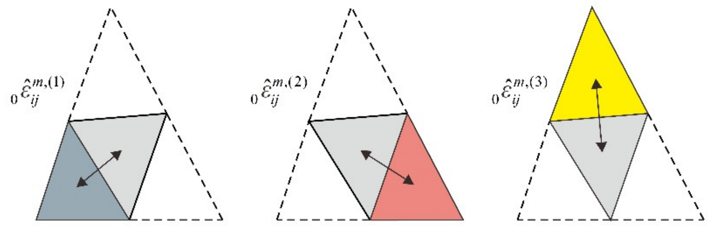

$$ {}_0\hat{\varepsilon}_{ij}^{m,(k)} = \frac{1}{A^{(e)} + \bar{A}^{(k)}} \left({}_0\varepsilon_{ij}^{m,(e)} A^{(e)} + {}_0\bar{\varepsilon}_{ij}^{m,(k)} \bar{A}^{(k)} \right) $$

(a)

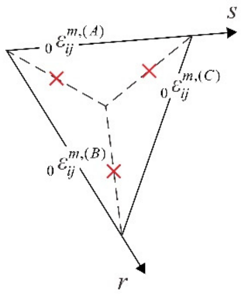

$$ {}_0\varepsilon_{ij}^{m,(A)} = \frac{1}{2} \left({}_0\hat{\varepsilon}_{ij}^{m,(3)} + {}_0\hat{\varepsilon}_{ij}^{m,(1)} \right) $$

$$ {}_0\varepsilon_{ij}^{m,(B)} = \frac{1}{2} \left({}_0\hat{\varepsilon}_{ij}^{m,(1)} + {}_0\hat{\varepsilon}_{ij}^{m,(2)} \right) $$

$$ {}_0\varepsilon_{ij}^{m,(C)} = \frac{1}{2} \left({}_0\hat{\varepsilon}_{ij}^{m,(2)} + {}_0\hat{\varepsilon}_{ij}^{m,(3)} \right) $$

(b)

Fig. 5.5. Strain smoothing in shell elements: (a) Strain smoothing between the target element and each neighboring element. (b) Strain smoothing within elements and construction of the smoothed strain field through three Gauss points.

5.2. **Numerical examples**

In this section, we evaluate the performance of the strain-smoothed MITC3+ shell element using several proper numerical examples in geometric nonlinear range. The Newton-Raphson method is used to solve the nonlinear equations in every load step with a convergence tolerance of 0.1 percent of the relative incremental energy [1].

Through our previous work in geometric linear range, we verified that the strain-smoothed MITC3+ shell element has superior performance compared with other competitive elements [25]. In this study, we demonstrate that the strain-smoothed element originally proposed for linear analysis also exhibits high performance in nonlinear analysis. The results of the linear analysis are also introduced briefly in the first problem.

The performance of the proposed strain-smoothed MITC3+ shell element (15 element DOFs) is compared with those of the MITC3+ shell element (15 element DOFs) and the enriched MITC3+ shell element (27 element DOFs). The MITC3+ shell element shows excellent bending behaviors by alleviating the locking [24,57], but shows insufficient membrane behaviors. The enriched MITC3+ shell element shows successful membrane performance by enriching the membrane displacement field with interpolation covers, but it requires 12 additional DOFs for an element [58].

For comparison purposes, displacements at specific locations, von Mises distributions and deformed configurations are measured at several load steps for various mesh patterns. We also use the s-norm defined below for the study in geometric linear range [52,55]

$$\left\|\mathbf{u}_{ref}-\mathbf{u}_h\right\|_s^2=\int_{\Omega}(\boldsymbol{\varepsilon}_{ref}-\boldsymbol{\varepsilon}_h)^T(\boldsymbol{\tau}_{ref}-\boldsymbol{\tau}_h)d\Omega\,, \tag{5.24}$$

and its relative error is given by

$$E_h=\frac{\left\|\mathbf{u}_{ref}-\mathbf{u}_h\right\|_s^2}{\left\|\mathbf{u}_{ref}\right\|_s^2}\,, \tag{5.25}$$

where $\mathbf{u}_{ref}$ is the reference solution, $\mathbf{u}_h$ is the solution of the finite element discretization, $\boldsymbol{\varepsilon}$ is the strain vector and $\boldsymbol{\tau}$ is the stress vector.

The reference solutions are obtained using the MITC9 shell element, which satisfies the consistency and ellipticity conditions and gives well-converged solutions in both linear and nonlinear analyses [51].

5.2.1. Scordelis-Lo roof

We consider the Scordelis-Lo roof shell problem [53,58] shown in **Fig. 5.6**. The shell is an arc of length $L=25$, radius $R=25$, and uniform thickness t. It is subjected to a self-weight loading f. Young's modulus is $E=4.32\times10^8$ and Poisson's ratio is $\nu=0$. Both ends of the structure are supported by rigid diaphragms, and due to the symmetry of the problem, we only consider one-quarter of the model. Detailed boundary conditions are as follows: $u=w=0$ along BD, $v=\alpha=0$ along AC and $u=\beta=0$ along AB. In this problem, the shell shows a mixed bending-membrane behavior.

The geometric linear analysis is performed first with a loading $f=90$ per unit area. The solutions are obtained with $N\times N$ element meshes (N = 8, 16 and 32) for three different thickness to length ratios (t/L = 1/100, 1/1000 and 1/10000). The s-norm convergence curves of the MITC3+, enriched MITC3+ and smoothed MITC3+ shell elements are depicted in **Fig. 5.7**. The reference solutions are obtained using a 64×64 mesh of MITC9 shell finite elements. The element size is $h=1/N$. The strain-smoothed MITC3+ shell element (15 element DOFs) provides very accurate solutions, which is even better than those of the enriched MITC3+ shell element (27 element DOFs) [25].

Then, the computational efficiency of the considered elements are compared for the case when t/L = 1/1000. **Fig. 5.8** shows the relations between computation times versus solution accuracies (relative errors in the s-norm). The computation times involve all the time from constructing stiffness matrices to solving linear equations. We use a symmetric skyline solver, and the computations are performed using a PC with Intel Core i7-6700, 3.40GHz CPU and 64GB RAM. The strain-smoothed MITC3+ shell element gives the best computational efficiency among the elements considered.

Now, we perform the geometric nonlinear analysis with an increased loading $f_{max} = 50 \times 90$ per unit area. The solutions are obtained with a 14×14 mesh of the MITC3+, enriched MITC3+ and strain-smoothed MITC3+ shell elements. The reference solutions are calculated using a 32×32 mesh of the MITC9 shell elements. **Fig. 5.9** shows the load–displacement curves measured at points C and D. **Tables 5.2** and **5.3** present the relative errors in the displacements at point C and D, respectively, for each load step. **Fig. 5.10** depicts the final deformed configurations (at load level $f = f_{max}$) obtained using the strain-smoothed MITC3+ shell element. The strain-smoothed MITC3+ shell element gives the best solution among the shell elements considered.

5.2.2. Cantilever beam subjected to a tip moment

We consider a cantilever beam subjected to a tip moment $M_{max} = 10\pi$ as shown in **Fig. 5.11** [58]. The cantilever beam has unit thickness, and the Young's modulus and Poisson's ratio are given as $E = 1.2 \times 10^3$ and $\nu = 0.2$, respectively. The conditions are given so that the beam is sufficiently rolled up into a circular ring. The beam is modeled using regular and distorted 20×2 meshes of the MITC3+, enriched MITC3+ and strain-smoothed MITC3+ shell elements as shown in **Fig. 5.11**. The reference solutions are obtained using a regular 40×4 mesh of the MITC9 shell elements.

Figs. 5.12 and **5.13** present the resulting load–displacement curves measured at point A for the regular and distorted mesh, respectively. The deformed shapes of the beam at load levels $M = 0.25M_{max}$, $0.5M_{max}$, $0.75M_{max}$ and M_{max} for the regular mesh are depicted in **Fig. 5.14**. The strain-smoothed MITC3+ shell element provides the solutions closest to the reference. Also, in **Table 5.4** and **Fig. 5.15**, we compare the number of iterations that the Newton-Raphson method to converge for each load step. The number of iterations for the strain-smoothed MITC3+ element is almost the same as that of the reference.

5.2.3. Cantilever plate subjected to an end shear force

A cantilever plate is subjected to a distributed shearing force $p_{max} = 4$ at its free end as shown in **Fig. 5.16** [57]. The plate has a uniform thickness $h = 0.1$, and material properties are given as Young's modulus $E = 1.2 \times 10^6$ and Poisson's ratio $\nu = 0$. The plate is modeled using 16×1 meshes of the MITC3+ and strain-smoothed MITC3+ shell elements. The reference solutions are calculated using a 32×2 element mesh of the MITC9 shell elements.

The load–displacement curves evaluated at the loaded point A are given in **Fig. 5.17**, and the deformed configurations obtained using the strain-smoothed MITC3+ shell element at load steps $p = 0.25 p_{\max}$, $0.5 p_{\max}$, $0.75 p_{\max}$ and $p_{\max}$ are depicted in **Fig. 5.18**. The cumulative number of iterations that the Newton-Raphson method to converge for each load step are given in **Fig. 5.19**. The strain-smoothed MITC3+ shell element retains the excellent bending behavior of the MIT3+ shell element, and there is no increase in the iteration number in this example.

5.2.4. Slit annular plate subjected to a lifting line force

We solve a slit annular plate problem as shown in **Fig. 5.20** [58,69]. The shell thickness is $h = 0.03$, and material properties are $E = 2.1 \times 10^7$ and $\nu = 0$. A shearing force $p_{\max} = 0.8$ per unit length is incrementally acting on one end of the plate while the other end is clamped. The plate is modeled using a 6×30 mesh of the MITC3+, enriched MITC3+ and strain-smoothed MITC3+ shell elements. We obtain the reference solutions using a 12×60 mesh of the MITC9 shell elements.

The load–displacement curves evaluated at two distinct points B and C are presented in **Fig. 5.21**. The final deformed shapes obtained using the MITC3+ and strain-smoothed MITC3+ shell elements are compared with the reference in **Fig. 5.22**. The strain-smoothed MITC3+ shell element gives much better response prediction than the MITC3+ and enriched MITC3+ shell elements.

5.2.5. Column under a compressive load

A compressive load $P_{\max} = 4.5 \times 10^3$ is incrementally acting on point A of the column as shown in **Fig. 5.23** [58]. The column has unit thickness, and material properties are taken as $E = 10^6$ and $\nu = 0$. The column is modeled with $N \times 5N$ meshes (N = 2, 4, 8 and 16) of the MITC3+ and strain-smoothed MITC3+ shell elements, and a 20×100 mesh of the MITC9 shell elements to obtain the reference solutions.

In **Figs. 5.24** and **5.25**, we depict the load-displacement curves measured at point A with increasing the number of element layers N (N = 2, 4, 8 and 16). In **Fig. 5.26**, we compare the final displacements at point A for the various N. The deformed configurations at load levels $P = 0.5 P_{\max}$ and $P_{\max}$ obtained using the MITC3+, strain-smoothed MITC3+ and MITC9 shell elements are shown in **Fig. 5.27**. The von-Mises distributions for the element considered are depicted in **Fig. 5.28**. The solutions calculated using the strain-smoothed MITC3+ shell element agree very well with the reference solutions. In **Fig. 5.29**, we compare the total number of iterations to obtain the converged solutions for the MITC3+ and strain-smoothed MITC3+ shell elements for the various N. Both shell elements have similar iteration numbers.

5.2.6. Pull out of a free cylindrical shell

We last consider a free cylindrical shell pulled out by a pair of point loads $P_{max} = 4\times10^4$ at its center points as shown in **Fig. 5.30** [62,70]. The shell has a thickness of $h = 0.094$, and the Young's modulus and Poisson's ratio are taken as $E = 1.05\times10^7$ and $\nu = 0.3125$, respectively. We only model one-eighth of the shell considering its symmetry, and the corresponding boundary conditions are given as: $w = \beta = 0$ along AB, $v = \alpha = 0$ along AC and $u = \beta = 0$ along CD. The solutions are obtained using a 12×12 mesh of the MITC3+ and strain-smoothed MITC3+ shell elements. The reference solutions are obtained using a 32×32 mesh of the MITC9 shell elements.

The load–displacement curves of the shell evaluated at points C and D are given in **Fig. 5.31**, and the deformed configurations at load levels $P = P_{max}/3$ and P_{max} obtained using the strain-smoothed MITC3+ shell element are shown in **Fig. 5.32**. The strain-smoothed MITC3+ gives much accurate solutions compared with the MITC3+ shell element.

Table 5.2. Relative errors in the displacement ($\left|w_{ref} - w_h\right| / w_{ref} \times 100$) at point C for each load step for the Scordelis-Lo roof problem.

Load step	Relative error (%)		Reference solution
	MITC3+	Smoothed MITC3+	
1	3.647	1.414	-0.845
2	2.974	1.233	-1.292
3	2.401	1.009	-1.657
4	10.183	0.615	-2.464
5	9.461	1.679	-3.393
6	9.657	1.655	-4.223
7	9.233	1.216	-4.910
8	8.646	0.763	-5.440
9	8.225	0.454	-5.846
10	7.774	0.290	-6.169

Table 5.3. Relative errors in the displacement ($\left|v_{ref} - v_h\right| / v_{ref} \times 100$) at point D for each load step for the Scordelis-Lo roof problem.

Load step	Relative error (%)		Reference solution
	MITC3+	Smoothed MITC3+	
1	5.534	2.743	-0.845
2	4.625	5.172	-1.292
3	6.098	9.000	-1.657
4	47.175	2.587	-2.464
5	27.392	5.398	-3.393
6	25.779	4.829	-4.223
7	25.078	3.484	-4.910
8	23.257	2.341	-5.440
9	21.874	1.542	-5.846
10	21.190	1.081	-6.169

Table 5.4. The number of iterations that the Newton-Raphson method to converge for each load step for the cantilever beam subjected to a tip moment.

Load step	MITC3+	Smoothed MITC3+	MITC9	Load step	MITC3+	Smoothed MITC3+	MITC9
1	3	4	4	11	4	7	7
2	3	5	5	12	4	7	7
3	3	5	5	13	4	7	7
4	3	6	6	14	4	7	7
5	3	6	6	15	4	7	7
6	3	6	6	16	4	7	7
7	3	6	6	17	4	7	7
8	4	6	6	18	4	7	6
9	4	7	7	19	4	7	6
10	4	7	7	20	4	7	7
Total iteration number					73	128	126

Table 5.5. Relative errors in the final displacement ($\left|v_{ref} - v_h\right| / v_{ref} \times 100$) at point A for the column under a compressive load.

N	MITC3+	Smoothed MITC3+
2	96.607	6.077
4	34.498	0.829
8	8.649	0.105
16	2.202	0.033
Reference solution: $v_{ref} = -10.773$		

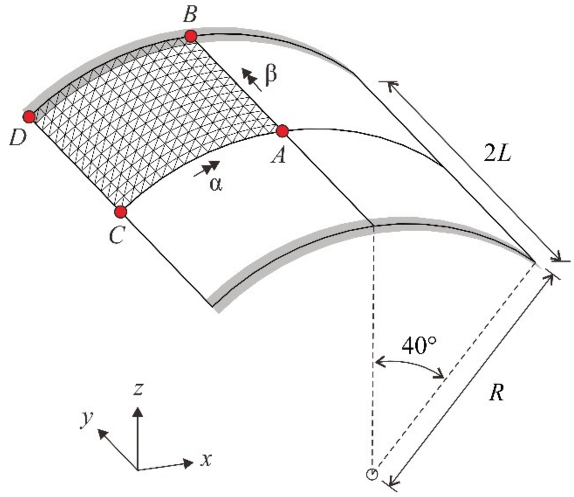

Fig. 5.6. Scordelis-Lo roof problem.

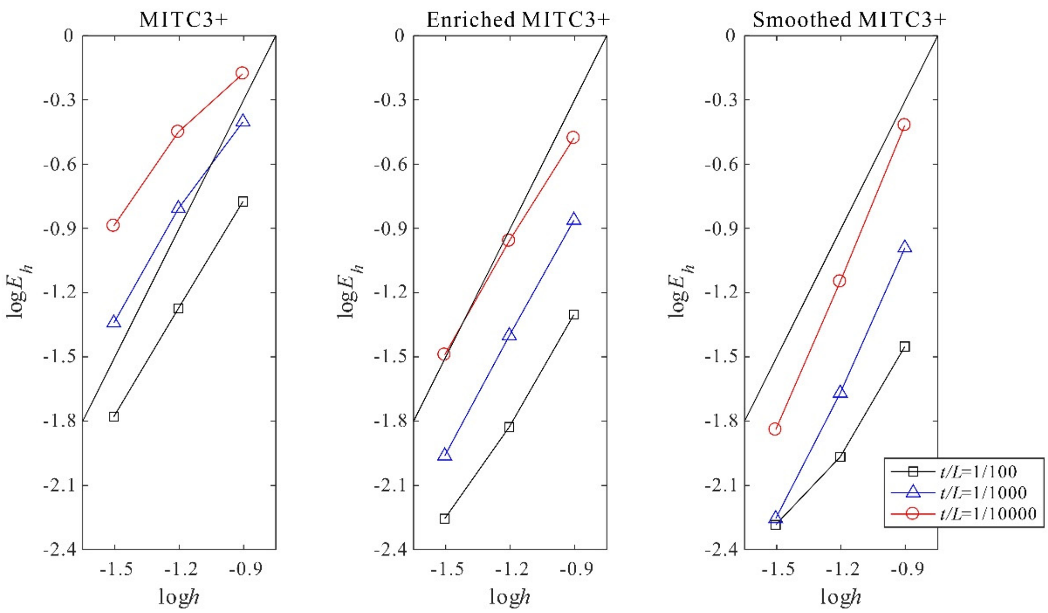

Fig. 5.7. Convergence curves for the Scordelis-Lo roof problem. The bold line represents the optimal convergence rate.

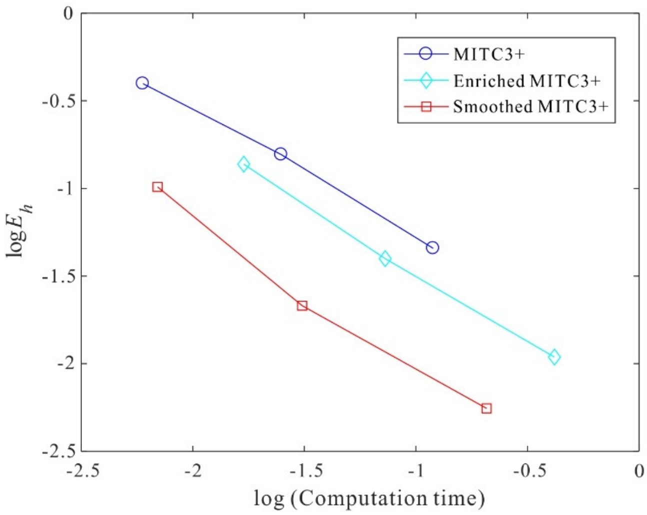

Fig. 5.8. Computational efficiency curves for the Scordelis-Lo roof problem. The computation times are measured in seconds.

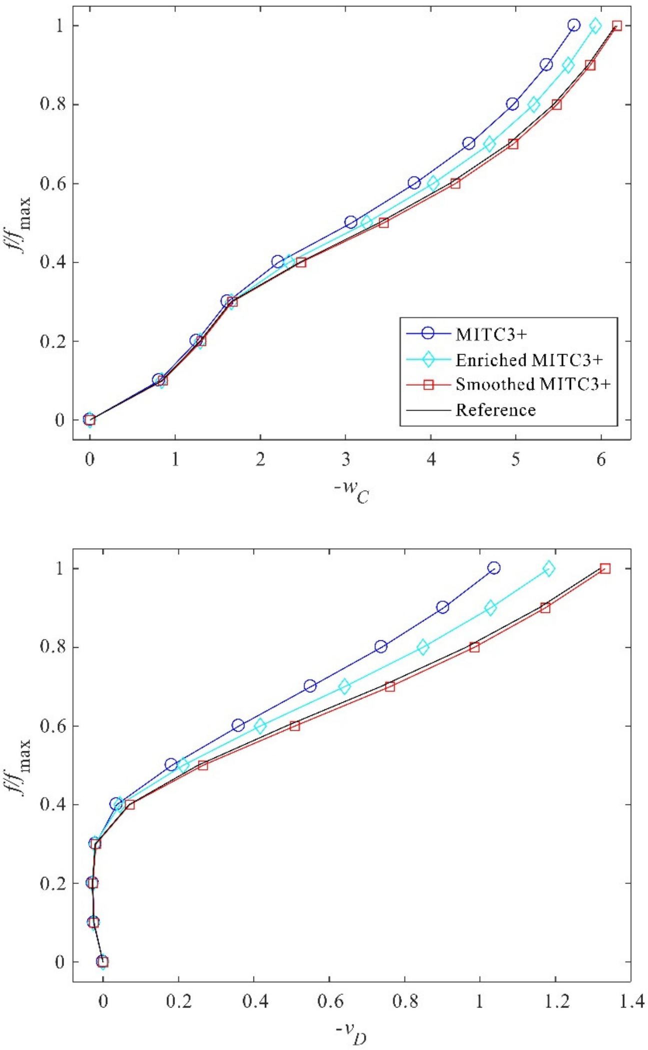

Fig. 5.9. Load-displacement curves ($-w_C$ and $-v_D$) for the Scordelis-Lo roof problem.

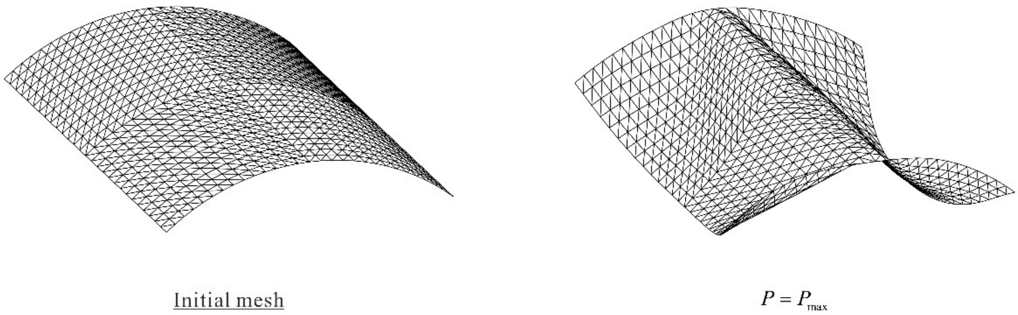

Fig. 5.10. Final deformed configuration of the Scordelis-Lo roof obtained using the strain-smoothed MITC3+ shell element.

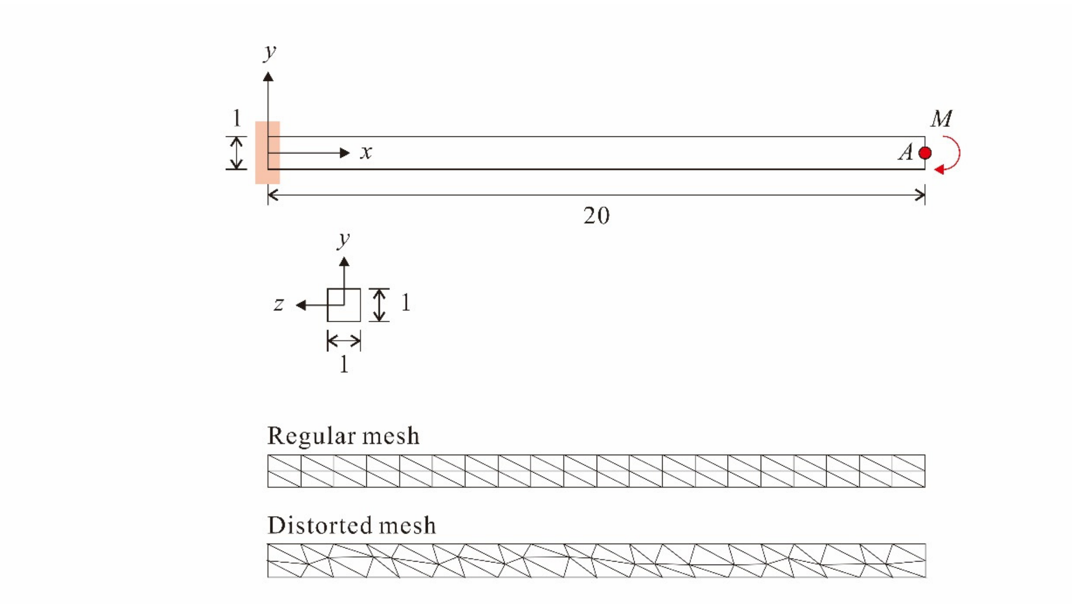

Fig. 5.11. Cantilever beam subjected to a tip moment, and regular and distorted 20×2 meshes.

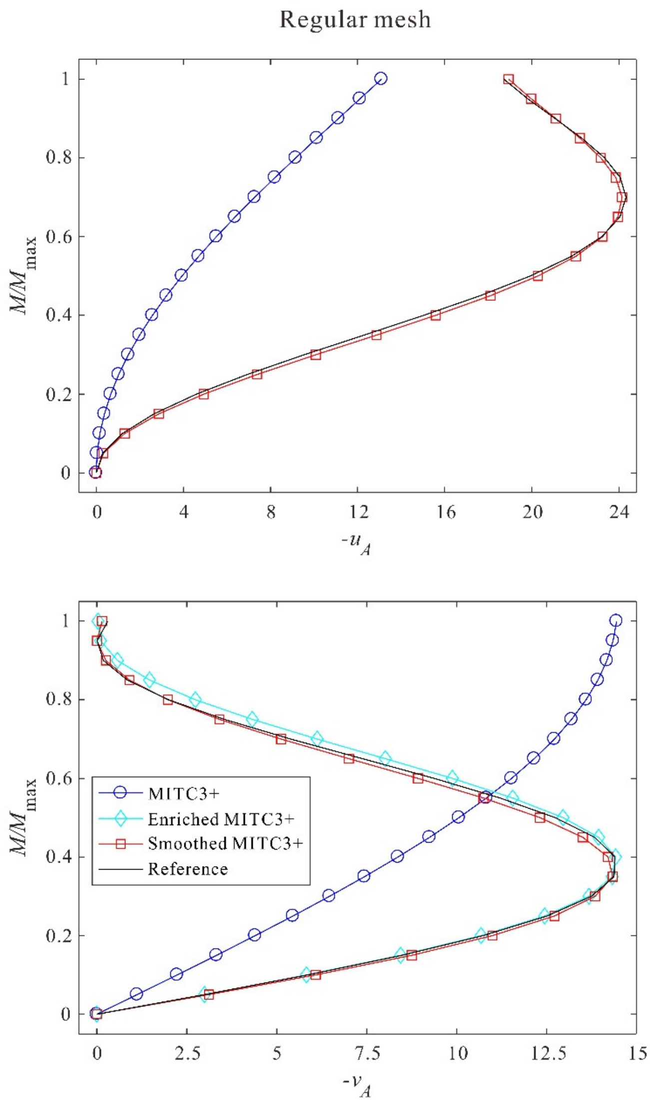

Fig. 5.12. Load-displacement curves ($-u_A$ and $-v_A$) for the cantilever beam subjected to a tip moment when the regular mesh is used.

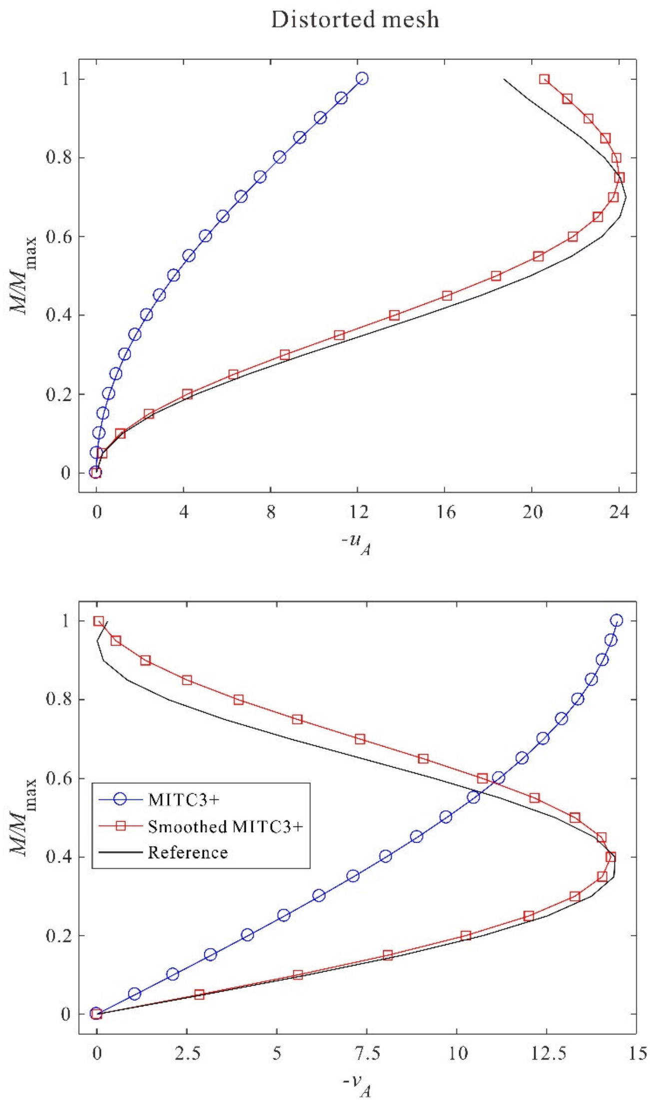

Fig. 5.13. Load-displacement curves ($-u_A$ and $-v_A$) for the cantilever beam subjected to a tip moment when the distorted mesh is used.

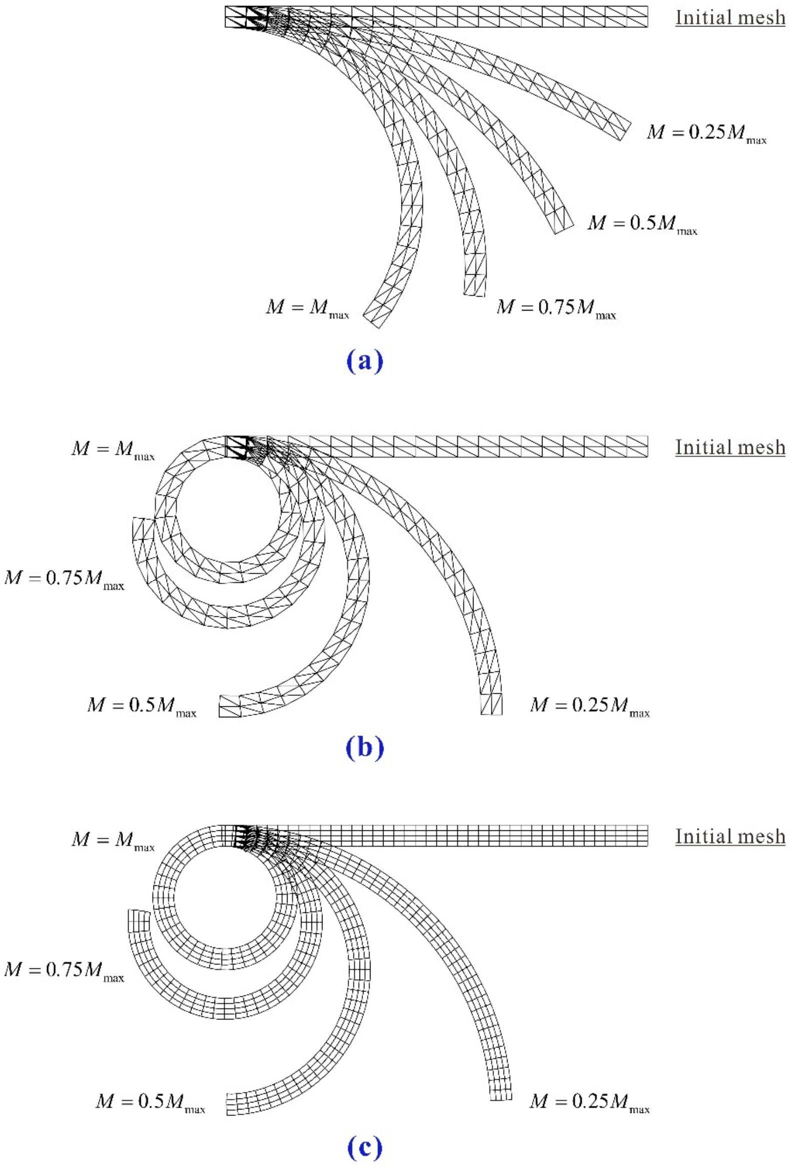

Fig. 5.14. Deformed configurations of the cantilever beam subjected to a tip moment at several load levels obtained using (a) regular 20×2 mesh of the MITC3+ elements, (b) regular 20×2 mesh of the strain-smoothed MITC3+ elements and (c) regular 40×4 mesh of the MITC9 shell elements (reference).

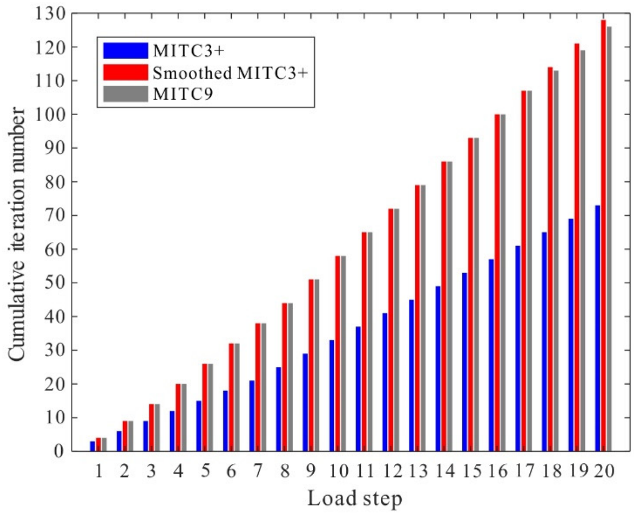

Fig. 5.15. The cumulative number of iterations that the Newton-Raphson method to converge for the cantilever beam subjected to a tip moment.

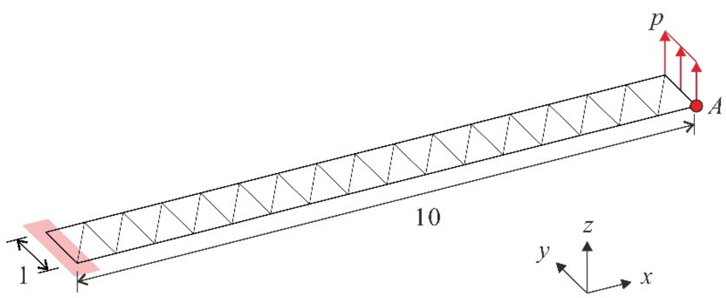

Fig. 5.16. Cantilever plate subjected to an end shear force.

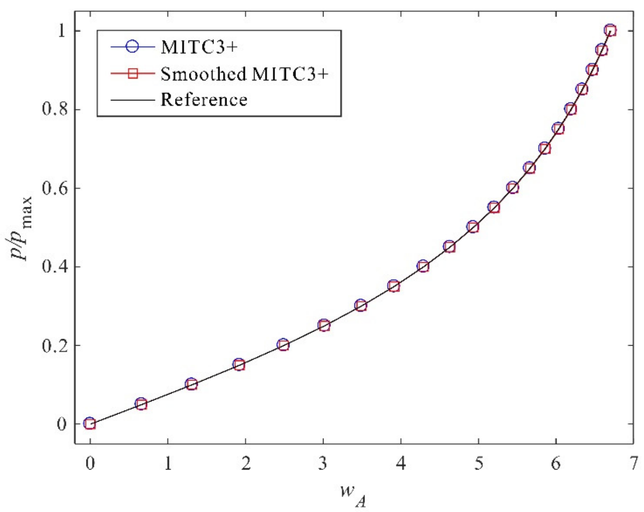

Fig. 5.17. Load-displacement curves (w_A) for the cantilever plate subjected to an end shear force.

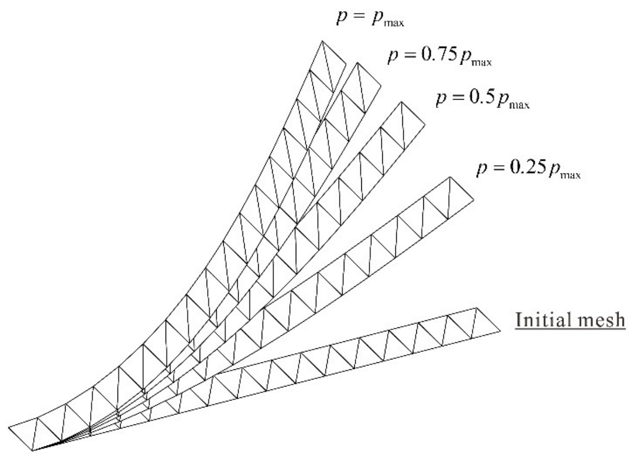

Fig. 5.18. Deformed configurations of the cantilever plate subjected to an end shear force at several load levels obtained using the strain-smoothed MITC3+ shell element.

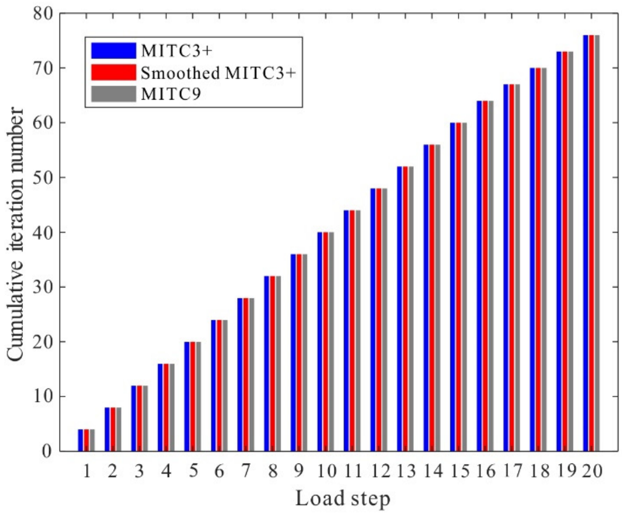

Fig. 5.19. The cumulative number of iterations that the Newton-Raphson method to converge for the cantilever plate subjected to an end shear force.

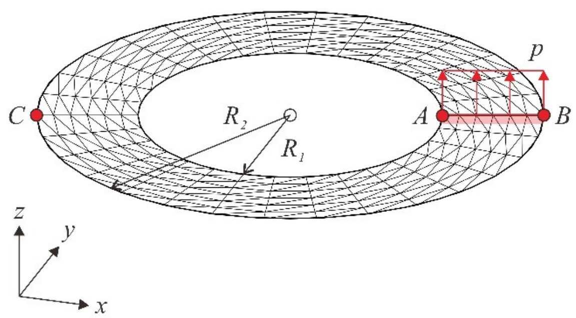

Fig. 5.20. Slit annular plate subjected to a lifting line force.

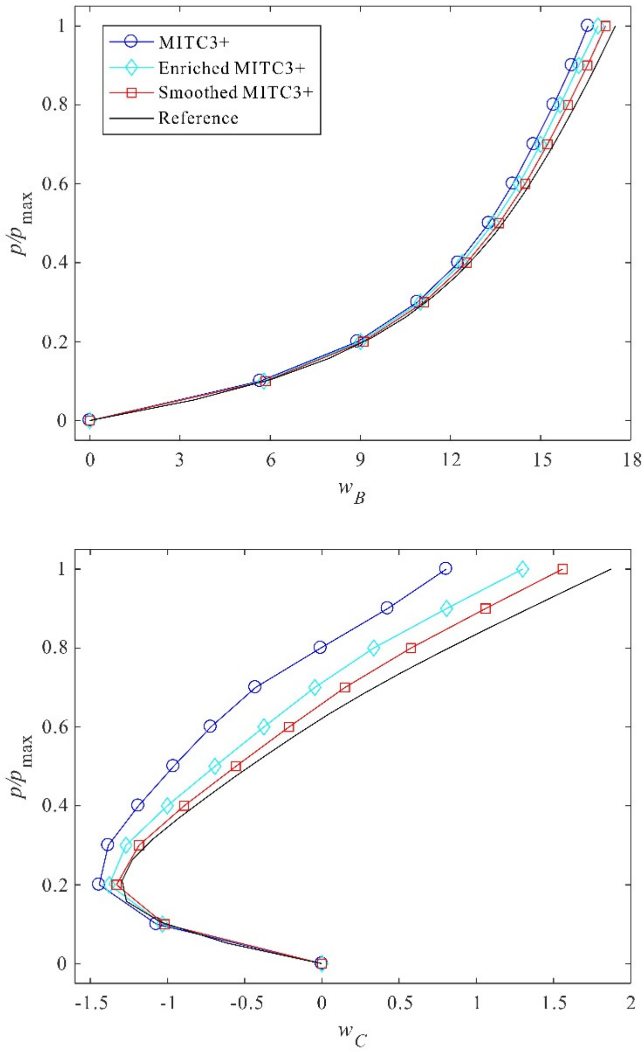

Fig. 5.21. Load-displacement curves (w_B and w_C) for the slit annular plate subjected to a lifting line force.

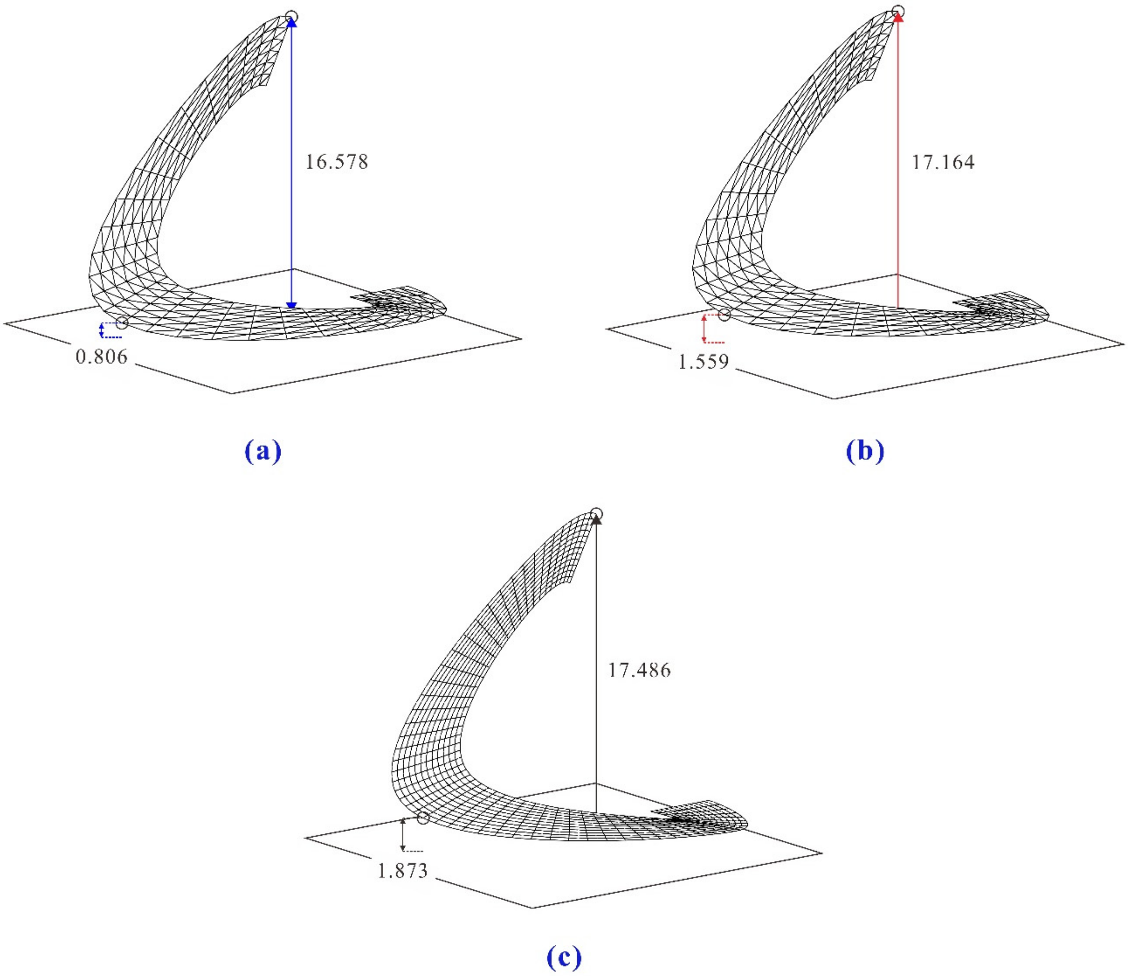

Fig. 5.22. Final deformed configurations of the slit annular plate subjected to a lifting line force obtained using (a) 6×30 mesh of the MITC3+ elements, (b) 6×30 mesh of the strain-smoothed MITC3+ elements and (c) 12×60 mesh of the MITC9 shell elements (reference).

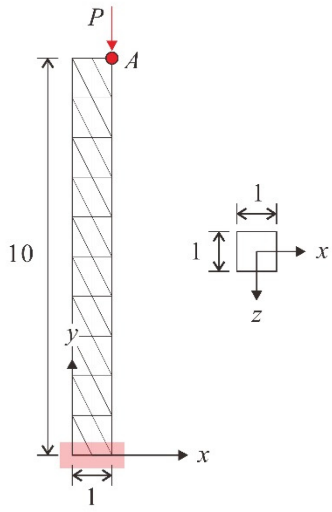

Fig. 5.23. Column under a compressive load.

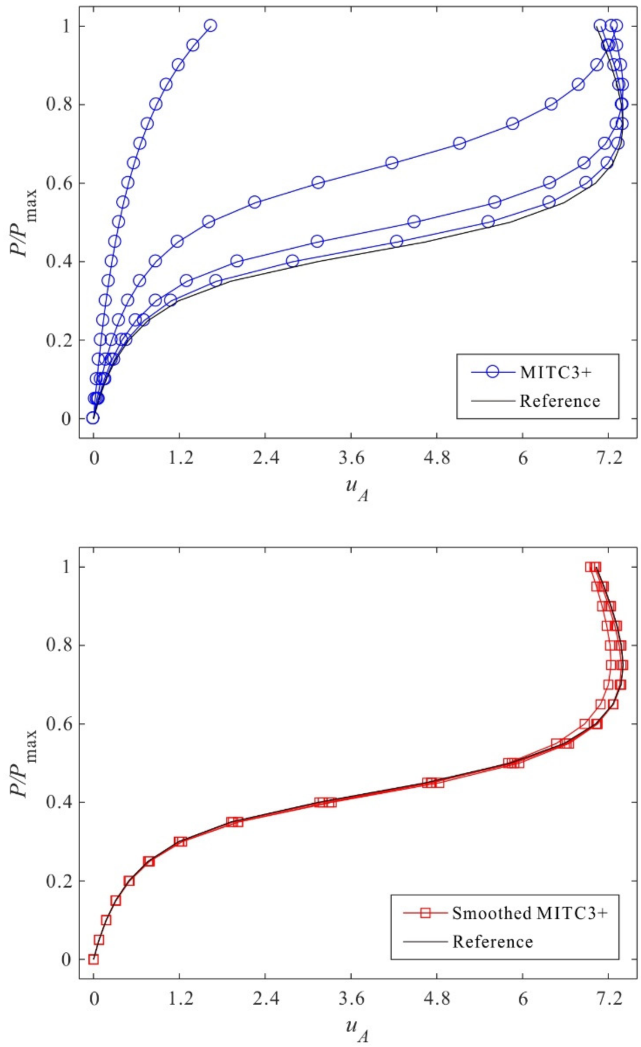

Fig. 5.24. Load-displacement curves (u_A) for the column under a compressive load with increasing the number of element layers N (N = 2, 4, 8 and 16).

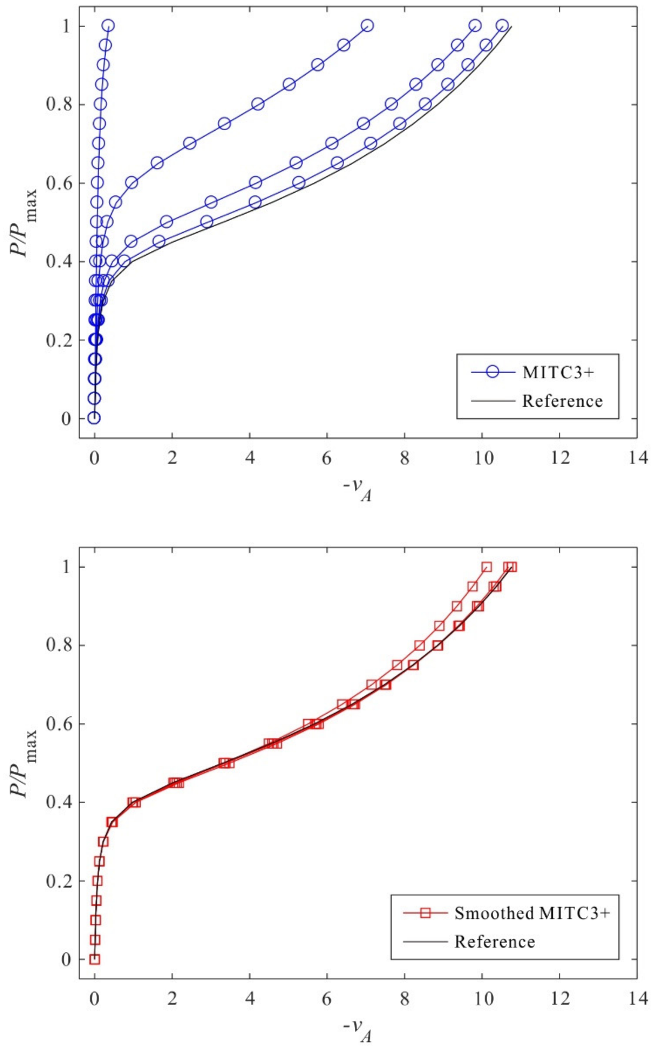

Fig. 5.25. Load-displacement curves ($-v_A$) for the column under a compressive load with increasing the number of element layers N (N = 2, 4, 8 and 16).

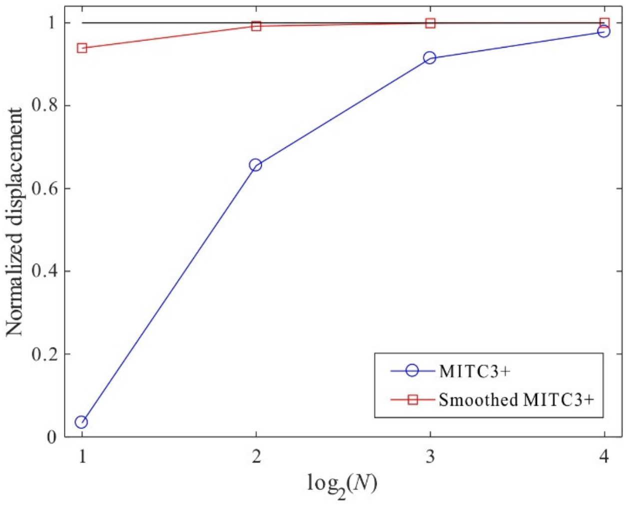

Fig. 5.26. Normalized final displacements (v_h / v_{ref}) at point A for the column under a compressive load for the various number of element layers N (N = 2, 4, 8 and 16).

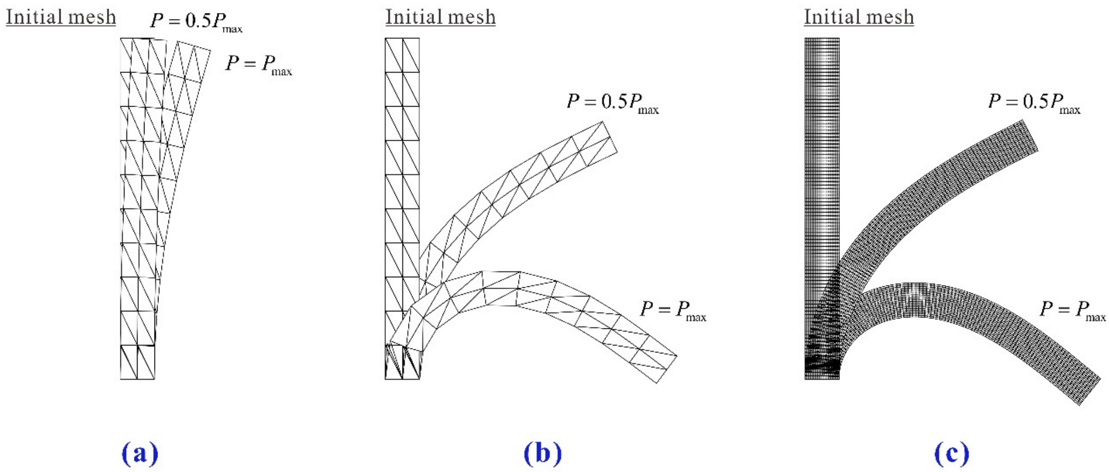

Fig. 5.27. Deformed configurations of the column under a compressive load at several load levels obtained using (a) 2×10 mesh of the MITC3+ elements, (b) 2×10 mesh of the strain-smoothed MITC3+ elements and (c) 20×100 mesh of the MITC9 elements (reference).

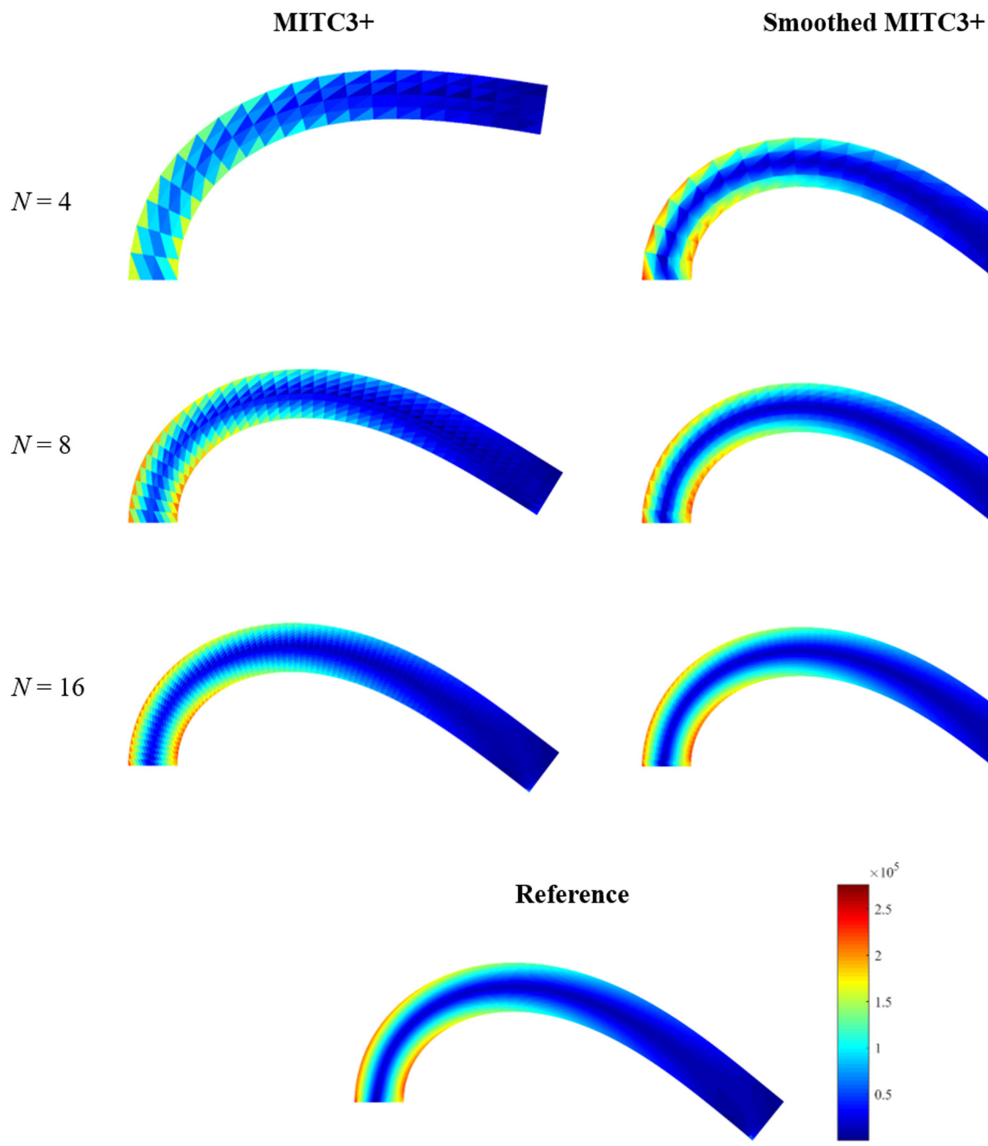

Fig. 5.28. von Mises stress distributions of the column under a compressive load at the final load level obtained using $N \times 5N$ meshes (N = 4, 8 and 16) of the MITC3+ and strain-smoothed MITC3+ shell elements. The reference distribution is obtained using a 20×100 mesh of the MITC9 elements.

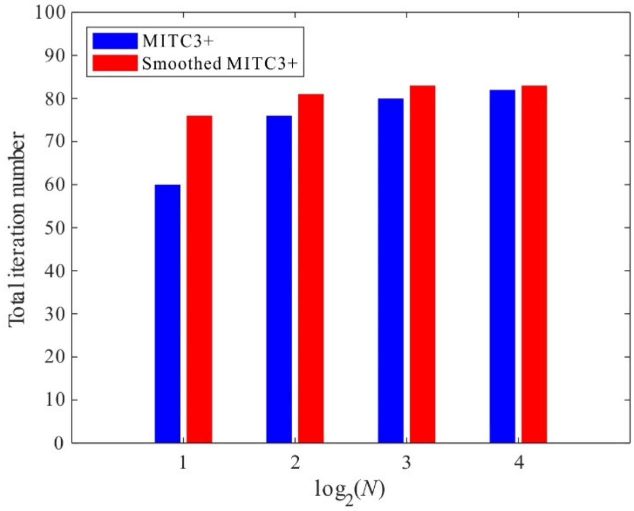

Fig. 5.29. The total number of iterations to obtain converged solutions for the column under a compressive load for the various number of element layers N (N = 2, 4, 8 and 16).

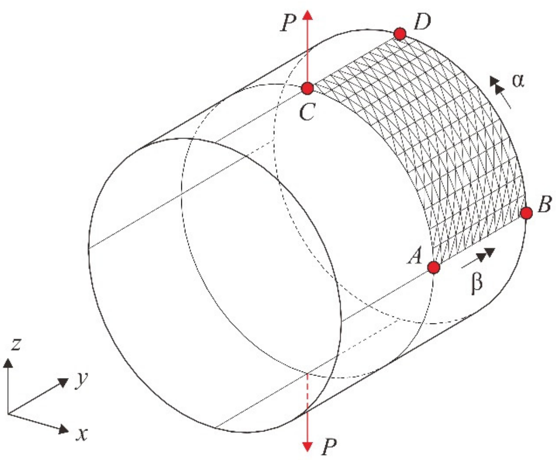

Fig. 5.30. Pull-out of a free cylindrical shell.

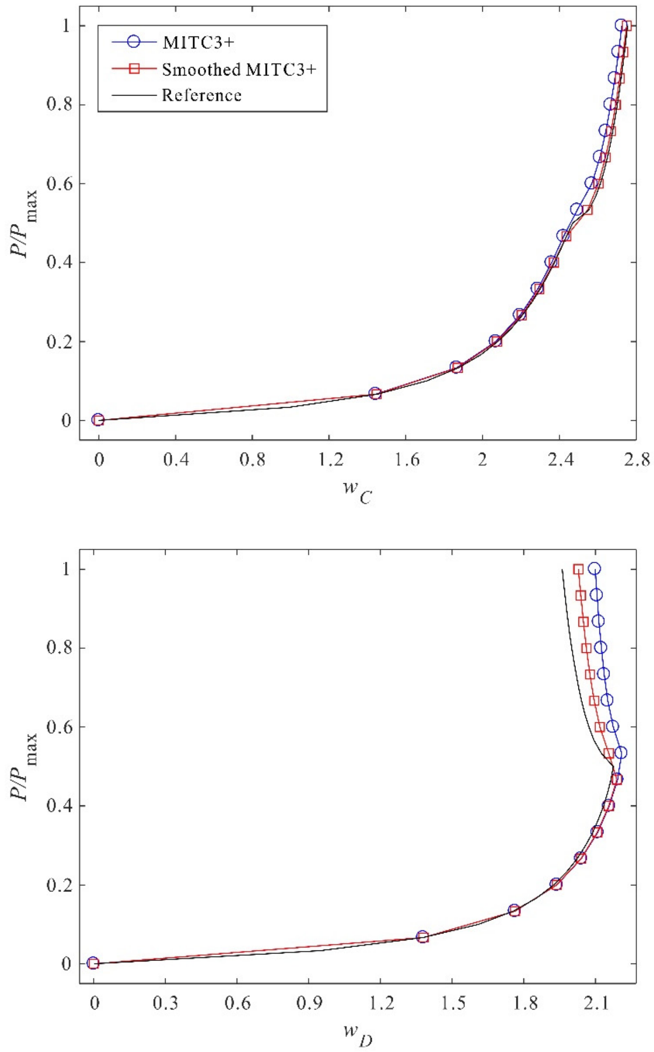

Fig. 5.31. Load-displacement curves (w_C and w_D) for the pull-out of a free cylindrical shell.

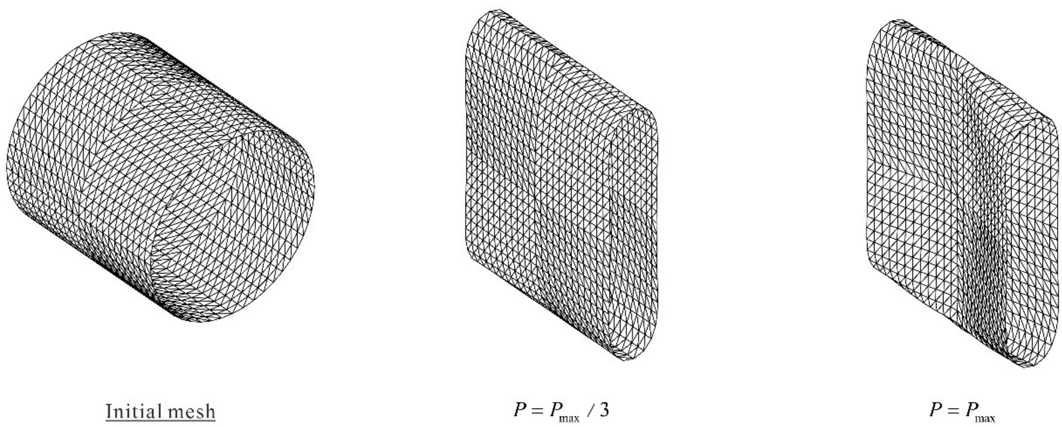

Fig. 5.32. Deformed configurations of the pull-out of a free cylindrical shell at several load levels obtained using the strain-smoothed MITC3+ shell element.

Chapter 6. A variational framework for the strain-smoothed element method

6.1. Introduction

For several decades, substantial efforts have been made to the development of low-order finite elements which exhibit high accuracy in coarse meshes. One major attempt is the assumed strain methods in which the standard discrete gradient operator is replaced with an assumed form [42,44,48]. The assumed strain methods effectively alleviate locking in finite elements and can be formulated within the framework of the Hu-Washizu variational principle [45]. The smoothed finite element methods (S-FEMs) are also good examples. The S-FEMs construct smoothing domains based on edges, nodes, or cells, and piecewise constant strain fields are constructed for the smoothing domains. They improve the performance of finite elements without using additional DOFs through strain smoothing. Theoretical studies on the S-FEMs were conducted, and a variational framework was established based on the Hellinger-Reissner principle [71,72].

In the previous chapters, the properties of the strain-smoothed element (SSE) method have been verified by numerical means. In this chapter, a theoretical framework for the SSE method is established. A variational principle for the SSE method is constructed and convergence and stability analyses are performed based on the defined variational principle.

The displacement variational formulation for linear elasticity is reviewed in Sect. 6.2. In Sect. 6.3, we introduce the SSE method and show that the method can be interpreted using projection operators. The variational framework for the SSE method is established in Sect. 6.4. In Sect. 6.5, the convergence theory for the SSE method based on the variational principle established in Sect. 6.4 is presented.

6.1.1. Contribution

Research to establish a variational framework for the strain-smoothed method has been conducted with Dr. Jongho Park, a postdoctoral researcher at the Department of Mathematical Sciences, KAIST.

6.2. Linear elasticity

Let $\Omega \subset \mathbb{R}^2$ be a bounded and polygonal domain representing a two-dimensional linear elastic solid. The boundary $\partial\Omega$ of Ω consists of two parts $\Gamma_D \neq \varnothing$ and $\Gamma_N = \partial\Omega \setminus \Gamma_D$. The displacement field $\mathbf{u}$ and the stress field $\boldsymbol{\sigma}$ satisfy the Dirichlet boundary condition

$$\mathbf{u} = \mathbf{u}_\Gamma \quad \text{on} \quad \Gamma_D \tag{6.2.1}$$

and the Neumann boundary condition

$$\mathbf{A\sigma} = \mathbf{t} \quad \text{on} \quad \Gamma_N \tag{6.2.2}$$

for some prescribed displacement $\mathbf{u}_\Gamma$ and traction $\mathbf{t}$, respectively. In (6.2.2), the matrix $\mathbf{A}$ is given by

$$\mathbf{A} = \begin{bmatrix} n_1 & 0 & n_2 \\ 0 & n_2 & n_1 \end{bmatrix},$$

where $\mathbf{n} = \begin{bmatrix} n_1 & n_2 \end{bmatrix}^T$ is the unit outward normal to Γ_N.

In the following, we summarize three governing equations for linear elasticity. Let $\boldsymbol{\varepsilon}$ denote the strain field. The compatibility relation between the displacement $\mathbf{u}$ and the strain $\boldsymbol{\varepsilon}$ reads as

$$\boldsymbol{\varepsilon} = \mathbf{Bu} \quad \text{in} \quad \Omega, \tag{6.2.3}$$

Where $\mathbf{B}$ is a matrix of differential operators given by

$$\mathbf{B} = \begin{bmatrix} \dfrac{\partial}{\partial x} & 0 \\ 0 & \dfrac{\partial}{\partial y} \\ \dfrac{\partial}{\partial y} & \dfrac{\partial}{\partial x} \end{bmatrix}.$$

The stress-strain constitutive equation is written as follows:

$$\boldsymbol{\sigma} = \mathbf{D}\boldsymbol{\varepsilon} \quad \text{in} \quad \Omega, \tag{6.2.4}$$

where $\mathbf{D}$ is a 3×3 symmetric and positive definite matrix which relies on a material composing the elastic solid. We assume that the material is uniform, i.e., $\mathbf{D}$ is constant in Ω.

The equilibrium equation is stated as

$$\text{div}\boldsymbol{\sigma} + \mathbf{b} = \mathbf{0} \quad \text{in} \quad \Omega, \tag{6.2.5}$$

where $\mathbf{b}$ is a body force.

Combining (6.2.3), (6.2.4), and (6.2.5) with the boundary conditions (6.2.1) and (6.2.2), we have the following displacement formulation for linear elasticity:

$$\begin{aligned} &-\text{div}(\mathbf{DBu}) = \mathbf{b} \quad \text{in} \quad \Omega, \\ &\mathbf{u} = \mathbf{u}_\Gamma \quad \text{on} \quad \Gamma_D, \quad \mathbf{A\sigma} = \mathbf{t} \quad \text{on} \quad \Gamma_N. \end{aligned} \tag{6.2.6}$$

In what follows, we set $\mathbf{u}_\Gamma = \mathbf{0}$ in (6.2.6) for the sake of convenience.

Next, we consider the weak formulation of (6.2.6), i.e., the displacement variational formulation for linear elasticity. Let V be a space of kinematically admissible displacement fields defined as

$$V = \left\{ \mathbf{u} \in (H^1(\Omega))^2 : \mathbf{u} = \mathbf{0} \text{ on } \Gamma_D \right\}.$$

A space W of strain and stress fields is given by
$W = (L^2(\Omega))^3$.

A bilinear form $a(\cdot,\cdot)$ on V is defined by

$$a(\mathbf{u},\mathbf{v}) = \int_\Omega \mathbf{D}\boldsymbol{\varepsilon}[\mathbf{u}] : \boldsymbol{\varepsilon}[\mathbf{v}]\, d\Omega, \quad \mathbf{u},\mathbf{v} \in V, \tag{6.2.7}$$

where $\boldsymbol{\varepsilon}[\mathbf{u}] = \mathbf{B}\mathbf{u}$ and the symbol : denotes the Euclidean inner product in $\mathbb{R}^3$. Note that for $\mathbf{u} \in V$, we have $\boldsymbol{\varepsilon}[\mathbf{u}] \in W$. Clearly, $a(\cdot,\cdot)$ is symmetric, continuous, and coercive.

Let f denote a continuous linear functional on V given by
$f(\mathbf{u}) = \int_\Omega \mathbf{b}\cdot\mathbf{u}\, d\Omega + \int_{\Gamma_N} \mathbf{t}\cdot\mathbf{u}\, d\Gamma, \quad \mathbf{u} \in V$.

It is well-known that (see, e.g., [73]) a solution of (6.2.6) is characterized by the following variational problem: find $\mathbf{u} \in V$ such that

$$a(\mathbf{u},\mathbf{v}) = f(\mathbf{v}), \quad \forall \mathbf{v} \in V. \tag{6.2.8}$$

By the Lax-Milgram theorem (see, e.g., [73, Theorem 2.7.7]), the problem (6.2.8) has a unique solution and it solves the following quadratic optimization problem:

$$\min_{\mathbf{u}\in V} \left\{ \frac{1}{2} a(\mathbf{u},\mathbf{u}) - f(\mathbf{u}) \right\}. \tag{6.2.9}$$

6.3. The strain-smoothed element method

This section is devoted to a brief introduction to the SSE method for solving (6.2.8). We closely follow the explanation presented in [22] for the method. In addition, we present an alternative view to the SSE method that the method can be described in terms of orthogonal projection operators defined on particular meshes. We note that similar discussions were made in [72] for the S-FEMs.

For a subregion K of Ω and a nonnegative integer n, let $P_n(K)$ denote the collection of all polynomials of degree less than or equal to n on K. Let $\mathcal{T}_h$ be a triangulation of Ω with the maximum element diameter $h > 0$.

We set the discrete displacement space $V_h \subset V$ as the collection of the continuous and piecewise linear functions on $\mathcal{T}_h$ satisfying the homogeneous Dirichlet boundary condition on Γ_D, i.e.,
$V_h = \left\{ \mathbf{u} \in V : \mathbf{u}|_T \in (P_1(T))^2 \ \forall T \in \mathcal{T}_h \right\}$.

We define the discrete strain/stress space W_h associated to the subdivision $\mathcal{T}_h$ by

$W_h = \left\{ \boldsymbol{\varepsilon} \in W : \boldsymbol{\varepsilon}\big|_T \in (P_0\,(T))^2 \;\; \forall T \in \mathcal{T}_h \right\}$.

It is clear that $\boldsymbol{\varepsilon}[\mathbf{u}] = \mathbf{Bu}$ and $\boldsymbol{\sigma}[\mathbf{u}] = \mathbf{DBu}$ belong to W_h when $\mathbf{u} \in V_h$.

The standard FEM for linear elasticity in (6.2.8) solves the Galerkin approximation of (6.2.8) defined on V_h: find $\mathbf{u}_h \in V_h$ such that

$a(\mathbf{u}_h, \mathbf{v}) = f(\mathbf{v})$, $\forall \mathbf{v} \in V_h$,

where the bilinear form $a(\cdot,\cdot)$: $V_h \times V_h \to \mathbb{R}$ was given in (6.2.7). In the strain-smoothing approach [22], we use an alternative bilinear form $\overline{a}(\cdot,\cdot)$: $V_h \times V_h \to \mathbb{R}$ made by replacing $\boldsymbol{\varepsilon}[\mathbf{u}]$ in (6.2.7) by an appropriate smoothed strain field $\overline{\boldsymbol{\varepsilon}}[\mathbf{u}]$, i.e.,

$$\overline{a}(\mathbf{u}, \mathbf{v}) = \int_\Omega \mathbf{D}\overline{\boldsymbol{\varepsilon}}[\mathbf{u}] : \overline{\boldsymbol{\varepsilon}}[\mathbf{v}]\, d\Omega, \quad \mathbf{u}, \mathbf{v} \in V_h. \tag{6.3.1}$$

In the following, we present how to construct the SSE smoothing operator S_h: $W_h \to \overline{W}_h$ which maps a given strain field $\boldsymbol{\varepsilon} \in W_h$ to the corresponding smoothed strain field $\overline{\boldsymbol{\varepsilon}} \in \overline{W}_h$, where

$\overline{W}_h = \left\{ \overline{\boldsymbol{\varepsilon}} \in W : \overline{\boldsymbol{\varepsilon}}\big|_T \in (P_1\,(T))^3 \;\; \forall T \in \mathcal{T}_h \right\}$.

That is, the resulting $\overline{\boldsymbol{\varepsilon}} = S_h \boldsymbol{\varepsilon}$ shall be piecewise linear. Take any element $T \in \mathcal{T}_h$. We assume for simplicity that T is an interior element, i.e., there exist three elements T_1, T_2, and T_3 in $\mathcal{T}_h$ adjacent to T as shown in **Fig. 6.1**(a); for the case of exterior elements, see [22].

Intermediate smoothed strains $\hat{\boldsymbol{\varepsilon}}^{(i)} \in \mathbb{R}^3$, $i = 1, 2, 3$, are defined by

$$\hat{\boldsymbol{\varepsilon}}^{(i)} = \frac{1}{|T \cup T_i|} \int_{T \cup T_i} \boldsymbol{\varepsilon}\, d\Omega. \tag{6.3.2}$$

Using the intermediate smoothed strains in (6.3.2), we assign the pointwise values of $\overline{\boldsymbol{\varepsilon}}$ at three Gauss integration points ($G1$, $G2$ and $G3$ in **Fig. 6.2**) of T in the following manner:

$$\overline{\boldsymbol{\varepsilon}}(Gi) = \frac{1}{2}(\hat{\boldsymbol{\varepsilon}}^{(j)} + \hat{\boldsymbol{\varepsilon}}^{(k)}), \tag{6.3.3}$$

where $i = 1$, 2, 3 and $\{i, j, k\} = \{1, 2, 3\}$. From (6.3.3), the smoothed strain field $\overline{\boldsymbol{\varepsilon}}$ in (6.3.1) is uniquely determined on T by linear interpolation.

Finally, we have

$$\bar{a}(\mathbf{u},\mathbf{v}) = \int_\Omega \mathbf{D} S_h \boldsymbol{\varepsilon}[\mathbf{u}] : S_h \boldsymbol{\varepsilon}[\mathbf{v}] \, d\Omega \,, \quad \mathbf{u},\mathbf{v} \in V_h \tag{6.3.4}$$

and solve the following problem: find $\bar{\mathbf{u}}_h \in V_h$ such that

$$\bar{a}(\bar{\mathbf{u}}_h,\mathbf{v}) = f(\mathbf{v}) \,, \quad \forall \mathbf{v} \in V_h \,. \tag{6.3.5}$$

6.3.1. An alternative view: twice-projected strain

We present an alternative derivation of the SSE method which will be useful in the convergence analysis of the method. An alternative smoothed strain field $\bar{\boldsymbol{\varepsilon}}$ defined in the following is different from the one explained above, but eventually give an equivalent formulation to (6.3.5).

We construct two subdivisions $\mathcal{T}_{1,h}$ and $\mathcal{T}_{2,h}$ of Ω other than $\mathcal{T}_h$ as follows. For two neighboring elements T_1 and T_2, let e be the edge shared by them. Then we consider the quadrilateral whose vertices are the endpoints of e and the centroids of T_1, T_2. We define $\mathcal{T}_{1,h}$ as the collection of such quadrilaterals. In order to construct $\mathcal{T}_{2,h}$, we partition each element of $\mathcal{T}_h$ into three pieces by joining the centroid and the midpoints of element edges. Then $\mathcal{T}_{2,h}$ is defined as the collection of such pieces. **Fig. 6.3** displays $\mathcal{T}_h$, $\mathcal{T}_{1,h}$, and $\mathcal{T}_{2,h}$. For k = 1, 2, let $W_{k,h} \subset W$ be the collection of piecewise constant functions on $\mathcal{T}_{k,h}$, i.e., $W_{k,h} = \left\{ \boldsymbol{\varepsilon} \in W : \boldsymbol{\varepsilon}|_T \in (P_0(T))^3 \ \forall T \in \mathcal{T}_{k,h} \right\}$.

The piecewise smoothing operator $P_{k,h} : W \to W_{k,h}$ is defined by

$$(P_{k,h}\boldsymbol{\varepsilon})(x) = \frac{1}{|T|} \int_T \boldsymbol{\varepsilon} \, d\Omega \,, \quad \boldsymbol{\varepsilon} \in W \,, \quad T \in \mathcal{T}_{k,h} \,, \quad x \in T \,. \tag{6.3.6}$$

It was observed in [72] that piecewise smoothing operators of the form (6.3.6) are in fact orthogonal projectors; rigorous statements are given in the following lemmas.

Lemma 3.1. *Let* $\mathbf{A}$ *be a* 3×3 *matrix. For* k *= 1, 2, the piecewise smoothing operator* $P_{k,h}$ *commutes with* $\mathbf{A}$, *i.e.,*

$P_{k,h}(\mathbf{A}\boldsymbol{\varepsilon}) = \mathbf{A} P_{k,h} \boldsymbol{\varepsilon} \,, \quad \boldsymbol{\varepsilon} \in W$.

Proof. It is elementary.

Lemma 3.2. *For $k = 1, 2$, the piecewise smoothing operator $P_{k,h}$ is the $(L^2(\Omega))^3$-orthogonal projection onto $W_{k,h}$, i.e., $P_{k,h}^2 = P_{k,h}$ and*

$\int_\Omega P_{k,h}\boldsymbol{\varepsilon} : \boldsymbol{\delta}\, d\Omega = \int_\Omega \boldsymbol{\varepsilon} : P_{k,h}\boldsymbol{\delta}\, d\Omega$, $\boldsymbol{\varepsilon}, \boldsymbol{\delta} \in W$.

Proof. See [72, Remarks 2 and 4].

Now, we set $\overline{\boldsymbol{\varepsilon}} = P_{2,h}P_{1,h}\boldsymbol{\varepsilon}$ in (6.3.1). That is, we have

$$\overline{a}(\mathbf{u},\mathbf{v}) = \int_\Omega \mathbf{D}P_{2,h}P_{1,h}\boldsymbol{\varepsilon}[\mathbf{u}] : P_{2,h}P_{1,h}\boldsymbol{\varepsilon}[\mathbf{v}]\, d\Omega, \quad \mathbf{u},\mathbf{v} \in V_h. \tag{6.3.7}$$

We note that $\overline{\boldsymbol{\varepsilon}} = P_{2,h}P_{1,h}\boldsymbol{\varepsilon} \in W_{2,h}$ in (6.3.7) while its counterpart $\overline{\boldsymbol{\varepsilon}} = S_h\boldsymbol{\varepsilon}$ belongs to $\overline{W}_h$. Even though (6.3.4) and (6.3.7) use different smoothed strain fields to each other, one can prove that they result the same bilinear form $\overline{a}(\cdot,\cdot)$.

Theorem 3.3. *Two bilinear forms in* (6.3.4) *and* (6.3.7) *are identical, i.e., it satisfies that*

$\int_\Omega \mathbf{D}S_h\boldsymbol{\varepsilon}[\mathbf{u}] : S_h\boldsymbol{\varepsilon}[\mathbf{v}]\, d\Omega = \int_\Omega \mathbf{D}P_{2,h}P_{1,h}\boldsymbol{\varepsilon}[\mathbf{u}] : P_{2,h}P_{1,h}\boldsymbol{\varepsilon}[\mathbf{v}]\, d\Omega$, $\mathbf{u},\mathbf{v} \in V_h$.

Proof. Thanks to the polarization identity [74, Theorem 0.19], it suffices to show that

$\int_T \mathbf{D}S_h\boldsymbol{\varepsilon}[\mathbf{u}] : S_h\boldsymbol{\varepsilon}[\mathbf{u}]\, d\Omega = \int_T \mathbf{D}P_{2,h}P_{1,h}\boldsymbol{\varepsilon}[\mathbf{u}] : P_{2,h}P_{1,h}\boldsymbol{\varepsilon}[\mathbf{u}]\, d\Omega$,

for $\mathbf{u} \in V_h$ and $T \in \mathcal{T}_h$. We take any $\mathbf{u} \in V_h$ and write $\boldsymbol{\varepsilon} = \boldsymbol{\varepsilon}[\mathbf{u}]$. Assume that T is an interior element; the exterior case can be treated in similarly. Let T_i, $i = 1, 2, 3$ be neighboring elements of T in $\mathcal{T}_h$; see **Fig. 6.1**(a). We denote the values of $\boldsymbol{\varepsilon}$ on the elements T and T_i by $\boldsymbol{\varepsilon}_T$ and $\boldsymbol{\varepsilon}_{T_i}$, respectively.

Since three-point Gaussian integration is exact for linear functions, we have

$\int_T \mathbf{D}S_h\boldsymbol{\varepsilon} : S_h\boldsymbol{\varepsilon}\, d\Omega = \dfrac{|T|}{3}\sum_{i=1}^{3}\mathbf{D}(S_h\boldsymbol{\varepsilon})(Gi) : (S_h\boldsymbol{\varepsilon})(Gi)$,

where Gaussian points $G1$, $G2$ and $G3$ are given in **Fig. 6.2**. By (6.3.2) and (6.3.3), $(S_h\boldsymbol{\varepsilon})(Gi)$ is computed as follows:

$$\begin{aligned}
(S_h\boldsymbol{\varepsilon})(Gi) &= \frac{1}{2}(\hat{\boldsymbol{\varepsilon}}^{(j)} + \hat{\boldsymbol{\varepsilon}}^{(k)}) \\
&= \frac{1}{2}\left(\frac{1}{|T \cup T_j|}\int_{T\cup T_j}\boldsymbol{\varepsilon}\, d\Omega + \frac{1}{|T \cup T_k|}\int_{T\cup T_k}\boldsymbol{\varepsilon}\, d\Omega\right) \\
&= \frac{1}{2}\left(\frac{|T|\boldsymbol{\varepsilon}_T + |T_j|\boldsymbol{\varepsilon}_{T_j}}{|T| + |T_j|} + \frac{|T|\boldsymbol{\varepsilon}_T + |T_k|\boldsymbol{\varepsilon}_{T_k}}{|T| + |T_k|}\right),
\end{aligned}$$

where $\{i, j, k\} = \{1,2,3\}$.

On the other hand, let $T_{1,i}$ and $T_{2,i}$, $i = 1, 2, 3$ be the subregions in $\mathcal{T}_{1,h}$ and $\mathcal{T}_{2,h}$ that overlap with T; see **Fig. 6.1**(b).

Since $P_{2,h}P_{1,h}\boldsymbol{\varepsilon}$ is piecewise constant on $\mathcal{T}_{2,h}$, we have

$$\int_T \mathbf{D}P_{2,h}P_{1,h}\boldsymbol{\varepsilon} : P_{2,h}P_{1,h}\boldsymbol{\varepsilon}\, d\Omega = \sum_{i=1}^{3}\int_{T_{2,i}} \mathbf{D}P_{2,h}P_{1,h}\boldsymbol{\varepsilon} : P_{2,h}P_{1,h}\boldsymbol{\varepsilon}\, d\Omega,$$
$$= \frac{|T|}{3}\sum_{i=1}^{3}\mathbf{D}(P_{2,h}P_{1,h}\boldsymbol{\varepsilon})_{T_{2,i}} : (P_{2,h}P_{1,h}\boldsymbol{\varepsilon})_{T_{2,i}},$$

where $(P_{2,h}P_{1,h}\boldsymbol{\varepsilon})_{T_{2,i}}$ denotes the value of $P_{2,h}P_{1,h}\boldsymbol{\varepsilon}$ on $T_{2,i}$. Noting that $P_{1,h}$ and $P_{2,h}$ are piecewise averaging operators, it follows that

$$(P_{2,h}P_{1,h}\boldsymbol{\varepsilon})_{T_{2,i}} = \frac{1}{2}((P_{1,h}\boldsymbol{\varepsilon})_{T_{1,j}} + (P_{1,h}\boldsymbol{\varepsilon})_{T_{1,k}}), \qquad (\because |T_{1,j}\cap T_{2,i}| = |T_{1,k}\cap T_{2,i}|)$$
$$= \frac{1}{2}\left(\frac{|T|\boldsymbol{\varepsilon}_T + |T_j|\boldsymbol{\varepsilon}_{T_j}}{|T|+|T_j|} + \frac{|T|\boldsymbol{\varepsilon}_T + |T_k|\boldsymbol{\varepsilon}_{T_k}}{|T|+|T_k|}\right), \qquad (\because |T\cap T_{1,i}| : |T_i \cap T_{1,i}| = |T| : |T_i|)$$

where $\{i,j,k\} = \{1,2,3\}$ and $(P_{1,h}\boldsymbol{\varepsilon})_{T_{1,i}}$ is the value of $P_{1,h}\boldsymbol{\varepsilon}$ on $T_{1,i}$. This completes the proof.

As a direct consequence of Theorem 3.3, two bilinear forms (6.3.4) and (6.3.7) provide the same displacement solution $\bar{\mathbf{u}}_h \in V_h$ when they are adopted for (6.3.5). On the other hand, they have different distributions for smoothed strain fields; (6.3.7) has piecewise constant fields within an element while (6.3.4) has linear field. We close this section by presenting the uniqueness theorem for the solution of the SSE method.

Proposition 3.4. *The SSE method* (6.3.5) *has a unique solution.*
Proof. The coercivity of the bilinear form $\bar{a}(\cdot,\cdot)$ in (6.3.7) can be proven by the same argument as [75, Sect. 3.9]. Then the uniqueness of a solution of (6.3.5) is straightforward by Theorem 3.3 and the Lax-Milgram theorem [73, Theorem 2.7.7].

6.4. A variational principle for the strain-smoothed element method

In this section, we construct a variational principle for linear elasticity with respect to a single displacement field, two stress fields, and two strain fields. Then we show that the SSE method interpreted by the bilinear form in (6.3.7) is a Galerkin approximation of the constructed variational principle. It resembles the fact that S-FEM satisfies a modified Hellinger-Reissner variational principle [72, Sect. 4]. Throughout this section, let the index k denote either 1 or 2.

The starting point is the minimization problem (6.2.9). We set $W_k = W$. Consider two independent strain fields $\boldsymbol{\varepsilon}_1 \in W_1$ and $\boldsymbol{\varepsilon}_2 \in W_2$. It is obvious that (6.2.9) is equivalent to the following constrained minimization problem:

$$\min_{\mathbf{u}\in V, \boldsymbol{\varepsilon}_1\in W_1, \boldsymbol{\varepsilon}_2\in W_2}\left\{\frac{1}{2}\int_\Omega \mathbf{D}\boldsymbol{\varepsilon}_2 : \boldsymbol{\varepsilon}_2\, d\Omega - f(\mathbf{u})\right\} \quad \text{subject to } \boldsymbol{\varepsilon}_1 = \mathbf{B}\mathbf{u} \text{ and } \boldsymbol{\varepsilon}_1 = \boldsymbol{\varepsilon}_2. \tag{6.4.1}$$

In (6.4.1), we use the method of Lagrange multipliers in order to deal with the constraints $\boldsymbol{\varepsilon}_1 = \mathbf{Bu}$ and $\boldsymbol{\varepsilon}_1 = \boldsymbol{\varepsilon}_2$. Then we obtain the following saddle point problem:

$$\min_{\mathbf{u}\in V,\boldsymbol{\varepsilon}_1\in W_1,\boldsymbol{\varepsilon}_2\in W_2}\ \max_{\boldsymbol{\sigma}_1\in W_1,\boldsymbol{\sigma}_2\in W_2}\left\{\frac{1}{2}\int_\Omega \mathbf{D}\boldsymbol{\varepsilon}_2:\boldsymbol{\varepsilon}_2 d\Omega - f(\mathbf{u}) + \int_\Omega \boldsymbol{\sigma}_1:(\mathbf{Bu}-\boldsymbol{\varepsilon}_1)d\Omega + \int_\Omega \boldsymbol{\sigma}_2:(\boldsymbol{\varepsilon}_1-\boldsymbol{\varepsilon}_2)d\Omega\right\}, \tag{6.4.2}$$

where $\boldsymbol{\sigma}_1 \in W_1$ and $\boldsymbol{\sigma}_2 \in W_2$ are the Lagrange multipliers corresponding to the constraints $\boldsymbol{\varepsilon}_1 = \mathbf{Bu}$ and $\boldsymbol{\varepsilon}_1 = \boldsymbol{\varepsilon}_2$, respectively.

Equivalently, we have the following variational problem: find $(\mathbf{u},\boldsymbol{\varepsilon}_1,\boldsymbol{\varepsilon}_2,\boldsymbol{\sigma}_1,\boldsymbol{\sigma}_2)\in V\times W_1\times W_2\times W_1\times W_2$ such that

$$\int_\Omega \boldsymbol{\sigma}_1:\mathbf{Bv}\,d\Omega + \int_\Omega(-\boldsymbol{\sigma}_1+\boldsymbol{\sigma}_2):\boldsymbol{\delta}_1 d\Omega + \int_\Omega(\mathbf{D}\boldsymbol{\varepsilon}_2-\boldsymbol{\sigma}_2):\boldsymbol{\delta}_2\,d\Omega = f(\mathbf{v}),\ \ \forall\mathbf{v}\in V,\ \boldsymbol{\delta}_1\in W_1,\ \boldsymbol{\delta}_2\in W_2,$$
$$\int_\Omega \boldsymbol{\tau}_1:(\mathbf{Bu}-\boldsymbol{\varepsilon}_1)d\Omega + \int_\Omega \boldsymbol{\tau}_2:(\boldsymbol{\varepsilon}_1-\boldsymbol{\varepsilon}_2)d\Omega = 0,\ \ \forall\boldsymbol{\tau}_1\in W_1,\ \boldsymbol{\tau}_2\in W_2. \tag{6.4.3}$$

The existence and the uniqueness of a solution of the variational principle (6.4.3) is summarized in Proposition 4.1. We postpone the proof of Proposition 4.1 until Sect. 6.5; a more general statement will be given in Proposition 5.1.

Proposition 4.1. *The variational problem* (*6.4.3*) *has a unique solution* $(\mathbf{u},\boldsymbol{\varepsilon}_1,\boldsymbol{\varepsilon}_2,\boldsymbol{\sigma}_1,\boldsymbol{\sigma}_2)\in V\times W_1\times W_2\times W_1\times W_2$. *Moreover,* $\mathbf{u}$ *solves (6.2.8) and the following relations hold:*
$\boldsymbol{\varepsilon}_1 = \boldsymbol{\varepsilon}_2 = \mathbf{Bu}$, $\boldsymbol{\sigma}_1 = \boldsymbol{\sigma}_2 = \mathbf{DBu}$.

Remark 4.2. From Proposition 4.1, we observe that the Lagrange multipliers $\boldsymbol{\sigma}_1$ and $\boldsymbol{\sigma}_2$ introduced in (6.4.2) in fact play a role of the strain field.

Remark 4.3. Elimination of two variables $\boldsymbol{\varepsilon}_2$ and $\boldsymbol{\sigma}_2$ in (6.4.2) yields

$$\min_{\mathbf{u}\in V,\boldsymbol{\varepsilon}_1\in W_1}\ \max_{\boldsymbol{\sigma}_1\in W_1}\left\{\frac{1}{2}\int_\Omega \mathbf{D}\boldsymbol{\varepsilon}_1:\boldsymbol{\varepsilon}_1 d\Omega - f(\mathbf{u}) + \int_\Omega \boldsymbol{\sigma}_1:(\mathbf{Bu}-\boldsymbol{\varepsilon}_1)d\Omega\right\},$$

which is the Hu-Washizu variational principle. In this sense, we can say that (6.4.3) generalizes the Hu–Washizu variational principle.

6.4.1. Galerkin approximation

Now, we consider a Galerkin approximation of (6.4.3) made by replacing the spaces V and W_k by their finite-dimensional subspaces $V_h \in V$ and $W_{k,h} \in W_k$, respectively (see Sect. 6.3 for the definitions of V_h and $W_{k,h}$): find $(\overline{\mathbf{u}}_h,\boldsymbol{\varepsilon}_{1,h},\boldsymbol{\varepsilon}_{2,h},\boldsymbol{\sigma}_{1,h},\boldsymbol{\sigma}_{2,h})\in V_h\times W_{1,h}\times W_{2,h}\times W_{1,h}\times W_{2,h}$ such that

$$\int_\Omega \boldsymbol{\sigma}_{1,h} : \mathbf{B}\mathbf{v}\, d\Omega + \int_\Omega (-\boldsymbol{\sigma}_{1,h} + \boldsymbol{\sigma}_{2,h}) : \boldsymbol{\delta}_1\, d\Omega + \int_\Omega (\mathbf{D}\boldsymbol{\varepsilon}_{2,h} - \boldsymbol{\sigma}_{2,h}) : \boldsymbol{\delta}_2\, d\Omega = f(\mathbf{v}),$$
$$\forall \mathbf{v} \in V_h,\ \ \boldsymbol{\delta}_1 \in W_{1,h},\ \ \boldsymbol{\delta}_2 \in W_{2,h}, \tag{6.4.4a}$$

$$\int_\Omega \boldsymbol{\tau}_1 : (\mathbf{B}\bar{\mathbf{u}}_h - \boldsymbol{\varepsilon}_{1,h})\, d\Omega + \int_\Omega \boldsymbol{\tau}_2 : (\boldsymbol{\varepsilon}_{1,h} - \boldsymbol{\varepsilon}_{2,h})\, d\Omega = 0,\ \ \forall \boldsymbol{\tau}_1 \in W_{1,h},\ \ \boldsymbol{\tau}_2 \in W_{2,h}. \tag{6.4.4b}$$

We take $\mathbf{v} = \mathbf{0}$ and $\boldsymbol{\delta}_2 = \mathbf{0}$ in (6.4.4a). Then we have

$$\int_\Omega (-\boldsymbol{\sigma}_{1,h} + \boldsymbol{\sigma}_{2,h}) : \boldsymbol{\delta}_1\, d\Omega = 0,\ \ \forall \boldsymbol{\delta}_1 \in W_{1,h},$$

which implies that $\boldsymbol{\sigma}_{1,h}$ is the $(L^2(\Omega))^3$-orthogonal projection of $\boldsymbol{\sigma}_{2,h}$ onto $W_{1,h}$. It follows by Lemma 3.2 that $\boldsymbol{\sigma}_{1,h} = P_{1,h}\boldsymbol{\sigma}_{2,h}$.

Similarly, it is straightforward to verify that

$$\boldsymbol{\sigma}_{2,h} = \mathbf{D}\boldsymbol{\varepsilon}_{2,h}$$

from (6.4.4a) and that

$$\boldsymbol{\varepsilon}_{1,h} = P_{1,h}(\mathbf{B}\bar{\mathbf{u}}_h),\ \ \boldsymbol{\varepsilon}_{2,h} = P_{2,h}\boldsymbol{\varepsilon}_{1,h}$$

from (6.4.4b).

Using the above relations and Lemmas 3.1 and 3.2, we readily get

$$\boldsymbol{\sigma}_{1,h} = P_{1,h}\mathbf{D}P_{2,h}P_{1,h}(\mathbf{B}\bar{\mathbf{u}}_h) = P_{1,h}P_{2,h}(\mathbf{D}P_{2,h}P_{1,h}(\mathbf{B}\bar{\mathbf{u}}_h)).$$

Substituting $\boldsymbol{\delta}_1 = \mathbf{0}$ and $\boldsymbol{\delta}_2 = \mathbf{0}$ in (6.4.4a) yields

$$\int_\Omega \mathbf{D}P_{2,h}P_{1,h}(\mathbf{B}\bar{\mathbf{u}}_h) : P_{2,h}P_{1,h}(\mathbf{B}\mathbf{v})\, d\Omega = f(\mathbf{v}),\ \ \forall \mathbf{v} \in V_h,$$

which is equivalent to (6.3.5) with the bilinear form $\bar{a}(\cdot,\cdot)$ given in (6.3.7). Therefore, the SSE method can be derived from the variational principle (6.4.3).

We summarize the above discussion in the following theorem. Note that the uniqueness of the solution of the SSE method was presented in Proposition 3.4.

Theorem 4.3. *The variational problem* (6.4.4) *has a unique solution* $(\bar{\mathbf{u}}_h, \boldsymbol{\varepsilon}_{1,h}, \boldsymbol{\varepsilon}_{2,h}\boldsymbol{\sigma}_{1,h}, \boldsymbol{\sigma}_{2,h}) \in V_h \times W_{1,h} \times W_{2,h} \times W_{1,h} \times W_{2,h}$ *which satisfies that*

$$\boldsymbol{\varepsilon}_{1,h} = P_{1,h}(\mathbf{B}\bar{\mathbf{u}}_h),\ \ \boldsymbol{\varepsilon}_{2,h} = P_{2,h}P_{1,h}(\mathbf{B}\bar{\mathbf{u}}_h),\ \ \boldsymbol{\sigma}_{1,h} = P_{1,h}P_{2,h}(\mathbf{D}P_{2,h}P_{1,h}(\mathbf{B}\bar{\mathbf{u}}_h)),\ \ \boldsymbol{\sigma}_{2,h} = \mathbf{D}P_{2,h}P_{1,h}(\mathbf{B}\bar{\mathbf{u}}_h),$$

and that $\bar{\mathbf{u}}_h$ *is a unique solution of* (6.3.5) *with the bilinear form* $\bar{a}(\cdot,\cdot)$ *given in* (6.3.7).

6.5. **Convergence analysis**

In this section, we present a convergence theory for the SSE method based on the variational formulation (6.4.3). For the sake of presenting a unified convergence analysis for the standard FEM, S-FEM, and SSE method, the convergence theory established in this section is built upon an abstract mixed problem which generalizes (6.4.3).

Let X, Y be two Hilbert spaces equipped with inner products $\langle\cdot,\cdot\rangle_X$, $\langle\cdot,\cdot\rangle_Y$ and their induced norms $|||\cdot|||_X$, $|||\cdot|||_Y$, respectively. We set $\Pi = X\times Y\times Y$ and $\Delta = Y\times Y$. Let $D:Y\to Y$ be a continuous and symmetric positive definite linear operator so that

$\|\varepsilon\|_Y = \langle D\varepsilon,\varepsilon\rangle_Y^{1/2}$, $\varepsilon\in Y$,

becomes a norm on Y.

In this case, the dual norm $\|\cdot\|_{Y^*}$ of $\|\cdot\|_Y$ is given as follows:

$$\|\sigma\|_{Y^*} = \sup_{\delta\in Y\setminus\{0\}} \frac{\langle\sigma,\delta\rangle_Y}{\|\delta\|_Y} = \langle\sigma, D^{-1}\sigma\rangle_Y^{1/2},\ \ \sigma\in Y .$$

We additionally assume that there is a continuous linear operator $B:X\to Y$ such that

$\|u\|_X = \|Bu\|_Y$, $u\in X$

becomes a norm on X.

The following norms on the spaces Π and Δ are defined:

$\|U\|_\Pi^2 = \|u\|_X^2 + \|\varepsilon_1\|_Y^2 + \|\varepsilon_2\|_Y^2$, $U=(u,\varepsilon_1,\varepsilon_2)\in\Pi$,

$\|P\|_\Delta^2 = \|\varepsilon_1\|_Y^2 + \|\varepsilon_2\|_Y^2$, $P=(\varepsilon_1,\varepsilon_2)\in\Delta$,

$\|Q\|_{\Delta^*}^2 = \|\sigma_1\|_{Y^*}^2 + \|\sigma_2\|_{Y^*}^2$, $Q=(\sigma_1,\sigma_2)\in\Delta$.

We also define a seminorm $|\cdot|_\Pi$ on Π as follows:

$|U|_\Pi = \|\varepsilon_2\|_Y$, $U=(u,\varepsilon_1,\varepsilon_2)\in\Pi$.

Let $\mathfrak{D}:\Pi\to\Delta$ be a linear operator given by

$\mathfrak{D}U = (DBu-\varepsilon_1, \varepsilon_1-\varepsilon_2)$, $U=(u,\varepsilon_1,\varepsilon_2)\in\Pi$.

In terms of the operator $\mathfrak{D}$, we define a bilinear form $B(\cdot,\cdot)::\Pi\times\Delta\to\mathbb{R}$ as follows:

$B(V,Q) = \langle\mathfrak{D}V,Q\rangle_\Delta = \langle\tau_1, Bv-\delta_1\rangle_Y + \langle\tau_2,\delta_1-\delta_2\rangle_Y$, $V=(v,\delta_1,\delta_2)\in\Pi$, $Q=(\tau_1,\tau_2)\in\Delta$.

It is straightforward to check that the kernel Z of $B(\cdot,\Delta)$ defined by

$$Z=\{V\in\Pi: B(V,Q)=0,\ Q\in\Delta\}, \tag{6.5.1}$$

is characterized as follows:

$$Z=\{(v,Bv,Bv)\in\Pi:\ v\in X\}. \tag{6.5.2}$$

The seminorm $|\cdot|_\Pi$ is positive definite on Z since

$$|U|_\Pi^2=\|Bu\|_Y^2=\frac{1}{3}\|U\|_\Pi^2,\ \ U=U=(u,Bu,Bu)\in Z. \tag{6.5.3}$$

In other words, $|\cdot|_\Pi$ becomes a norm on Z.

If we define a bilinear form $A(\cdot,\cdot):\Pi\times\Pi\to\mathbb{R}$ by

$$A(U,V)=\langle D\varepsilon_2,\delta_2\rangle_Y,\ \ U=(u,\varepsilon_1,\varepsilon_2),\ \ V=(v,\delta_1,\delta_2)\in\Pi,$$

then it is continuous and coercive with respect to $|\cdot|_\Pi$ since

$$A(U,V)=\langle D\varepsilon_2,\delta_2\rangle_Y\le\|\varepsilon_2\|_Y\|\delta_2\|_Y=|U|_\Pi|V|_\Pi \tag{6.5.4}$$

and

$$A(U,U)=\|\varepsilon_2\|_Y^2=|U|_\Pi^2 \tag{6.5.5}$$

for any $U=(u,\varepsilon_1,\varepsilon_2)$, $V=(v,\delta_1,\delta_2)\in\Pi$.

Now, we are ready to state the following abstract variational problem to find $U\in\Pi$ and $P\in\Delta$ such that

$$A(U,V)+B(V,P)=F(V),\ \ \forall V\in\Pi, \tag{6.5.6a}$$

$$B(U,Q)=0,\qquad \forall Q\in\Delta, \tag{6.5.6b}$$

where $F\in\Pi^*$ satisfies

$$F(V)=f(v),\ \ V=(v,\delta_1,\delta_2)\in\Pi,$$

for some $f\in X^*$. The existence and uniqueness of a solution of (6.5.6) can be shown as follows.

Proposition 5.1. *The variational problem* (6.5.6) *has a unique solution* $(U,P)\in\Pi\times\Delta$. *Moreover, the unique solution* (U,P) *is characterized by*

$$U=(u,Bu,Bu),\ \ P=(DBu,DBu),$$

where $u\in X$ *is a unique solution of the variational problem*

$$\langle DBu,Bv\rangle_Y=f(v),\ \ \forall v\in X. \tag{6.5.7}$$

Proof. Note that the existence and uniqueness of a solution of (6.5.7) are direct consequences of the Lax-Milgram theorem [73, Theorem 2.7.7]. The equation (6.5.6b) implies that $U\in Z$. By (6.5.6a), U can be determined by the following variational problem: find $U\in Z$ such that

$$A(U,V)+F(V)\ ,\quad \forall V\in Z\ . \tag{6.5.8}$$

Since $|\cdot|_\Pi$ is a norm on Z (see (6.5.3)), the existence and uniqueness of U are guaranteed by (6.5.4), (6.5.5), and the Lax-Milgram theorem applied to (6.5.8). By (6.5.2), we have $U=(u,Bu,Bu)$ for some $u\in X$. Writing $V=(v,Bv,Bv)$ for $v\in X$, the problem (6.5.8) reduces to (6.5.7). Therefore, u is a unique solution of (6.5.7).

Next, we characterize the dual solution P. We write $V=(v,\delta_1,\delta_2)$ and $P=(\sigma_1,\sigma_2)$ in (6.5.6a). Substituting $v=0$ and $\delta_2=0$ in (6.5.6a) yields

$$\langle \sigma_1-\sigma_2,\delta_1\rangle_Y=0\ ,\quad \forall \delta_1\in Y\ ,$$

which is equivalent to $\sigma_1=\sigma_2$. On the other hand, by substituting $U=(u,Bu,Bu)$, $v=0$, and $\delta_1=0$ in (6.5.6a), we have

$$\langle DBu-\sigma_2,\delta_2\rangle_Y=0\ ,\quad \forall \delta_2\in Y\ .$$

That is, we get $\sigma_2=DBu$. Therefore, we conclude that $\sigma_1=\sigma_2=DBu$.

The abstract problem (6.5.6) generalizes several important elliptic partial differential equations. If we set

$$X=\{u\in H^1(\Omega):u=0\text{ on }\Gamma_D\}\ ,\quad Y=L^2(\Omega)\ ,\quad D=I\ ,\quad B=\nabla$$

in (6.5.6), then (6.5.7) becomes

$$\int_\Omega \nabla u\cdot\nabla v\,d\Omega=f(v)\ ,\quad \forall v\in X\ ,$$

which is the weak formulation for the Poisson's equation with a mixed boundary condition. On the other hand, if we set

$$X=V\ ,\quad Y=W\ ,\quad D=\mathbf{D}\ ,\quad B=\mathbf{B}\ , \tag{6.5.9}$$

where V, W, $\mathbf{D}$, and $\mathbf{B}$ were defined in Sect. 6.2, then (6.5.6) and (6.5.7) reduce to (6.4.3) and (6.2.8), respectively. Therefore, linear elasticity is an instance of (6.5.6). In this sense, Proposition 5.1 generalizes Proposition 4.1.

Now, we present a Galerkin approximation of (6.5.6) which generalizes (6.4.4). Let $X_h\subset X$, $Y_{1,h}\subset Y$, and $Y_{2,h}\subset Y$. For $\Pi_h=X_h\times Y_{1,h}\times Y_{2,h}$ and $\Delta_h=Y_{1,h}\times Y_{2,h}$, we consider a variational problem to find $U_h\in\Pi_h$ and $P_h\in\Delta_h$ such that

$$A(U_h,V)+B(V,P_h)=F(V)\ ,\quad \forall V\in\Pi_h\ , \tag{6.5.10a}$$

$$B(U_h,Q)=0\ ,\qquad \forall Q\in\Delta_h\ . \tag{6.5.10b}$$

Similarly to (6.5.1), we define

$$Z_h=\{V\in\Pi_h:B(V,Q)=0,\ Q\in\Delta_h\}\ . \tag{6.5.11}$$

Note that $Z_h\not\subset Z$ in general.

We state an assumption on Z_h which is necessary to obtain a bound for the error $U-U_h$.

Assumption 5.2. The seminorm $|\cdot|_\Pi$ is positive definite on $Z \cup Z_h$, i.e., there exists a positive constant α such that

$|U|_\Pi \geq \alpha \|U\|_\Pi$, $U \in Z \cup Z_h$.

Thanks to (6.5.3), it is enough to prove the positive definiteness of $|\cdot|_\Pi$ on Z_h in order to verify Assumption 5.2 in applications. Under Assumption 5.2, the primal solution U_h of (6.5.10) is uniquely determined since it solves

$$A(U_h, V) = F(V), \quad \forall V \in Z_h. \tag{6.5.12}$$

Moreover, one can prove the following continuity condition of the bilinear form $B(\cdot,\cdot)$ with respect to $|\cdot|_\Pi$.

Lemma 5.3. *Suppose that Assumption 5.2 holds. Then there exist a positive constant* C_B *such that*

$B(V,Q) \leq C_B |V|_\Pi \|Q\|_{\Delta^*}$, $V \in \Pi$, $P \in \Delta$.

Proof. First, we show that the operator $\mathfrak{D}$ is bounded. For any $U = (u, \varepsilon_1, \varepsilon_2) \in \Pi$, it follows that

$$\begin{aligned} \|\mathfrak{D}U\|_\Delta^2 &= \|Bu - \varepsilon_1\|_Y^2 + \|\varepsilon_1 - \varepsilon_2\|_Y^2 \\ &\leq 2(\|Bu\|_Y^2 + \|\varepsilon_1\|_Y^2) + 2(\|\varepsilon_1\|_Y^2 + \|\varepsilon_2\|_Y^2) \\ &= 2\|u\|_X^2 + 4\|\varepsilon_1\|_Y^2 + 2\|\varepsilon_2\|_Y^2 \\ &\leq 4\|U\|_\Pi^2. \end{aligned} \tag{6.5.13}$$

Using (6.5.13), one can obtain the desired result with $C_B = 2/\alpha$ as follows: for $V \in \Pi$ and $Q \in \Delta$, we have

$$\begin{aligned} B(V,Q) &= \langle \mathfrak{D}V, Q \rangle_\Delta \\ &\leq \|\mathfrak{D}Vv\|_\Delta \|Q\|_{\Delta^*} \\ &\overset{(5.13)}{\leq} 2\|V\|_\Pi \|Q\|_{\Delta^*} \\ &\leq \frac{2}{\alpha} |V|_\Pi \|Q\|_{\Delta^*}, \end{aligned}$$

where we used Assumption 5.2 in the last inequality.

Motivated by [73, Theorem 12.3.7], we have the following result on a relation between primal solutions of the variational problem (6.5.6) and its Galerkin approximation (6.5.10).

Theorem 5.4. *Suppose that Assumption 5.2 holds. Let* $(U,P) \in \Pi \times \Delta$ *be a unique solution of (6.5.6), and let* $U_h \in \Pi_h$ *be a unique primal solution of (6.5.10). Then we have*

$$\left|U-U_h\right|_\Pi \le 2\inf_{V\in Z_h}\left|U-V\right|_\Pi + C_B \inf_{Q\in\Delta_h}\left\|P-Q\right\|_{\Delta^*},$$

where C_B *was defined in Lemma 5.3.*

Proof. Note that U and U_h solve (6.5.8) and (6.5.12), respectively. Thanks to (6.5.4), (6.5.5), and Assumption 5.2, one can apply Theorem Appendix A.1 to obtain

$$\left|U-U_h\right|_\Pi \le 2\inf_{V\in Z_h}\left|U-V\right|_\Pi + \sup_{W\in Z_h\setminus\{0\}} \frac{\left|A(U-U_h,W)\right|}{\left|W\right|_\Pi}. \tag{6.5.14}$$

On the other hand, for any $W\in Z_h$ and $Q\in\Delta_h$, we have

$$\begin{aligned}\left|A(U-U_h,W)\right| &\overset{(5.12)}{=} \left|A(U,W)-F(W)\right| \\ &\overset{(5.6a)}{=} \left|B(W,P)\right| \\ &\overset{(5.11)}{=} \left|B(W,P-Q)\right| \\ &\le C_B\left|W\right|_\Pi \left\|P-Q\right\|_{\Delta^*},\end{aligned} \tag{6.5.15}$$

where the last inequality is due to Lemma 5.3. Combining (6.5.14) and (6.5.15) yields the desired result.

Like that linear elasticity is an instance of the continuous problem (6.5.6), various FEMs such as the standard FEM, S-FEM, and SSE method for linear elasticity can be written in the form of (6.5.10). We present how the convergence results of those methods can be obtained in a unified fashion from Theorem 5.4. In what follows, we assume the setting (6.5.9). Then the norms $\|\cdot\|_Y$ and $\|\cdot\|_{Y^*}$ become the energy norms for strain and stress fields, respectively, i.e.,

$$\|\boldsymbol{\varepsilon}\|_Y^2 = \int_\Omega \mathbf{D}\boldsymbol{\varepsilon}:\boldsymbol{\varepsilon}\,d\Omega,\ \ \boldsymbol{\varepsilon}\in W,$$

and

$$\|\boldsymbol{\sigma}\|_{Y^*}^2 = \int_\Omega \boldsymbol{\sigma}:\mathbf{D}^{-1}\boldsymbol{\sigma}\,d\Omega,\ \ \boldsymbol{\sigma}\in W.$$

6.5.1. Standard finite element method

First, we set $X_h = V_h$ and $Y_{1,h} = Y_{2,h} = W_h$ in (6.5.10), where the spaces V_h and W_h were defined in Sect. 6.3. Since the meshes associated to V_h and W_h agree, it satisfies that $\mathbf{Bv}\in W_h$ for all $\mathbf{v}\in V_h$. Accordingly, the set Z_h defined in (6.5.11) is characterized by

$$Z_h = \left\{(\mathbf{v},\mathbf{Bv},\mathbf{Bv})\in V_h\times W_h\times W_h : \mathbf{v}\in V_h\right\}.$$

In addition, the variational problem (6.5.12) reduces to the standard FEM formulation

$$\int_\Omega \mathbf{D}\boldsymbol{\varepsilon}[\mathbf{u}_h]:\boldsymbol{\varepsilon}[\mathbf{v}]\,d\Omega = f(\mathbf{v}),\ \ \forall\mathbf{v}\in V_h, \tag{6.5.16}$$

where $\boldsymbol{\varepsilon}[\mathbf{v}] = \mathbf{Bv}$.

For $\mathbf{V} = (\mathbf{v}, \mathbf{Bv}, \mathbf{Bv}) \in Z_h$, one can easily verify that

$\|\mathbf{V}\|_\Pi^2 = 3\|\boldsymbol{\varepsilon}[\mathbf{v}]\|_Y^2 = 3|\mathbf{V}|_\Pi^2$,

which implies that Assumption 5.2 holds. Therefore, one can obtain an error estimate for (6.5.16) as a corollary of Theorem 5.4 as follows.

Corollary 5.5. *Let* $\mathbf{u} \in V$ *and* $\mathbf{u}_h \in V_h$ *solve* (6.2.8) *and* (6.5.16)*, respectively. Then we have*

$\|\boldsymbol{\varepsilon}[\mathbf{u}] - \boldsymbol{\varepsilon}[\mathbf{u}_h]\|_Y \le 2\inf_{\mathbf{v}\in V_h}\|\boldsymbol{\varepsilon}[\mathbf{u}] - \boldsymbol{\varepsilon}[\mathbf{v}]\|_Y + 2C_B \inf_{\boldsymbol{\tau}\in W_h}\|\boldsymbol{\sigma}[\mathbf{u}] - \boldsymbol{\tau}\|_{Y^*}$,

where $\boldsymbol{\varepsilon}[\mathbf{v}] = \mathbf{Bv}$, $\boldsymbol{\sigma}[\mathbf{v}] = \mathbf{DBv}$ *for* $\mathbf{v} \in V_h$ *and* C_B *was defined in Assumption 5.2.*

6.5.2. Edge-based smoothed finite element method

Next, let $X_h = V_h$, $Y_{1,h} = Y_{2,h} = W_{1,h}$ in (6.5.10), where the spaces $W_{1,h}$ was defined in Sect. 6.3.1. By a similar argument as Sect. 6.4.1, we get

$Z_h = \{(\mathbf{v}, P_{1,h}(\mathbf{Bv}), P_{1,h}(\mathbf{Bv})) \in V_h \times W_{1,h} \times W_{1,h} : \mathbf{v} \in V_h\}$.

In this case, the variational problem (6.5.12) becomes the following: find $\hat{\mathbf{u}}_h \in V_h$ such that

$$\int_\Omega \mathbf{D}\hat{\boldsymbol{\varepsilon}}[\hat{\mathbf{u}}_h] : \hat{\boldsymbol{\varepsilon}}[\mathbf{v}]\, d\Omega = f(\mathbf{v}) , \quad \forall \mathbf{v} \in V_h , \tag{6.5.17}$$

where $\hat{\boldsymbol{\varepsilon}}[\mathbf{v}] = P_{1,h}(\mathbf{Bv})$. It was shown in [72] that (6.5.17) is a formulation for the edge-based S-FEM [10].

In order to verify Assumption 5.2 for (6.5.17), we first observe that

$\|\mathbf{V}\|_\Pi^2 = \|\boldsymbol{\varepsilon}[\mathbf{v}]\|_Y^2 + 2\|\hat{\boldsymbol{\varepsilon}}[\mathbf{v}]\|_Y^2$, $|\mathbf{V}|_\Pi^2 = \|\hat{\boldsymbol{\varepsilon}}[\mathbf{v}]\|_Y^2$

for $\mathbf{V} = (\mathbf{v}, P_{1,h}(\mathbf{Bv}), P_{1,h}(\mathbf{Bv})) \in Z_h$.

Since it was shown in [75, Sect. 3.9] that there exists a positive constant C such that

$\|\hat{\boldsymbol{\varepsilon}}[\mathbf{v}]\|_Y \ge C\|\boldsymbol{\varepsilon}[\mathbf{v}]\|_Y$, $\mathbf{v} \in V_h$,

it is clear that Assumption 5.2 holds.

The following corollary summarizes the convergence property of (6.5.17) (cf. [72, Theorem~1]).

Corollary 5.6. *Let* $\mathbf{u} \in V$ *and* $\hat{\mathbf{u}}_h \in V_h$ *solve* (6.2.8) *and* (6.5.17)*, respectively. Then we have*

$\|\boldsymbol{\varepsilon}[\mathbf{u}] - \hat{\boldsymbol{\varepsilon}}[\hat{\mathbf{u}}_h]\|_Y \le 2\inf_{\mathbf{v}\in V_h}\|\boldsymbol{\varepsilon}[\mathbf{u}] - \hat{\boldsymbol{\varepsilon}}[\mathbf{v}]\|_Y + 2C_B \inf_{\hat{\boldsymbol{\tau}}\in W_{1,h}}\|\boldsymbol{\sigma}[\mathbf{u}] - \hat{\boldsymbol{\tau}}\|_{Y^*}$,

where $\boldsymbol{\varepsilon}[\mathbf{v}] = \mathbf{Bv}$, $\boldsymbol{\sigma}[\mathbf{v}] = \mathbf{DBv}$, $\hat{\boldsymbol{\varepsilon}}[\mathbf{v}] = P_{1,h}(\mathbf{Bv})$ *for* $\mathbf{v} \in V_h$ *, and* C_B *was defined in Assumption 5.2.*

6.5.3. Strain-smoothed finite element method

In order to derive the SSE (6.3.5) from the abstract problem (6.5.10), we set $X_h = V_h$, $Y_{1,h} = W_{1,h}$, and $Y_{2,h} = W_{2,h}$, where the space $W_{2,h}$ was defined in Sect. 6.3.1. Then the set Z_h is characterized by

$Z_h = \left\{ (\mathbf{v}, P_{1,h}(\mathbf{Bv}), P_{2,h}P_{1,h}(\mathbf{Bv})) \in V_h \times W_{1,h} \times W_{2,h} : \mathbf{v} \in V_h \right\}$,

and (6.5.12) is reduced to (6.3.5): find $\bar{\mathbf{u}}_h \in V_h$ such that

$$\int_\Omega \mathbf{D}\bar{\boldsymbol{\varepsilon}}[\bar{\mathbf{u}}_h] : \bar{\boldsymbol{\varepsilon}}[\mathbf{v}] d\Omega = f(\mathbf{v}), \quad \forall \mathbf{v} \in V_h, \tag{6.5.18}$$

where $\bar{\boldsymbol{\varepsilon}}[\mathbf{v}] = P_{2,h}P_{1,h}(\mathbf{Bv})$.

Similarly to the case of S-FEM, we have

$\|\mathbf{V}\|_\Pi^2 = \|\boldsymbol{\varepsilon}[\mathbf{v}]\|_Y^2 + \|\hat{\boldsymbol{\varepsilon}}[\mathbf{v}]\|_Y^2 + \|\bar{\boldsymbol{\varepsilon}}[\mathbf{v}]\|_Y^2$, $|\mathbf{V}|_\Pi^2 = \|\bar{\boldsymbol{\varepsilon}}[\mathbf{v}]\|_Y^2$

for $\mathbf{V} = (\mathbf{v}, P_{1,h}(\mathbf{Bv}), P_{2,h}P_{1,h}(\mathbf{Bv})) \in Z_h$.

With the same argument as [75, Sect. 3.9], one can show without major difficulty that there exists a positive constant C such that

$\|\bar{\boldsymbol{\varepsilon}}[\mathbf{v}]\|_Y \geq C \|\hat{\boldsymbol{\varepsilon}}[\mathbf{v}]\|_Y$, $\mathbf{v} \in V_h$.

Hence, Assumption 5.2 holds for (6.5.18).

Finally, we have the following convergence theorem for the SSE method.

Corollary 5.8. *Let* $\mathbf{u} \in V$ *and* $\bar{\mathbf{u}}_h \in V_h$ *solve* (6.2.8) *and* (6.5.18)*, respectively. Then we have*

$\|\boldsymbol{\varepsilon}[\mathbf{u}] - \bar{\boldsymbol{\varepsilon}}[\bar{\mathbf{u}}_h]\|_Y \leq 2 \inf_{\mathbf{v} \in V_h} \|\boldsymbol{\varepsilon}[\mathbf{u}] - \bar{\boldsymbol{\varepsilon}}[\mathbf{v}]\|_Y + C_B \inf_{\hat{\boldsymbol{\tau}} \in W_{1,h}} \|\boldsymbol{\sigma}[\mathbf{u}] - \hat{\boldsymbol{\tau}}\|_{Y^*} + C_B \inf_{\bar{\boldsymbol{\tau}} \in W_{2,h}} \|\boldsymbol{\sigma}[\mathbf{u}] - \bar{\boldsymbol{\tau}}\|_{Y^*}$,

where $\boldsymbol{\varepsilon}[\mathbf{v}] = \mathbf{Bv}$, $\boldsymbol{\sigma}[\mathbf{v}] = \mathbf{DBv}$, $\hat{\boldsymbol{\varepsilon}}[\mathbf{v}] = P_{1,h}(\mathbf{Bv})$, $\bar{\boldsymbol{\varepsilon}}[\mathbf{v}] = P_{2,h}P_{1,h}(\mathbf{Bv})$ *for* $\mathbf{v} \in V_h$, *and* C_B *was defined in Assumption 5.2.*

Appendix A. Abstract convergence theory of nonconforming finite element methods

In this appendix, we present an abstract convergence theory of nonconforming Galerkin methods. Let H be a Hilbert space and let V, V_h be subspaces of H such that $V_h \not\subset V$. Assume that $|\cdot|_H$ is a seminorm on H such that $|\cdot|_H$ is positive definite on $V \cup V_h$, i.e.,

$|u|_H > 0$, $u \in (V \cup V_h) \setminus \{0\}$.

Let $a(\cdot,\cdot): H \times H \to \mathbb{R}$ be a bilinear form on H which is continuous and coercive with respect to $|\cdot|_H$, i.e., there exist two positive constants C and α satisfying

$$a(u,v) \le C|u|_H |v|_H, \tag{A.1}$$

$$a(u,u) \ge \alpha |u|_H^2 \tag{A.2}$$

for $u, v \in H$.

In Theorem Appendix A.1, we present an error estimate for the variational problem

$$a(u,v) = f(v), \quad v \in V \tag{A.3}$$

with respect to its nonconforming Galerkin approximation

$$a(u_h,v) = f(v), \quad v \in V_h, \qquad \text{(A.4}$$

where $f \in H^*$.

Theorem Appendix A.1. *Let* $u \in V$ *and* $u_h \in V_h$ *solve* (A.3) *and* (A.4)*, respectively. Then we have*

$$|u-u_h|_H \le \left(1+\frac{C}{\alpha}\right)\inf_{v\in V_h}|u-v|_H + \frac{1}{\alpha}\sup_{w\in V_h\setminus\{0\}}\frac{|a(u-u_h,w)|}{|w|_H}.$$

Proof. One can easily obtain the desired result by following the argument in [73, Lemma 10.1.1].

Note that Theorem Appendix A.1 is written in terms of seminorm $|\cdot|_H$ while the existing standard results (see, e.g., [73,76]) are written in terms of norm. In this sense, Theorem Appendix A.1 is a generalization of the standard results.

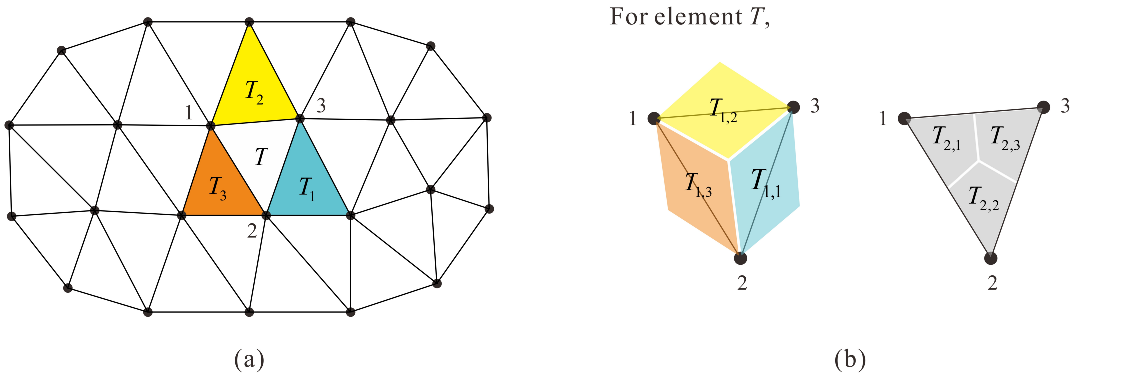

Fig. 6.1. (a) Three neighboring elements T_1, T_2 and T_3 of an interior element $T \in \mathcal{T}_h$. (b) $T_{1,i}$ and $T_{2,i}$, $i = 1, 2, 3$ are the subregions in $\mathcal{T}_{1,h}$ and $\mathcal{T}_{2,h}$ that overlap with T, respectively.

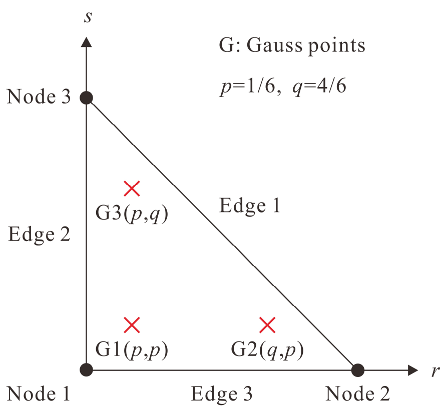

Fig. 6.2. Coordinate systems for the reference 3-node triangular element. Three Gauss integration points of the element are depicted by G1, G2, and G3.

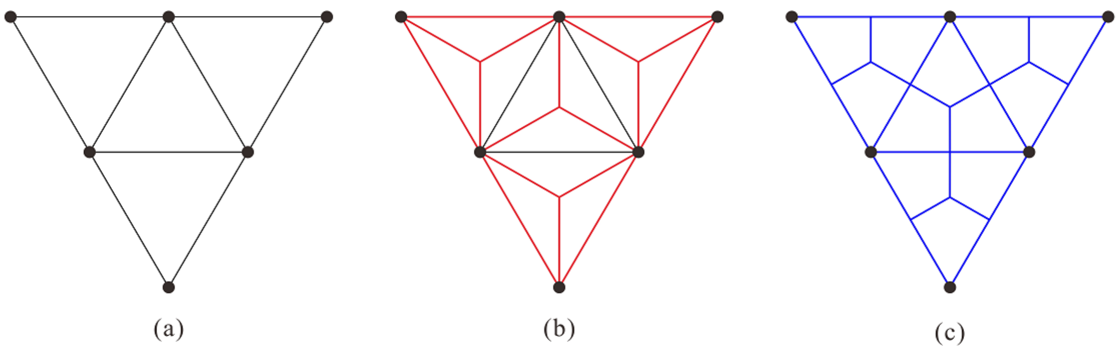

Fig. 6.3. Three subdivisions of the domain Ω: (a) $\mathcal{T}_h$, (b) $\mathcal{T}_{1,h}$, and (c) $\mathcal{T}_{2,h}$.

Chapter 7. Conclusions

The objectives in this work were to develop a new finite element method (FEM) to improve low-order solid and shell finite elements. The FEM has been widely used for solving problems in various engineering fields over the past several decades. The low-order finite elements are very attractive due to their simplicity and efficiency. They have high modeling capabilities and are particularly preferred for large deformation analysis requiring automatic remeshing. Also, they often provide a relatively easy way to solve complicated engineering problems such as contact analysis. However, in general, the predictive capability of low-order elements is not good enough to be used in engineering practice. Further development of low-order finite elements with improved accuracy is still required while maintaining its advantages.

In Chapter 2, a new strain smoothing method (the strain-smoothed element method) was proposed for 3-node triangular and 4-node tetrahedral finite elements. To construct a smoothed strain field of a target element, the strains of neighboring elements were utilized. The smoothed strain values were directly assigned to the Gauss integration points of the element. Consequently, strain-smoothed triangular and tetrahedral elements were developed. Unlike with previous S-FEM methods, special smoothing domains are not created in the strain-smoothed element (SSE) method. That is, the domain discretization is the same as with the standard finite element method. The strain-smoothed triangular and tetrahedral elements give linear strain fields within elements. The proposed elements passed patch, isotropy, and zero energy mode tests, and showed improved convergence behavior, when compared to standard and edge-based smoothed elements in 2D, and the standard, face-based and edge-based smoothed elements in 3D solid mechanics problems [22].

In Chapter 3, the strain-smoothed 4-node quadrilateral finite element was proposed using the SSE method. The proposed element has the smoothed strain field within an element by utilizing the strains of neighboring elements. The piecewise linear shape functions are employed for the quadrilateral element. No special smoothing domains are created and thus the standard FEM framework is maintained. The proposed strain-smoothed element passed the basic tests (the isotropic element, zero energy mode and patch tests), and provided highly accurate solutions compared with the standard, edge-based smoothed and incompatible modes quadrilateral elements in various numerical examples [23]. It is still necessary to extend the SSE method for improving other finite elements in the consistent manner presented in this paper.

In Chapter 4, the strain-smoothed MITC3+ shell finite element was developed, in which the membrane behavior of the MITC3+ shell finite element was significantly improved without additional degrees of freedom (DOFs). We obtained the covariant membrane strain of the MITC3+ shell element by decomposing its strains, and applied the SSE method to the membrane strain. With the SSE method, special smoothing domains are not necessary. The strain-smoothed MITC3+ shell element passed the patch, isotropy and zero energy mode tests. Through the numerical examples, it was observed that the strain-smoothed MITC3+ shell element retains excellent bending behavior while showing significantly improved membrane behavior. The strain-smoothed MITC3+ shell element showed solution accuracy comparable to other shell elements with more DOFs [25].

In Chapter 5, the formulation of the strain-smoothed MITC3+ shell finite element was extended to geometric nonlinear analysis. The total Lagrangian formulation was employed to describe large displacements and rotations. The SSE method was adopted for the membrane strain fields of the shell element, leading to the tangent stiffness matrix and internal force vector. The strain-smoothed MITC3+ shell element also showed the same superior performance in geometric nonlinear analysis, and thus we can conclude that the strain-smoothed MITC3+ shell element can be used very powerfully for the analysis of general shell structures.

In Chapter 6, the theoretical foundation for the SSE method was presented. A variational framework for the SSE method was established, and the convergence and stability analyses were performed based on the defined variational principle. The smoothed strains in the SSE method can be obtained by applying a sequence of orthogonal projection operators among assumed strain spaces. Invoking this observation, the mixed variational principle for the SSE method was established. The SSE method can be derived as a conforming Galerkin approximation of the defined variational principle. Then, a unifying convergence analysis of the standard FEM, the S-FEM, and the SSE method was performed to verify faster convergence of the SSE method compared with others. Note that, while the argument dealt with the triangular element, it can be generalized straightforwardly to other elements.

Bibliography

[1] K.J. Bathe, Finite element procedures, 2nd ed., K.J. Bathe, Watertown, 2014, and Higher Education Press, China, 2016.

[2] T.J.R. Hughes, The finite element method: linear static and dynamic finite element analysis, Dover Publications, Mineola, NY, 2000.

[3] R.D. Cook, Concepts and Applications of Finite Element Analysis, John Wiley & Sons, New York, 2007.

[4] G.R. Liu, K.Y. Dai, T.T. Nguyen, A smoothed finite element method for mechanics problems, Comput. Mech. 39 (2007) 859–877.

[5] S.P.A. Bordas, T. Rabczuk, N.X. Hung, V.P. Nguyen, S. Natarajan, T. Bog, D.M. Quan, N.V. Hiep, Strain smoothing in FEM and XFEM, Comput. Struct. 88 (2010) 1419–1443.

[6] A. Hamrani, S.H. Habib, I. Belaidi, CS-IGA: A new cell-based smoothed isogeometric analysis for 2D computational mechanics problems, Comput. Methods Appl. Mech. Eng. 315 (2017) 671–690.

[7] G.R. Liu, T. Nguyen-Thoi, H. Nguyen-Xuan, K.Y. Lam, A node-based smoothed finite element method (NS-FEM) for upper bound solutions to solid mechanics problems, Comput. Struct. 87 (2009) 14–26.

[8] T. Nguyen-Thoi, H.C. Vu-Do, T. Rabczuk, H. Nguyen-Xuan, A node-based smoothed finite element method (NS-FEM) for upper bound solution to visco-elastoplastic analyses of solids using triangular and tetrahedral meshes, Comput. Methods Appl. Mech. Eng. 199 (2010) 3005–3027.

[9] G. Wang, X.Y. Cui, H. Feng, G.Y. Li, A stable node-based smoothed finite element method for acoustic problems, Comput. Methods Appl. Mech. Eng. 297 (2015) 348–370.

[10] G.R. Liu, T. Nguyen-Thoi, K.Y. Lam, An edge-based smoothed finite element method (ES-FEM) for static, free and forced vibration analyses of solids, J. Sound Vib. 320 (2009) 1100–1130.

[11] Z.C. He, G.R. Liu, Z.H. Zhong, S.C. Wu, G.Y. Zhang, A.G. Cheng, An edge-based smoothed finite element method (ES-FEM) for analyzing three-dimensional acoustic problems, Comput. Methods Appl. Mech. Eng. 199 (2009) 20–33.

[12] T. Nguyen-Thoi, G.R. Liu, H. Nguyen-Xuan, An n-sided polygonal edge-based smoothed finite element method (nES-FEM) for solid mechanics, Int. j. Numer. Method. Biomed. Eng. 27 (2011) 1446–1472.

[13] L. Chen, T. Rabczuk, S.P.A. Bordas, G.R. Liu, K.Y. Zeng, P. Kerfriden, Extended finite element method with edge-based strain smoothing (ESm-XFEM) for linear elastic crack growth, Comput. Methods Appl. Mech. Eng. 209–212 (2012) 250–265.

[14] H. Nguyen-Xuan, G.R. Liu, S. Bordas, S. Natarajan, T. Rabczuk, An adaptive singular ES-FEM for mechanics problems with singular field of arbitrary order, Comput. Methods Appl. Mech. Eng. 253 (2013) 252–273.

[15] C. Lee, H. Kim, S. Im, Polyhedral elements by means of node/edge-based smoothed finite element method, Int. J. Numer. Methods Eng. 110 (2016) 1069–1100.

[16] C. Lee, H. Kim, J. Kim, S. Im, Polyhedral elements using an edge-based smoothed finite element method for nonlinear elastic deformations of compressible and nearly incompressible materials, Comput. Mech. 60 (2017) 659–682.

[17] T. Nguyen-Thoi, G.R. Liu, K.Y. Lam, G.Y. Zhang, A face-based smoothed finite element method (FS-FEM) for 3D linear and geometrically non-linear solid mechanics problems using 4-node tetrahedral elements, Int. J. Numer. Methods Eng. 78 (2009) 324–353.

[18] T. Nguyen-Thoi, G.R. Liu, H.C. Vu-Do, H. Nguyen-Xuan, A face-based smoothed finite element method (FS-FEM) for visco-elastoplastic analyses of 3D solids using tetrahedral mesh, Comput. Methods Appl. Mech. Eng. 198 (2009) 3479–3498.

[19] D. Sohn, J. Han, Y.S. Cho, S. Im, A finite element scheme with the aid of a new carving technique combined with smoothed integration, Comput. Methods Appl. Mech. Eng. 254 (2013) 42–60.

[20] S. Jin, D. Sohn, S. Im, Node-to-node scheme for three-dimensional contact mechanics using polyhedral type variable-node elements, Comput. Methods Appl. Mech. Eng. 304 (2016) 217–242.

[21] J.S. Chen, S. Yoon, C.T. Wu, A stabilized conforming nodal integration for Galerkin mesh-free methods, Int. J. Numer. Methods Eng. 53 (2001) 2587–2615.

[22] C. Lee, P.S. Lee, A new strain smoothing method for triangular and tetrahedral finite elements, Comput. Methods Appl. Mech. Eng. 341 (2018) 939–955.

[23] Lee C, Kim S, Lee PS. The strain-smoothed 4-node quadrilateral finite element. Comput. Methods Appl. Mech. Eng. In revision.

[24] Y. Lee, P.S. Lee, K.J. Bathe, The MITC3+ shell element and its performance, Comput. Struct. 138 (2014) 12–23.

[25] C. Lee, P.S. Lee, The strain-smoothed MITC3+ shell finite element, Comput. Struct. 223 (2019) 106096.

[26] J.M. Melenk, I. Babuška, The partition of unity finite element method: Basic theory and applications, Comput. Methods Appl. Mech. Eng. 139 (1996) 289–314.

[27] I. Babuška, J.M. Melenk, The partition of unity method, Int. J. Numer. Methods Eng. 40 (1997) 727–758.

[28] T. Strouboulis, I. Babuška, K. Copps, The design and analysis of the Generalized Finite Element Method, Comput. Methods Appl. Mech. Eng. 181 (2000) 43–69.

[29] T. Belytschko, T. Black, Elastic crack growth in finite elements with minimal remeshing, Int. J. Numer. Methods Eng. 45 (1999) 601–620.

[30] N. Moës, J. Dolbow, T. Belytschko, A finite element method for crack growth without remeshing, Int. J. Numer. Methods Eng. 46 (1999) 131–150.

[31] S. Kim, P.S. Lee, A new enriched 4-node 2D solid finite element free from the linear dependence problem, Comput. Struct. 202 (2018) 25–43.

[32] S. Kim, P.S. Lee, New enriched 3D solid finite elements: 8-node hexahedral, 6-node prismatic, and 5-node pyramidal elements, Comput. Struct. 216 (2019) 40–63.

[33] S.P. Timoshenko, J.N. Goodier, Theory of elasticity, 3rd ed., McGraw-Hill, New York, 1970.

[34] Y. Yang, G. Sun, H. Zheng, A four-node tetrahedral element with continuous nodal stress, Comput. Struct. 191 (2017) 180–192.

[35] E.L. Wilson, R.L. Taylor, W.P. Doherty, J. Ghaboussi, Incompatible displacement models, in: S.J. Fenves (Ed.), Numerical and Computer Methods in Structural Mechanics, Academic Press, New York, 1973.

[36] A. Ibrahimbegovic, E.L. Wilson, A modified method of incompatible modes, Commun. Appl. Numer. Methods. 7 (1991) 187–194.

[37] E.L. Wilson, A. Ibrahimbegovic, Use of incompatible displacement modes for the calculation of element stiffnesses or stresses, Finite Elem. Anal. Des. 7 (1990) 229–241.

[38] Intel Math Kernel Library, http://software.intel.com/en-us/intel-mkl.

[39] Y. Li, G.R. Liu, An element-free smoothed radial point interpolation method (EFS-RPIM) for 2D and 3D solid mechanics problems, Comput. Math. with Appl. 77 (2019) 441–465.

[40] O.C. Zienkiewicz, R.L. Taylor, J.M. Too, Reduced integration technique in general analysis of plates and shells, Int. J. Numer. Methods Eng. 3 (1971) 275–290.

[41] T.J.R. Hughes, M. Cohen, M. Haroun, Reduced and selective integration techniques in the finite element analysis of plates, Nucl. Eng. Des. 46 (1978) 203–222.

[42] T.J.R. Hughes, Generalization of Selective Integration Procedures to Anisotropic and Nonlinear Media, Int. J. Numer. Methods Eng. (1980) 1413–1418.

[43] D.S. Malkus, T.J.R. Hughes, Mixed finite element methods - Reduced and selective integration techniques: A unification of concepts, Comput. Methods Appl. Mech. Eng. 15 (1978) 63–81.

[44] J.C. Simo, R.L. Taylor, K.S. Pister, Variational and projection methods for the volume constraint in finite deformation elasto-plasticity, Comput. Methods Appl. Mech. Eng. 51 (1985) 177–208.

[45] J.C. Simo, T.J.R. Hughes, On the Variational Foundations of Assumed Strain Methods, J. Appl. Mech. 53 (1986) 51–54.

[46] J.C. Simo, M.S. Rifai, A class of mixed assumed strain methods and the method of incompatible modes, Int. J. Numer. Methods Eng. 29 (1990) 1595–1638.

[47] T. Belytschko, C. -S Tsay, A stabilization procedure for the quadrilateral plate element with one-point quadrature, Int. J. Numer. Methods Eng. 19 (1983) 405–419.

[48] T. Belytschko, W.E. Bachrach, Efficient implementation of quadrilaterals with high coarse-mesh accuracy, Comput. Methods Appl. Mech. Eng. 54 (1986) 279–301.

[49] T. Belytschko, I. Leviathan, Physical stabilization of the 4-node shell element with one point quadrature, Comput. Methods Appl. Mech. Eng. 113 (1994) 321–350.

[50] K.J. Bathe, A. Iosilevich, D. Chapelle, An evaluation of the MITC shell elements, Comput. Struct. 75 (2000) 1–30.

[51] K.J. Bathe, P.S. Lee, J.F. Hiller, Towards improving the MITC9 shell element, Comput. Struct. 81 (2003) 477–489.

[52] K.J. Bathe, P.S. Lee, Measuring the convergence behavior of shell analysis schemes, Comput. Struct. 89 (2011) 285–301.

[53] P.S. Lee, K.J. Bathe, On the asymptotic behavior of shell structures and the evaluation in finite element solutions, Comput. Struct. 80 (2002) 235–255.

[54] P.S. Lee, K.J. Bathe, Development of MITC isotropic triangular shell finite elements, Comput. Struct. 82 (2004) 945–962.

[55] J.F. Hiller, K.J. Bathe, Measuring convergence of mixed finite element discretizations: An application to shell structures, Comput. Struct. 81 (2003) 639–654.

[56] D. Chapelle, K.J. Bathe, The Finite Element Analysis of Shells-Fundamentals, Springer Science & Business Media, 2010.

[57] H.M. Jeon, Y. Lee, P.S. Lee, K.J. Bathe, The MITC3+ shell element in geometric nonlinear analysis, Comput. Struct. 146 (2015) 91–104.

[58] H. Jun, K. Yoon, P.S. Lee, K.J. Bathe, The MITC3+ shell element enriched in membrane displacements by interpolation covers, Comput. Methods Appl. Mech. Eng. 337 (2018) 458–480.

[59] Y. Ko, Y. Lee, P.S. Lee, K.J. Bathe, Performance of the MITC3+ and MITC4+ shell elements in widely-used benchmark problems, Comput. Struct. 193 (2017) 187–206.

[60] Y. Ko, P.S. Lee, K.J. Bathe, The MITC4+ shell element and its performance, Comput. Struct. 169 (2016) 57–68.

[61] Y. Ko, P.S. Lee, K.J. Bathe, A new 4-node MITC element for analysis of two-dimensional solids and its formulation in a shell element, Comput. Struct. 192 (2017) 34–49.

[62] Y. Ko, P.S. Lee, K.J. Bathe, The MITC4+ shell element in geometric nonlinear analysis, Comput. Struct. 185 (2017) 1–14.

[63] C.M. Shin, B.C. Lee, Development of a strain-smoothed three-node triangular flat shell element with drilling degrees of freedom, Finite Elem. Anal. Des. 86 (2014) 71–80.

[64] D.J. Payen, K.J. Bathe, A stress improvement procedure, Comput. Struct. 112–113 (2012) 311–326.

[65] D.J. Allman, A compatible triangular element including vertex rotations for plane elasticity analysis, Comput. Struct. 19 (1984) 1–8.

[66] I. Katili, A new discrete Kirchhoff-Mindlin element based on Mindlin-Reissner plate theory and assumed shear strain fields—part I: An extended DKT element for thick-plate bending analysis, Int. J. Numer. Methods Eng. 36 (1993) 1859–1883.

[67] C.A. Felippa, C. Militello, Membrane triangles with corner drilling freedoms-II. The ANDES element, Finite Elem. Anal. Des. 12 (1992) 189–201.

[68] C.A. Felippa, A study of optimal membrane triangles with drilling freedoms, Comput. Methods Appl. Mech. Eng. 192 (2003) 2125–2168.

[69] Y. Başar, Y. Ding, Finite-rotation shell elements for the analysis of finite-rotation shell problems, Int. J. Numer. Methods Eng. 34 (1992) 165–169.

[70] K.Y. Sze, X.H. Liu, S.H. Lo, Popular benchmark problems for geometric nonlinear analysis of shells, Finite Elem. Anal. Des. 40 (2004) 1551–1569.

[71] G. R. Liu, T. Nguyen-Thoi, Smoothed Finite Element Methods, CRC Press, New York, 2010.

[72] G.R. Liu, H. Nguyen-Xuan, T. Nguyen-Thoi, A theoretical study on the smoothed FEM (S-FEM) models: Properties, accuracy and convergence rates, Int. J. Numer. Methods Eng. 84 (2010) 1222–1256.

[73] S. Brenner, R. Scott, The Mathematical Theory of Finite Element Methods, Springer, New York, 2007.

[74] G. Teschl, Mathematical Methods in Quantum Mechanics, American Mathematical Society, Providence, 2009.

[75] G.R. Liu, A G space theory and a weakened weak (W2) form for a unified formulation of compatible and incompatible methods: Part I theory, Int. J. Numer. Methods Eng. (2009) 1093–1126.

[76] P. G. Ciarlet, The Finite Element Method for Elliptic Problems, SIAM, Philadelphia, 2002.